



LUND UNIVERSITY

Ultrafast Photoionization Dynamics Studied with Coincidence Momentum Imaging Spectrometers

Cheng, Yu-Chen

2019

Document Version:

Publisher's PDF, also known as Version of record

[Link to publication](#)

Citation for published version (APA):

Cheng, Y.-C. (2019). *Ultrafast Photoionization Dynamics Studied with Coincidence Momentum Imaging Spectrometers*. Department of Physics, Lund University.

Total number of authors:

1

Creative Commons License:

CC BY-NC

General rights

Unless other specific re-use rights are stated the following general rights apply:

Copyright and moral rights for the publications made accessible in the public portal are retained by the authors and/or other copyright owners and it is a condition of accessing publications that users recognise and abide by the legal requirements associated with these rights.

- Users may download and print one copy of any publication from the public portal for the purpose of private study or research.
- You may not further distribute the material or use it for any profit-making activity or commercial gain
- You may freely distribute the URL identifying the publication in the public portal

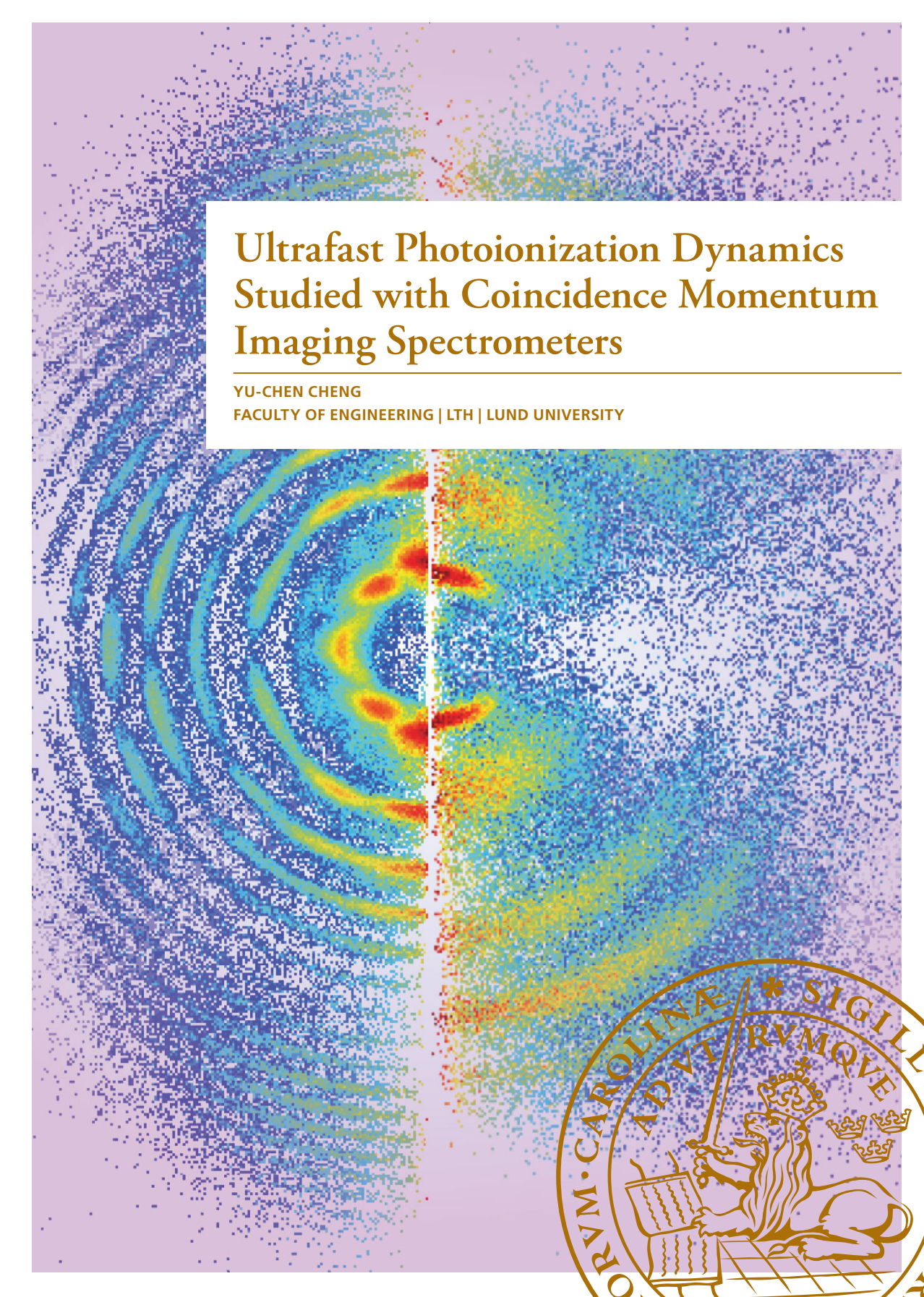
Read more about Creative commons licenses: <https://creativecommons.org/licenses/>

Take down policy

If you believe that this document breaches copyright please contact us providing details, and we will remove access to the work immediately and investigate your claim.

LUND UNIVERSITY

PO Box 117
221 00 Lund
+46 46-222 00 00



Ultrafast Photoionization Dynamics Studied with Coincidence Momentum Imaging Spectrometers

YU-CHEN CHENG

FACULTY OF ENGINEERING | LTH | LUND UNIVERSITY



ULTRAFAST PHOTOIONIZATION DYNAMICS STUDIED WITH COINCIDENCE MOMENTUM IMAGING SPECTROMETERS

Yu-Chen Cheng

Doctoral Thesis
2019



LUND UNIVERSITY

Akademisk avhandling som för avläggande av teknologie doktorexamen vid tekniska fakulteten vid Lunds Universitet kommer att offentlig försvaras den 5 april 2019, kl. 09.15 i Rydbergs sal, på Fysiska Institutionen, Professorsgatan 1, Lund.

Fakultetsopponent: Dr. Giuseppe Sansone
Albert-Ludwigs-Universität Freiburg, Tyskland

Academic thesis which, by due permission of the Faculty of Engineering at Lund University, will be publicly defended on 5th of April 2019, at 09.15 a.m. in Rydberg's hall, at the Department of Physics, Professorsgatan 1, Lund, for the degree of Doctor of Philosophy in Engineering.

Faculty opponent: Dr. Giuseppe Sansone
Albert Ludwig University of Freiburg, Germany

Organization LUND UNIVERSITY Division of Atomic Physics Department of Physics P.O. Box 118 SE-221 00 Lund, Sweden	Document name DOCTORAL DISSERTATION	
Author Yu-Chen Cheng	Date of issue February, 2019	
Title and subtitle Ultrafast Photoionization Dynamics Studied with Coincidence Momentum Imaging Spectrometers	Sponsoring organization	
Abstract <p>The time scale of the dynamics in atoms and molecules varies from attoseconds (10^{-18}) to picoseconds (10^{-12}) depending on the size of the particles. To study such dynamics, ultrafast light pulses are needed to trigger and capture the reaction. One of the most direct methods consists in ionizing the system and observing the following response. In this work, we use two different light sources with coincidence momentum imaging spectrometers. In the first experiment, we study electron wave packet interferences, while the second experiment focuses on electron and nuclear dynamics after multiple photoionization.</p> <p>In the first study, the experiment is performed with XUV attosecond pulses and a weak few-cycle infrared (IR) field. The attosecond pulses are produced from high harmonic generation (HHG) driven by an intense high-repetition-rate few-cycle IR field based upon optical parametric chirped pulse amplification (OPCPA). A weak fraction of the IR field is sent together with the attosecond pulses into a helium gas target. The photoelectrons are measured with a newly built momentum imaging spectrometer, which detects electrons over a full solid angle. The photoelectron momentum distribution is focused to be asymmetric relative to the plane perpendicular to the polarization axis and carrier-envelope phase (CEP) dependent. This asymmetry in photoemission can be explained by an interference phenomenon controlled by the relative amplitude and phase of the attosecond pulses.</p> <p>In the second study, the dissociation dynamics of the polyatomic molecule methyl iodide (CH_3I) was investigated with the intense XUV free electron laser in Hamburg (FLASH). We developed a model to describe the ionization and dissociation dynamics assuming a 3-fold symmetry. This model allowed us to study the charge transfer mechanism from the iodine atom to the methyl group (CH_3). Another mechanism contributing to the ionization of this methyl group was identified.</p> <p>This thesis contributes to the development of ultrafast and high-repetition-rate femtosecond lasers and attosecond light sources as well as three-dimensional momentum spectrometers. Hopefully, these tools will lead to further knowledge on ultrafast atomic and molecular physics.</p>		
Key words: Photoionization, High-order Harmonic Generation, Extreme Ultraviolet, Free-Electron Laser, Molecular Dissociation, Charge Transfer, Coincidence Measurement, Momentum Imaging, Electron Wave Packet		
Classification system and/or index terms (if any): 33.80.Eh, 42.65.Ky, 42.65.Re, 41.60.Cr, 87.15.Mi, 87.15.ht, 07.81.+a		
Supplementary bibliographical information:	Language English	
ISSN and key title: ISSN 0281-2762, Lund Reports on Atomic Physics, LRAP-555	ISBN 978-91-7895-026-3 (print) 978-91-7895-027-0 (pdf)	
Recipient's notes	Number of pages 189	Price
Security classification		

I, the undersigned, being the copyright owner of the abstract of the above-mentioned dissertation, hereby grant to all reference sources permission to publish and disseminate the abstract of the above-mentioned dissertation.

Signature



Date: 28nd February 2019

ULTRAFAST PHOTOIONIZATION
DYNAMICS STUDIED WITH
COINCIDENCE MOMENTUM
IMAGING SPECTROMETERS

Yu-Chen Cheng

Doctoral Thesis
2019



ULTRAFAST PHOTOIONIZATION DYNAMICS STUDIED WITH COINCIDENCE MOMENTUM
IMAGING SPECTROMETERS

Cover illustration, front: Photoelectron measurements from CIEL spectrometer.

Left: Krypton ATI photoelectron spectrum.

Right: Helium photoelectron spectrum from two-photon (XUV+IR) ionization.

Cover illustration, back: Photoion measurement from REMI spectrometer.

Spatial imaging of iodine ion fragment I^{5+} from the methyl iodide experiment

Funding information: This project has received funding from the European Union's Horizon 2020 research and innovation programme under the Marie Skłodowska-Curie grant agreement No 641789

pp. i-118 © 2019 Yu-Chen Cheng
Paper **I** © IOP Publishing 2017
Paper **II** © IOP Publishing 2017
Paper **III** © the authors
Paper **IV** © the authors
Paper **V** © the authors
Paper **VI** © American Chemical Society 2017

All rights reserved

Printed in Sweden by Media-Tryck, Lund, 2019

Division of Atomic Physics
Department of Physics
Faculty of Engineering, LTH
Lund University
P.O. Box 118
SE-221 00 Lund
Sweden

<http://www.atomic.physics.lu.se>

Lund Reports on Atomic Physics, LARP 555 (2019)

ISBN (print): 978-91-7895-026-3

ISBN (pdf): 978-91-7895-027-0

ISSN: 0281-2762

不經一番寒徹骨，焉得梅花撲鼻香

*Without the continuous bitter cold, there
can be no fragrant plum blossom.*

唐 黃檗禪師

ZEN MASTER, TANG DYNASTY

ABSTRACT

The time scale of the dynamics in atoms and molecules varies from attoseconds (10^{-18}) to picoseconds (10^{-12}) depending on the size of the particles. To study such dynamics, ultrafast light pulses are needed to trigger and capture the reaction. One of the most direct methods consists in ionizing the system and observing the following response. In this work, we use two different light sources with coincidence momentum imaging spectrometers. In the first experiment, we study electron wave packet interferences, while the second experiment focuses on electron and nuclear dynamics after multiple photoionization.

In the first study, the experiment is performed with XUV attosecond pulses and a weak few-cycle infrared (IR) field. The attosecond pulses are produced from high harmonic generation (HHG) driven by an intense high-repetition-rate few-cycle IR field based upon optical parametric chirped pulse amplification (OPCPA). A weak fraction of the IR field is sent together with the attosecond pulses into a helium gas target. The photoelectrons are measured with a newly built momentum imaging spectrometer, which detects electrons over a full solid angle. The photoelectron momentum distribution is focused to be asymmetric relative to the plane perpendicular to the polarization axis and carrier-envelope phase (CEP) dependent. This asymmetry in photoemission can be explained by an interference phenomenon controlled by the relative amplitude and phase of the attosecond pulses.

In the second study, the dissociation dynamics of the polyatomic molecule methyl iodide (CH_3I) was investigated with the intense XUV free electron laser in Hamburg (FLASH). We developed a model to describe the ionization and dissociation dynamics assuming a 3-fold symmetry. This model allowed us to study the charge transfer mechanism from the iodine atom to the methyl group (CH_3). Another mechanism contributing to the ionization of this methyl group was identified.

This thesis contributes to the development of ultrafast and high-repetition-rate femtosecond lasers and attosecond light sources as well as three-dimensional momentum spectrometers. Hopefully, these tools will lead to further knowledge on ultrafast atomic and molecular physics.

POPULAR SCIENCE SUMMARY

Atoms and molecules are small particles that form our world. By understanding their motion and interaction with light, we can learn more from the nature. Their motions are generally very fast, so we need a proper tool to observe them. It is usually easy to capture a motion with a high speed camera, which is at the order of milisecond (0.001 s, or 10^{-3} s). However, if we are looking at the atomic and molecular system, there is no camera with such a high speed shutter. It turns out that the alternative way is to manipulate the incoming light into ultrashort pulses. A general term for such special light sources are called ultrafast light sources.

How fast is ultrafast? In the daily life, the fastest device around us is the transistor speed of the computers and mobile phones. The time scale is around nanosecond (ns, 10^{-9} s). The conventional ultrafast definition starts from a smaller time unit called picosecond (ps, 10^{-12} s), and the molecular rotation time locates in this regime. However, it is still pretty slow comparing to the laser pulse width we used in the lab. The next time unit is femtosecond (fs, 10^{-15} s), which is the common unit in our lab for measuring the laser pulse width, and also most of the atomic and molecular dynamics are in this range. The last time unit in this thesis is attosecond (as, 10^{-18} s), which is used for measuring the electronic transition inside atoms or molecules. To have a direct idea of the smallest time scale, we give two examples in the following. We use the light speed to convert the short time scale into a distance, because light is the fastest thing in the universe. In about 1 second, light can travel from the earth to the moon. However, in 1 attosecond, light can only travel from an atom to another atom in solids. The other example is to have an analogy on the time scale. The ratio between 1 second to 1 attosecond is similar to the ratio of the age of universe (13.8 billion years $\approx 4.4 \times 10^{17}$) to 1 second. Both cases show how short time scale we are investigating.

Then the question will arise naturally. How do we generate such ultrashort pulses? The current conventional laser system can provide only down to femtosecond level (\sim few fs). In order to have shorter pulses, we use the process called high harmonic generation (HHG) technique providing attosecond pulses with hundreds of attoseconds duration. This thesis contributes to generate efficient attosecond pulses from a unique femtosecond laser system and to characterize the attosecond pulses.

As we have the ultrafast light source, the next step is to take a photo of atoms or molecules. In a traditional camera, photographic films or photo sensitive electronic devices are used as the image recorder. How do we make “film” at atomic scale? In this thesis, a special instrument called CIEL was built for recording pictures on atoms and molecules. After shooting the ultrafast laser pulses into atoms or molecules, they will absorb the light and emit negatively charged electrons and become positively charged ions. Under a well-prepared experimental condition, the electrons and the ions are collected with the instrument, which can provide the complete information about the emission of charged electrons and ions. By using physics conservation laws, we can reconstruct the atoms or molecules reaction induced by photons. In other words, the instrument acts as the recorder for having the photos of atomic and molecular dynamics. With the ultrafast light sources and the measurement instruments, in this thesis, we have investigated the electron dynamics and nuclear dynamics in atomic and molecular systems at the shortest possible time scale.

LIST OF PUBLICATIONS

This thesis is based on the following papers, which will be referred to in the text by their roman numerals.

I Compact 200 kHz HHG source driven by a few-cycle OPCPA

Anne Harth, Chen Guo, Yu-Chen Cheng, Arthur Losquin, Miguel Miranda, Sara Mikaelsson, Christoph M Heyl, Oliver Prochnow, Jan Ahrens, Uwe Morgner, Anne L'Huillier and Cord L Arnold.

Journal of Optics **20**, 014007 (2017).

II Phase control of attosecond pulses in a train

Chen Guo, Anne Harth, Stefanos Carlström, Yu-Chen Cheng, Sara Mikaelsson, Erik Mårzell, Christoph Heyl, Miguel Miranda, Mathieu Gisselbrecht, Mette B Gaarde, Kenneth J Schafer, Anders Mikkelsen, Johan Mauritsson, Cord L Arnold and Anne L'Huillier.

Journal of Physics B: Atomic, Molecular and Optical Physics **51**, 034006 (2018).

III A compact electron-ion coincidence spectrometer for attosecond time-resolved spectroscopy at high repetition rate

Yu-Chen Cheng, Saikat Nandi, Lisa Rämisch, Sara Mikaelsson, Bart Oostenrijk, Neven Ibraković, Anna Olofsson, Emma Simpson, Johan Mauritsson, Anne L'Huillier, and Mathieu Gisselbrecht.

(2019) *in manuscript*.

IV CEP controlled photoelectron emission using wave packet interference

Yu-Chen Cheng, Sara Mikaelsson, Saikat Nandi, Lisa Rämisch, Chen Guo, Anne Harth, Jan Vogelsang, Miguel Miranda, Cord L. Arnold, Anne L'Huillier, and Mathieu Gisselbrecht.

(2019) *in manuscript*.

V Ultrafast dynamics of methyl iodide studied with XUV Free Electron Laser

Yu-Chen Cheng, Bart Oostenrijk, Jan Lahl, Sylvain Maclot, Sven Augustin, Georg Schmid, Kirsten Schnorr, Severin Meister, Dimitrios Rompotis, Bastian Manschwetus, Cédric Bomme, Benjamin Erk, Daniel Rolles, Rebecca Boll, Pavel Olshin, Artem Rudenko, Michael Meyer, Per Johnsson, Robert Moshhammer, and Mathieu Gisselbrecht.
(2019) *in manuscript*.

VI Spatial Control of Multiphoton Electron Excitations in InAs Nanowires by Varying Crystal Phase and Light Polarization

Erik Mårzell, Emil Boström, Anne Harth, Arthur Losquin, Chen Guo, Yu-Chen Cheng, Eleonora Lorek, Sebastian Lehmann, Gustav Nylund, Martin Stankovski, Cord L. Arnold, Miguel Miranda, Kimberly A. Dick, Johan Mauritsson, Claudio Verdozzi, Anne L'Huillier, and Anders Mikkelsen.
Nano Letters **18**, 907-915 (2018).

ABBREVIATIONS

2DSI	Two-Dimensional Spectral Shearing interferometry
ADC	Analog to Digital Converter
ADK	Ammosov-Delone-Krařnov
APT	Attosecond Pulse Train
BBO	β -Barium Borate
CAMP	CFEL-ASG Multi Purpose
CEP	Carrier-Envelope Phase
CFD	Constant Fraction Discriminator
CH ₃ I	Methyl Iodide/iodomethane
CIEL	Coincidences entre Ions et Electrons Localises
COLTRIMS	Cold Target Recoil Ion Momentum Spectroscopy
COB	Classical Over-the Barrier
CPA	Chirp Pulse Amplification
DFG	Difference Frequency Generation
DLD	Delay Line Detector
EWP	Electron WavePacket
FEL	Free Electron Laser
FDTD	Finite Difference Time Domain
FLASH	Free Electron Laser in Hamburg
FROG	Frequency Resolved Optical Gating
FROG-CRAB	Frequency Resolved Optical Gating for Complete Reconstruction of Attosecond Bursts
FWHM	Full Width at Half Maximum
FWM	Four Wave Mixing
GD	Group Delay
GDD	Group Delay Dispersion

GVD	Group Velocity Dispersion
HHG	High Harmonic Generation
InAs	Indium Arsenide
IR	Infrared
KER	Kinetic Energy Release
KED	Kinetic Energy Distribution
LIGO	Laser Interferometer Gravitational Wave Observatory
MCP	Microchannel plate
MIIPS	Multiphoton Intrapulse Interference Phase Scan
NOPA	Noncollinear optical parametric Amplification
OCT	Optical Coherence Tomography
OPA	Optical Parametric Amplification
OPCPA	Optical Parametric Chirp Pulse Amplification
PEEM	PhotoElectron Emission Microscope
PIPICO	Photoion-Photoion Coincidence
PSD	Position Sensitive Detector
PVWC	Poynting Vector Walk-off Compensation
RABBITT	Reconstruction of Attosecond Beating by Interfering Two-photon Transition
REMI	REAction MIcroscope
RF	Radio Frequency
RIMS	Recoil Ion Momentum Spectroscopy
SFA	Strong Field Approximation
SFG	Sum Frequency Generation
SHG	Second Harmonic Generation
SPIDER	Spectral Phase Interference for Direct Electric-field Reconstruction
SPM	Self Phase Modulation
TDC	Time to Digital Converter
THG	Third Harmonic Generation
TOD	Third order Dispersion
TPM	Tangential Phase Matching
VMI	Velocity Momentum Imaging
WZ	Hexagonal Wurtzite
XUV	Extreme ultraviolet
ZB	Cubic Zinblende

CONTENTS

Abstract	v
Popular Science Summary	vii
1 Introduction	1
2 Ultrafast light source	5
2.1 Background	5
2.2 Few-Cycle OPCPA Laser System	12
2.2.1 Noncollinear Optical Parametric Amplification (NOPA)	13
2.2.2 Experimental Setup	15
2.2.3 Characterization	16
2.3 Application — Polarization Dependence of Multiphoton Induced Electron Emission from Nanostructures	21
2.3.1 Detection Instrument and Experimental Setup	21
2.3.2 Numerical Approach	22
2.3.3 Polarization-Dependent Photoemission	23
2.4 XUV attosecond light source	23
2.4.1 Microscopic — Classical Three-Step Model	24
2.4.2 Macroscopic — HHG Phase Matching	27
2.4.3 Experimental Setup — HHG Light Source	29
2.4.4 XUV Dispersion Scan	30
2.4.5 XUV attosecond pulses	33
2.5 Intense XUV Source — Free Electron Laser	34
3 3D Electron-Ion Momentum Imaging Spectrometer	39
3.1 Working Principle	40
3.2 Experimental Setup	45
3.2.1 Spectrometer Design	45
3.2.2 Magnetic Coils	46
3.2.3 Detection	49
3.3 Commissioning of the CIEL	52
3.3.1 Offset Calibration	53
3.3.2 Resolution Calibration	55
3.3.3 Ions Resolution	58
4 Applications	61
4.1 Electron Wave Packet Interferometry	61
4.1.1 Theory	62
4.1.2 Method	67
4.1.3 Result	67

4.2	Ultrafast electron dynamics of methyl iodide dissociation	73
4.2.1	Background	73
4.2.2	Data Analysis of Ions	79
4.2.3	Classical Sequential Ionization Model	82
4.2.4	Results	84
5	Summary and outlook	87
A	Transverse electron motion in uniform electric and magnetic field	89
B	Resolution of the spectrometer	91
C	Differential cross section	95
	Comments on the Papers	97
	Acknowledgements	101

Papers

I	Compact 200 kHz HHG source driven by a few-cycle OPCPA	121
II	Phase control of attosecond pulses in a train	137
III	A compact electron-ion coincidence spectrometer for attosecond time-resolved spectroscopy at high repetition rate	149
IV	CEP controlled photoelectron emission using wave packet interference	159
V	Ultrafast dynamics of methyl iodide studied with XUV Free Electron Laser	169
VI	Spatial Control of Multiphoton Electron Excitations in InAs Nanowires by Varying Crystal Phase and Light Polarization	179

INTRODUCTION

Electrons are behind a multitude of physical and chemical processes. The electron motion is at the heart of semiconductor components in electronics, and this motion depends on the geometry of the transistor design especially when the transistor size approaches the atomic scale. In chemical processes, the electrons form chemical bonds of various strength, affecting thereby the nuclear motion and the structure of the molecules. The nuclear motion can be manipulated by using visible photons, leading to molecular isomerization, dissociation or new molecules synthesis [1–3]. The timescale for these processes is often around tens or hundreds of femtosecond (fs, 10^{-15} s). The field of research dealing with ultrafast chemical processes is known as femtochemistry [4–6]. Since electron motion is much faster than nuclear motion it is envisioned that chemical reaction could be controlled by directly acting on the electron motion.

One traditional method to study electron dynamics is to use photons in the extreme ultraviolet (XUV) spectral range, i.e. with energies ranging from 10 to about a hundred electron volts (eV). The interaction between XUV radiation and atoms or molecules leads to the emission of electrons from the outer shells and shallow inner shells¹. Many observed processes cannot be understood without including interaction between electrons, also referred to as electron correlation. For example, Auger decay [7], which occurs after inner shell photoemission, and results in the emission of a second electron, is a direct signature of correlation since a photon can interact with only one electron. Photoemission/photoionization remains in essence a multi-body problem that is challenging but fascinating from both experimental and theoretical point of views. To address the dynamics of these processes, it is essential to match the natural timescale of the electron motion, which is in attosecond (10^{-18} s) time scale.

Thanks to laser technology development, powerful femtosecond lasers can be used to produce XUV attosecond pulses through a highly nonlinear process, called

¹For instance, it is possible to ionize the 4d shell in a xenon atom.

high harmonic generation (HHG)² [9, 10]. Attosecond pulses in combination with laser pulses have been used to investigate, among other things, electron dynamics in atomic photoionization [11–13] and electron charge transfer/migration inside molecules [14, 15].

An alternative method to study electron/nuclear motion utilizes free electron laser (FEL) radiation. The available pulse energies, in the tens of μJ range allows not only one-photon but multiphoton ionization processes [16, 17]. By choosing a suitable pulse energy, sequential multiple ionization can be made to match the dissociation time scale, providing a series of time stamps to investigate electron dynamics.

Such light sources ought to be followed by advanced instrumentation in order to develop new applications. To this end, we developed a spectrometer capable of detecting multiple charged particles in coincidence, providing thus information about correlations between charged particles after ionization. This spectrometer requires low ionization probability per light pulse [18] and benefits from high repetition rate light sources.

Thesis overview

This thesis work is concerned with the development of ultrafast light sources, charged particle spectrometers, and applications to the study of electron dynamics. Concerning the light sources, a high-repetition-rate (200 kHz) femtosecond IR laser system with 6-fs pulse duration was upgraded and characterized in detail (Paper I). Taking advantage of this high-repetition-rate and short pulse duration, a first application was performed on semiconductor nanostructures (Paper VI). The laser system was then used to efficiently generate XUV attosecond pulse trains (APT) through HHG. The properties of the generated APT were analyzed in Paper II.

The spectrometer developed in this work is based on an improved design of the so-called reaction microscope. It utilizes multiple detectors to image the three-dimensional momentum of the charged particles. A new spectrometer was developed, constructed, calibrated, and used in this thesis work. It is presented in Paper III and used in Paper IV.

The first application is a study of the photoionization dynamics in helium by using our high-repetition-rate attosecond light source and our momentum spectrometer. The results are presented in Paper IV. The second application consists in ionizing methyl iodide molecules (CH_3I), using a FEL (Free-Electron LASer in Hamburg, FLASH) in order to study electron charge transfer. The results are presented in Paper V.

The thesis is presented with the following order: In chapter 2, the ultrafast light sources used in the thesis are introduced. In chapter 3, the 3D momentum imaging spectrometers used for the experiments are presented. Emphasis is put

²The normal attosecond pulse duration is about a few hundreds of attoseconds, and the shortest attosecond pulses are around some tens of attoseconds. The current record is 43 attoseconds developed in 2017 [8].

on the description of the spectrometer which was built in this thesis work. The applications are presented in chapter 4. Finally, chapter 5 summarizes and provides an outlook.

ULTRAFAST LIGHT SOURCE

In nature, ultrafast processes usually take place in small-scale systems, particularly at the atomic and molecular scales. The time scale of nuclear motion is from femtoseconds to picoseconds, and the motion of electrons is even faster, i.e. in the attosecond regime. Studying such ultrafast dynamics requires ultrashort pulses, which lead to the term ultrafast light sources. These can be at different wavelengths. There are three categories of ultrafast light sources used in this thesis: few-cycle IR pulses (Paper **I**, Paper **VI**), extreme ultraviolet (XUV) attosecond pulses (Paper **I**, Paper **II**), and intense XUV pulses from a Free Electron Laser (FEL) (Paper **V**).

This chapter starts by introducing the basic concept of ultrashort pulse characteristics. Then, we will discuss how to generate and characterize ultrashort few-cycle IR laser pulses. This light source was used to study nanostructure samples (Paper **VI**) as well as to generate high-order harmonics and attosecond pulses. The XUV attosecond light source is presented in detail starting from a basic theoretical model to our experimental setup. The final part of this chapter introduces the intense XUV laser source from the FLASH facility in Hamburg. Its pulse energy is sufficient to induce XUV multiphoton ionization in molecules (Paper **V**).

2.1 Background

The fundamental wave equation is obtained from Maxwell's equations. The general expression of the wave equation can be written as follows¹:

$$\nabla^2 E(\mathbf{r}, t) = -\mu_0 \frac{\partial^2 D(\mathbf{r}, t)}{\partial t^2} \quad (2.1)$$

¹It is assumed that the polarization is along a certain axis, such that the equation here is in a scalar format

where $E(\mathbf{r}, t)$ is the electric field as a function of time t and space \mathbf{r} , μ_0 is the permeability of free space, and $D(\mathbf{r}, t)$ is the electric flux density defined as:

$$D = \epsilon_0 E + P \quad (2.2)$$

ϵ_0 is the permittivity of free space, and P is the polarization density. If the medium is linear and isotropic, P can be written as:

$$P(\mathbf{r}, t) = \epsilon_0 \int_{-\infty}^t \chi^{(1)}(t - t') E(\mathbf{r}, t') dt', \quad (2.3)$$

where $\chi^{(1)}$ represents the linear susceptibility. By performing a Fourier transform on the polarization density P , the convolution in equation 2.3 is replaced by a product. The Fourier transform of equation 2.1 becomes:

$$\nabla^2 \tilde{E}(\mathbf{r}, \omega) = \mu_0 \epsilon_0 [1 + \chi^{(1)}(\omega)] \omega^2 \tilde{E}(\mathbf{r}, \omega) = \frac{n^2}{c^2} \omega^2 \tilde{E}(\mathbf{r}, \omega), \quad (2.4)$$

where $\tilde{E}(\mathbf{r}, \omega)$ is the Fourier transform of $E(\mathbf{r}, t)$. Equation 2.4 supports free propagating wave solutions with velocity c/n , where $n = \sqrt{1 + \chi^{(1)}(\omega)}$ is the frequency dependent refractive index.

Fundamental Properties of a Light Pulse

Consider a temporal solution $E(\mathbf{r}, t)$ with a pulse profile $a(t)$ (Gaussian envelope, i.e. $a(t) = a_0 \exp[-t^2/2T_0^2]$, with a_0 being the electric field amplitude) and a central oscillation frequency ω_0 , also called the carrier frequency:

$$E(\mathbf{r}, t) = a(t) e^{i(\omega_0 t - \mathbf{k} \cdot \mathbf{r})}, \quad (2.5)$$

where \mathbf{k} is the wavevector for which the amplitude is called wavenumber $2\pi n/\lambda$ and λ denotes the wavelength. The Full Width at Half Maximum (FWHM) of the temporal intensity profile is $\Delta T_{\text{FWHM}} = 2\sqrt{\ln 2} T_0 \sim 1.665 T_0$. The spectral amplitude can be written as:

$$\tilde{E}(\mathbf{r}, \omega) = \sqrt{2\pi} T_0 a_0 e^{-\frac{1}{2}(\omega - \omega_0)^2 T_0^2} e^{-i\mathbf{k} \cdot \mathbf{r}}, \quad (2.6)$$

which satisfies equation 2.4. The frequency bandwidth of equation 2.6 is $\Delta\omega_{\text{FWHM}} = 2\sqrt{\ln 2}/T_0$. One can define the time-bandwidth product, which expresses that short laser pulses require a broad spectrum.

$$\Delta\omega_{\text{FWHM}} \Delta T_{\text{FWHM}} = 4 \ln 2 \quad (2.7)$$

The time-bandwidth product is more commonly written with the frequency instead of the angular frequency².

$$\Delta\nu_{\text{FWHM}} \Delta T_{\text{FWHM}} = \frac{4 \ln 2}{2\pi} \approx 0.441, \quad (2.8)$$

²The time-bandwidth product depends on the pulse shape. For pulses with an intensity profile sech^2 , as for certain solitons, it is e.g. 0.315.

One of the most common ways to obtain a broad spectrum is to use a Titanium-Sapphire (Ti:Sapphire) crystal with a spectral range from 600 nm to 1100 nm [19]. This spectrum can support ultrashort laser pulses down to around 5 fs [20–23].

Chromatic Dispersion

Each frequency component travels with a slightly different velocity $c/n(\omega)$ in a medium, which is also known as chromatic dispersion. Different orders of dispersion are defined by a Taylor expansion of the wavenumber k ³, i.e.:

$$k(\omega) = k_0 + \frac{\partial k}{\partial \omega}(\omega - \omega_0) + \frac{1}{2} \frac{\partial^2 k}{\partial \omega^2}(\omega - \omega_0)^2 + \frac{1}{6} \frac{\partial^3 k}{\partial \omega^3}(\omega - \omega_0)^3 + \dots \quad (2.9)$$

The zero-order term is related to the phase velocity $v_p = \omega/k_0$, which is the propagation velocity of the phase front. The first-order term is the inverse of the group velocity (or $v_g = \frac{\partial \omega}{\partial k}$), changing only the time delay of the pulse, but not the pulse shape. The second-order term is called group velocity dispersion (GVD) or group delay dispersion (GDD) per unit length. A pulse is called transform-limited when it has the shortest duration for a given spectrum, as described by equation 2.7. In

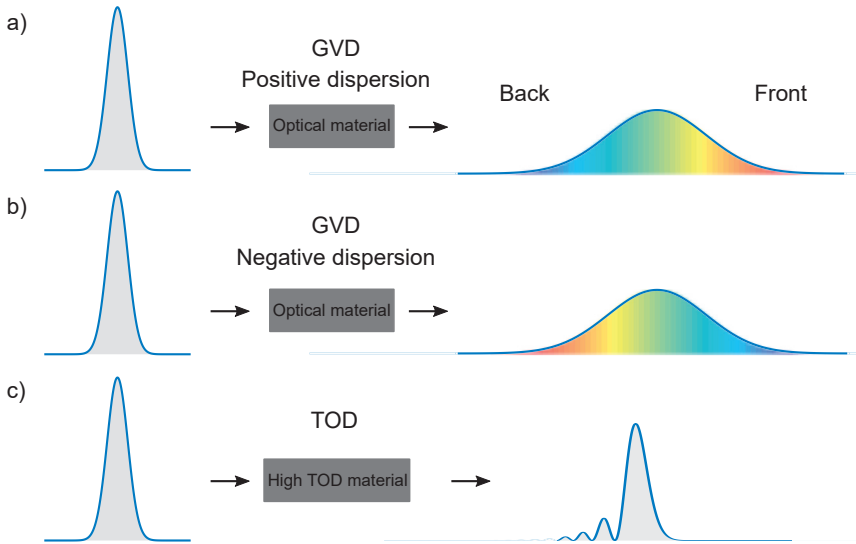


Figure 2.1: Schematic drawing of (a) positive group velocity dispersion, (b) negative group velocity dispersion, and (c) third order dispersion.

a transform-limited pulse, all frequencies are in phase with each other. Dispersion leads to a temporal shift of the different frequencies and the pulse stretches in time.

³ β is also used as a notation for the wavenumber in other books

Any transparent media in the visible range is positive dispersive (normal dispersion, positive GVD). After a transform-limited pulse travels through the positive dispersive medium, the lower frequencies (red) will be at the pulse front and the higher frequencies (blue) will be at the back. The frequency then changes from a lower frequency to a higher frequency, leading to the pulse being up-chirped as shown in figure 2.1 (a). In the opposite case, when a transform-limited pulse propagates through a negative dispersive material (anomalous dispersion, negative GVD), the higher frequencies (blue) will appear at the pulse front and the lower frequencies (red) at the back (figure 2.1 (b)). The third-order term is called third-order dispersion (TOD) per unit length. If the TOD is large, it leads to an oscillating structure at the tail of the pulse (figure 2.1 (c)).

Carrier-Envelope Phase

If the pulse duration corresponds to just a few cycles of the carrier frequency⁴, light-matter interactions driven by such a pulse often depend on the electric field itself rather than the intensity envelope⁵. In this condition, the phase difference between the carrier electric field and the envelope of electric field, defined as Carrier-Envelope Phase (CEP), becomes important.

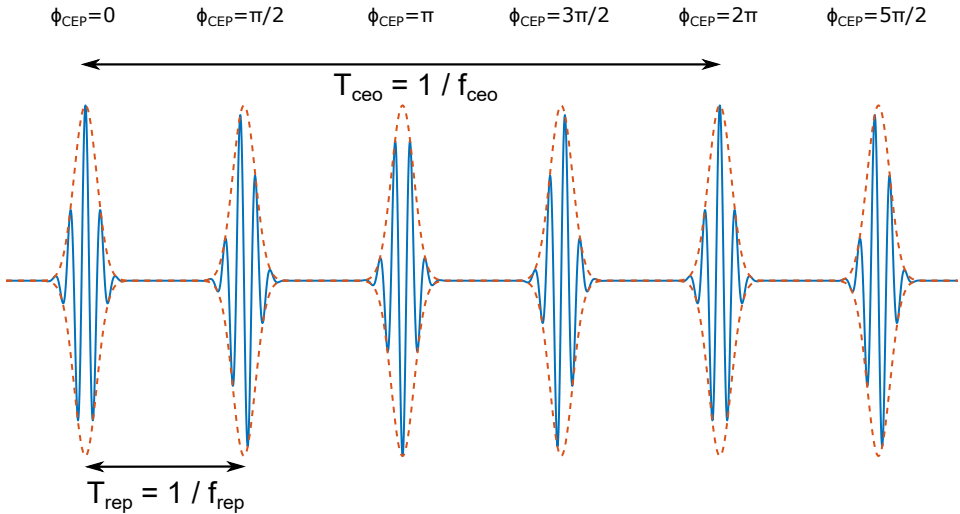


Figure 2.2: Varying CEP of the electric field in a pulse train. The separation between two pulses is $1/f_{\text{rep}}$. The carrier envelope offset frequency f_{ceo} is set to a quarter of the repetition rate. In other words, every fourth pulse has the same CEP.

In this thesis work, a passively mode-locked oscillator was used to provide CEP-stable pulses as a seed for further amplification. The output optical frequency of

⁴Such a pulse is often called a few-cycle pulse.

⁵A cycle of 800 nm light (Ti:Sapphire) is equal to 2.6 fs.

the oscillator is a multiple of its repetition rate f_{rep} with a constant carrier envelope offset frequency ν_{ceo} [24]:

$$\nu = Nf_{rep} + \nu_{ceo} \quad (2.10)$$

The carrier offset frequency ν_{ceo} causes the CEP to vary periodically from pulse to pulse, which is illustrated in figure 2.2. In the real world, mechanical vibrations, thermal variations, and air flow disturbances are noise sources for the CEP. The method for measuring the carrier envelope frequency offset is to perform f-2f interferometry, which requires an octave spanning spectrum. By doubling the fundamental spectrum, the beating signal between the fundamental and second harmonic (SH) is the carrier envelope frequency offset phase⁶,

$$\nu_{beat} = \nu_{SH} - \nu_{fund} = 2(N'f_{rep} + \nu_{ceo}) - (Nf_{rep} + \nu_{ceo}) = \nu_{ceo}, \quad (2.11)$$

since $2N' = N$. The beating signal can be stabilized to a reference frequency, thus canceling the CEP noise and stabilizing the CEP. In our oscillator, we chose active feedback to stabilize our beating signal. The difference between the beating signal and the reference signal is used to derive an error signal, which modulated the pump laser of the oscillator and thereby adjusted ν_{ceo} . In our case, ν_{ceo} is stabilized to a quarter of the repetition rate. Before the amplification, the CEP indeed changes periodically with every 4 pulses (as figure 2.2). Since the amplification only picks the 1st pulse out of every 400 pulses, the final output of the amplified laser is effectively CEP locked. The CEP stabilization from the oscillator is called fast feedback loop. There is another slow feedback loop after the amplification to compensate the long term phase drift of the amplifier chain.

Gaussian Beam

The spatial profile of a laser beam, needed to e.g. estimate the local intensity, can be found by solving the spatial part of equation 2.4. For convenience, it is assumed that the light field propagates along the +z direction. Then, it is useful to decompose the Laplace operator into transverse and longitudinal components (i.e. $\nabla^2 = \nabla_T^2 + \partial^2/\partial z^2$). Under the paraxial wave approximation, the longitudinal variation of the electric field amplitude is assumed much slower than an optical wavelength. Equation 2.4 can then be simplified to:

$$\nabla_T^2 E(\mathbf{r}) - 2ik \frac{\partial E(\mathbf{r})}{\partial z} = 0, \quad (2.12)$$

also called paraxial wave approximation. One of the simplest solutions to equation 2.12 in the Gaussian beam is [25]:

$$E(r, z) = A_0 \frac{W_0}{W(z)} \exp \left[-\frac{r^2}{W^2(z)} \right] \exp \left[-i(kz + k \frac{r^2}{2R(z)} - \zeta(z)) \right] \quad (2.13)$$

⁶In practice, the beating signal comes from the frequency-doubled red part of the fundamental and blue part of the fundamental.

where A_0 is a constant amplitude, W_0 is the beam waist ($W_0 = \sqrt{\lambda z_R/\pi}$), $W(z)$ is the beam radius as a function of propagation distance z ($W(z) = W_0\sqrt{1 + (z/z_R)^2}$), $R(z)$ is the radius of curvature ($R(z) = z[1 + (z_R/z)^2]$) of the wavefront, and the last term $\zeta(z)$ is called the Gouy phase ($\zeta(z) = \tan^{-1}(z/z_R)$). The common parameter z_R is called the Rayleigh range. The Gaussian beam solution in equation 2.13 describes a laser beam focused at $z = 0$ with as smallest radius W_0 (called beam waist). The beam radius increases to $\sqrt{2}W_0$ at z_R , where the area is twice the focal area. The length of the focus is given by the confocal parameter $b = 2z_R$.

The optical intensity is the power per unit area, and the relation between optical intensity and electric field is:

$$I(r, z) = \frac{1}{2}cn\epsilon_0|E(r, z)|^2 \quad (2.14)$$

At position z , the transverse intensity distribution is proportional to $\exp[-2r^2/W(z)^2]$, where the beam radius $W(z)$ denotes the width at which the intensity has fallen to 13.5% (i.e. e^{-2}) of its on-axis value. The intensity profile of a Gaussian beam $I(r, z)$ is shown in figure 2.3.

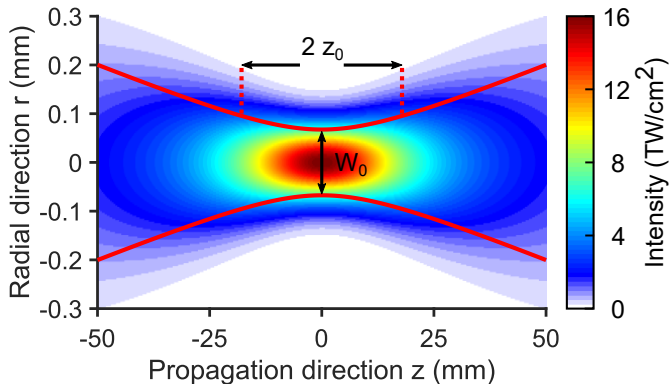


Figure 2.3: Gaussian beam intensity profile with a beam waist $W_0 = 135 \mu\text{m}$ and Rayleigh range $z_0 = 17.9 \text{ mm}$. These focusing conditions are those used in the experiment in Paper III.

Nonlinear Properties

In modern laser applications, different kinds of frequency conversion processes are generated by nonlinear interaction in transparent media. These processes can be identified by considering higher order terms of the polarization density P (equation 2.3). For simplicity, we assume that the linear and nonlinear responses are instantaneous, which simplifies the nonlinear susceptibilities $\chi^{(n)}$ as frequency in-

dependent. The polarization density P can be written as⁷:

$$P = \epsilon_0[\chi^{(1)}E + \chi^{(2)}E^2 + \chi^{(3)}E^3 + \dots] = P^{(1)} + P^{(2)} + P^{(3)} + \dots \quad (2.15)$$

The first linear term $P^{(1)}$ is the same as in equation 2.3. The second and third-order nonlinear susceptibilities, i.e. $\chi^{(2)}$ and $\chi^{(3)}$, are the basis for a number of processes in nonlinear optics. In general, the nonlinear susceptibility χ is a tensor. The simplified expression 2.15 is valid when the different components are along the same polarization direction as the nonlinear polarization P .

We now consider an external electromagnetic field consisting of two monochromatic components oscillating at different frequencies, i.e:

$$E = \frac{1}{2}(E_1e^{i\omega_1t} + E_2e^{i\omega_2t} + c.c.) \quad (2.16)$$

We substitute this field into equation 2.15. The second-order term $P^{(2)}$ becomes:

$$\begin{aligned} P^{(2)} = \frac{\epsilon_0}{4} \{ & \chi^{(2)}E_1^2e^{i2\omega_1t} + \chi^{(2)}E_2^2e^{i2\omega_2t} \\ & + 2\chi^{(2)}E_1E_2e^{i(\omega_1+\omega_2)t} \\ & + 2\chi^{(2)}E_1E_2^*e^{i(\omega_1-\omega_2)t} \\ & + 2\chi^{(2)}(E_1E_1^* + E_2E_2^*) + c.c. \} \end{aligned} \quad (2.17)$$

Note that the second-order susceptibility $\chi^{(2)}$ is different for the different processes included in these equation, which are second harmonic generation (SHG) in the first two terms leading to frequencies $2\omega_1$, $2\omega_2$, sum-frequency generation (SFG)($\omega_1 + \omega_2$), difference-frequency generation (DFG)($\omega_1 - \omega_2$), and optical rectification (zero frequency terms). Some of the frequency mixing processes induced by the second-order nonlinearity are illustrated in figure 2.4.

Third-order nonlinear effects, also called four-wave mixing (FWM) processes, mix four electric field components (three inputs and one output). Some third-order nonlinear effects are also shown in figure 2.4. Third harmonic generation (THG) corresponds to absorption of three photons at frequency ω and emission of a photon at frequency 3ω . An important FWM process in this thesis is the Kerr effect corresponding to a modification of the refractive index, i.e. $n = n_0 + n_2I$. It leads to self-focusing in the spatial domain and to self-phase modulation (SPM) in the spectral domain.

Phase-Matching

Figure 2.4 illustrates energy conservation in different nonlinear processes. To convert photons efficiently, the momentum should also be conserved. Conservation of momentum implies that the different input and output waves oscillate in phase in

⁷The nonlinear polarization is written as a scalar term by assuming that the polarization is along a certain axis.

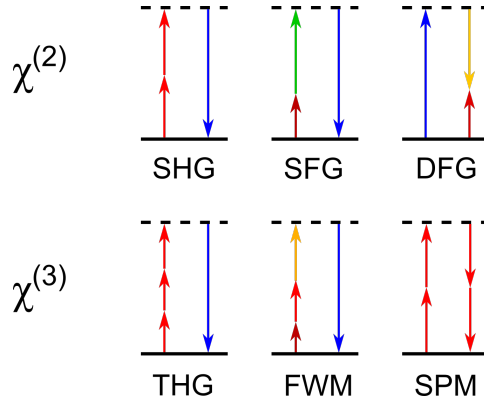


Figure 2.4: Schematic illustration of second and third-order nonlinear effects. The arrows pointing upward (downward) indicate absorption (emission). The dashed lines represent virtual states and the solid line at the bottom marks the ground state.

the nonlinear medium and is often referred as phase matching. Phase matching requires that the wavevector mismatch equals is minimized

$$\Delta \mathbf{k} = \mathbf{k}_1 - \mathbf{k}_2 - \mathbf{k}_3 \quad (2.18)$$

where \mathbf{k}_1 is the input field photon momentum; \mathbf{k}_2 and \mathbf{k}_3 are the output photon momenta for a DFG process. In a normal transparent medium, the wavevector mismatch is not easy to be minimized. Usually, phase-matching can be achieved in birefringent media, making use of different refractive indices in different polarization directions.

The main birefringent medium used in this thesis is β -barium borate (BBO). BBO is an uniaxial crystal, whose refractive index in one axis is different from the two other axes. If a light wave propagates with an angle θ in respect to the optical axis of the crystal, the so called ordinary and extraordinary waves propagate with different indices. The refractive index of the extraordinary wave $n'_e(\theta)$ can be written as:

$$\frac{1}{n_e'^2(\theta)} = \frac{\cos^2\theta}{n_o^2} + \frac{\sin^2\theta}{n_e^2}, \quad (2.19)$$

where n_o and n_e are the ordinary and extraordinary refractive indices. By choosing the angle properly, phase-matching can be achieved.

2.2 Few-Cycle OPCPA Laser System

The Optical Parametric Chirped-pulse Amplification (OPCPA) is a combination of Optical Parametric Amplification (OPA) and Chirped Pulse Amplification (CPA). OPA is a common approach to amplify laser pulses, similar to DFG introduced earlier—an intense short wavelength pump is used to amplify a longer wavelength

signal. For energy conservation, a third wave, the idler is emitted as well. The photon energies of the three waves, which are pump, signal and idler, fulfill energy conservation (i.e. $\hbar\omega_p = \hbar\omega_s + \hbar\omega_i$). The parametric process does not require a physical state, meaning that there is no real absorption, which may lead to heat dissipation. Chirped pulse amplification (CPA) for optical laser pulses has been demonstrated in 1985 [26]. A pulse is first stretched by introducing dispersion before being amplified. After amplification, the pulse is compressed down to a powerful and short pulse. Both advantages from OPA and CPA are included in OPCPA⁸ [27].

2.2.1 Noncollinear Optical Parametric Amplification (NOPA)

In general, OPA is implemented in a collinear geometry meaning that all pump, signal and idler propagate along the same direction. However, collinear OPA systems do not allow to amplify pulses with duration below 30 fs [28]. In order to amplify a few-cycle laser pulse, noncollinear geometries are more efficient [29–31]. This technique, called noncollinear optical parametric amplification (NOPA), is used for the high repetition rate laser system in this thesis work. The two types of geometries for achieving phase matching are illustrated in figure 2.5, collinear (a) and noncollinear (b).

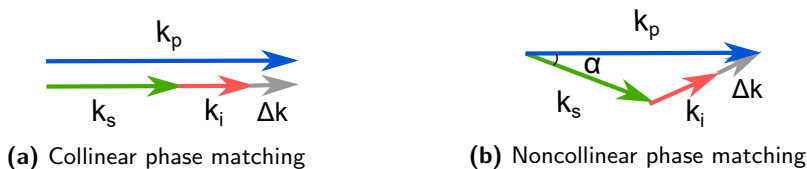


Figure 2.5: Two types of phase matching geometries are used in OPA.

The OPA (DFG) wavevector k mismatch is similar to equation 2.18,

$$\Delta \mathbf{k} = \mathbf{k}_p - \mathbf{k}_s - \mathbf{k}_i \quad (2.20)$$

where \mathbf{k}_p denotes to the pump wave vector, \mathbf{k}_s and \mathbf{k}_i are the signal and idler wave vectors, respectively. In the noncollinear geometry, we have

$$\Delta k = \sqrt{k_p^2 + k_s^2 - 2k_p k_s \cos \alpha} - k_i, \quad (2.21)$$

where α is the angle between the pump and signal wavevectors. We now want to minimize Δk over a broad bandwidth with respect to the angle θ (equation 2.19) and α . Using the Sellmeier equations to calculate the ordinary and extraordinary refractive indices of BBO, the optimized angles are found to be $\alpha = 2.4^\circ$ with $\theta = 24.35^\circ$ [32]. The gain curve for a 1 mm thick BBO crystal is shown in figure 2.6 (b) for $\alpha = 2.4^\circ$ and a pump wavelength of 515 nm.

⁸In our laser system, we perform dispersion management instead of stretching the seed pulse before each optical amplification stage. This is also categorized as OPCPA in a general definition.

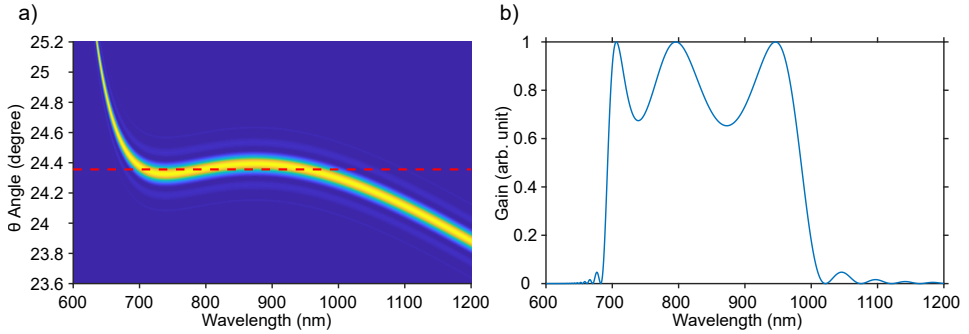


Figure 2.6: Phase-mismatch and gain for a fixed angle ($\alpha = 2.4^\circ$) between the 515 nm pump and the amplified signal. (a) Phase mismatch (b) Normalized signal gain at the angle $\theta = 24.35^\circ$.

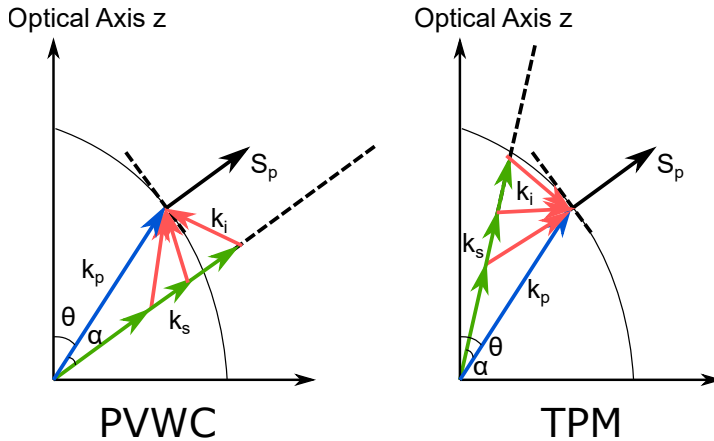


Figure 2.7: Schematic drawing of two phase matching conditions, i.e. Poynting Vector Walk-off Compensation (PVWC) and Tangential Phase Matching (TPM). Both configurations satisfy broadband phase matching as illustrated with the different red and green arrows.

In a noncollinear geometry, phase matching leads to a signal (k_s) in the same direction while the idler (k_i) is angularly dispersed. This can be seen in figure 2.7 (adapted from [33]). There are actually two configurations for satisfying phase matching. The Poynting Vector Walk-off Compensation (PVWC) is used to minimize the angle between signal wave vector k_s and the Poynting vector of the pump S_p , giving an efficient amplification. Another solution is Tangential Phase Matching (TPM). The Poynting vector S_p is moving away from the signal, such that spatial overlaps between the pumps and signal beams may be challenging to sustain in particular for small beams. Thus, the PVWC solution is chosen for our

laser system.

2.2.2 Experimental Setup

The OPCPA system in Lund is shown in figure 2.8. It contains three main units: a seed laser from a CEP stabilized Ti:Sapphire oscillator (VENTEON) shaped by a pulse shaper, a pump laser with a fiber based pre-amplifier and a Yb-doped rod-type final amplifier. The final unit is a two-stage NOPA for broadband amplification.

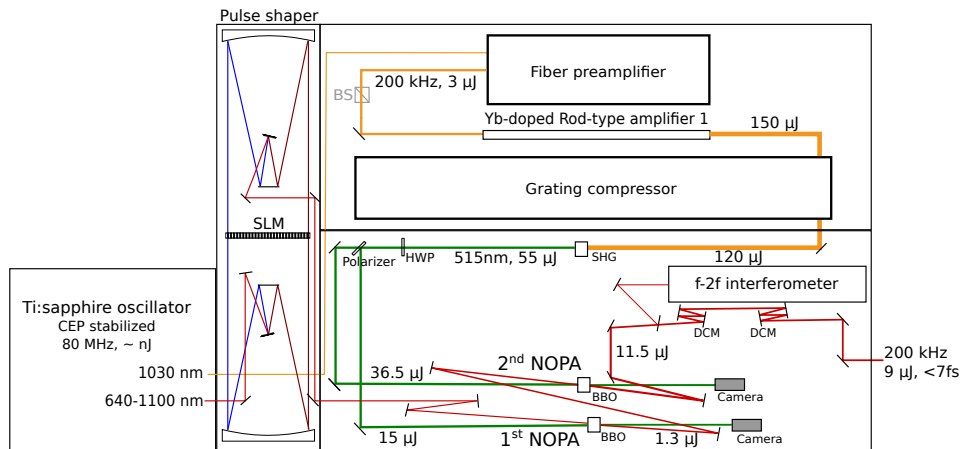


Figure 2.8: The OPCPA laser system built in Lund serves as a high repetition rate ultrafast laser source. SLM denotes to spatial light modulator, HWP means half-wave plate, DCM stands for double-chirped mirrors.

The Ti:Sapphire oscillator produces a broad spectrum spanning more than an octave. The spectrum is broad enough for performing CEP stabilization with f-2f interferometry, from which a feedback signal for the controller of the oscillator's pump laser is derived. Thus, the oscillator's CEP can be stabilized by modulating the oscillator pump for fine tuning and by translating a wedge pair for rough tuning. The oscillator has sufficient spectral bandwidth to provide seed pulses supporting < 7 fs duration around 800 nm, but also provides seed pulses at 1030 nm for the Yb-fiber amplifier chain. This approach is called optical synchronization, which is much easier than synchronizing two lasers electronically.

The 1030 nm seed is filtered by a dichroic mirror from the oscillator spectrum and coupled into a fiber based stretcher. We use a chirped fiber Bragg grating as a stretcher since the last laser upgrade. After the pulses are stretched, the beam is amplified to 600 mW at 200 kHz with a preamplifier consisting of three amplifier sections and two pulse pickers (1/40 and 1/10 repetition rate reduction). The output of the preamplifier is split into two for seeding two rod-type fiber amplifiers. They deliver around 30 W of output power before compression, but

only one of the amplifiers was used during the experiments. The rod-type fiber amplifiers (NKT Photonics) are Yb-doped, 80 cm long and pumped continuously at 972 nm. A grating compressor with about 80% efficiency compresses the output pulses to 350 fs. By second harmonic generation, the compressed pulse is frequency doubled with a 1 mm thick β -barium borate (BBO) crystal, resulting in 55 μJ (11 W) output at 515 nm for pumping two NOPA stages.

Before parametric amplification, the seed from the oscillator can be manipulated with a spectral phase shaper. The shaper is designed in a 4f geometry with a spatial light modulator (SLM, Jenoptik) placed in the Fourier plane. The SLM can change the spectral phase of different frequency components to manipulate the seed of the NOPA. The parametric amplification consists of two NOPA stages. The output is CEP-stabilized with a f-2f based slow loop acting on the oscillator. Alternatively, the shaper or wedges could be used for stabilizing the CEP. The two NOPA stages are set to the phase matching angle $\theta = 24.35^\circ$ and pumped with 3 and 7.3 W of the 515 nm light, respectively. The seed gets amplified from 10 mW (0.125 nJ @ 80 MHz) to 260 mW (1.3 μJ @ 200 kHz) in the first stage NOPA, and the second stage amplifies further to 2.3 W (11.5 μJ). The overall conversion efficiency of the NOPA is around 22%, which is a typical efficiency in such an OPCPA system [34–37]. The final output is compressed by two sets of double-chirped mirrors (DCM7, DCM11, VENTEON), and delivers 9 μJ , sub-7 fs ultrabroad band, high repetition rate ultrashort pulses.

The rod-type amplifiers have recently been upgraded with the goal to obtain better mode quality and higher power. The rod length was changed from 80 cm to 100 cm with less doping (NKT photonics), which is targeted for higher power with less self-phase modulation (SPM) distortion. The current status is a compressed final 1030 nm output up to 175 μJ (35 W), and the second harmonic pulse energy is 90 μJ (18 W), resulting in a 2-stage NOPA output of 13.4 μJ (2.67 W) after pulse compression. In short, the OPCPA is now about 50 % more powerful than the version used for the experiments presented in the thesis.

2.2.3 Characterization

Femtosecond pulses with broad bandwidth are usually challenging to characterize. There are several common optical pulse characterization techniques, such as autocorrelation, FROG [38], SPIDER [39], MIIPS [40], 2DSI [41] etc... Each technique has advantages and disadvantages [42]. In this thesis work, the femtosecond pulses are characterized with the technique called dispersion scan (d-scan). The d-scan technique was developed in a collaboration of Lund University and Porto University in 2012 [43], and it is based on manipulating the spectral phase while recording the SHG spectrum. The experimental setup of the d-scan is simple and robust (figure 2.9). It consists of a chirped mirror pair, a wedge pair, focusing optics, a nonlinear BBO crystal for SHG, and a spectrometer. The dispersion of the pulse is usually overcompensated to negative chirp with a chirped mirror pair before sending it into the wedge pair. After the pulse passing through the wedge pair, the laser pulse is focused into a thin BBO crystal ($\sim 10 \mu\text{m}$) to generate a SHG

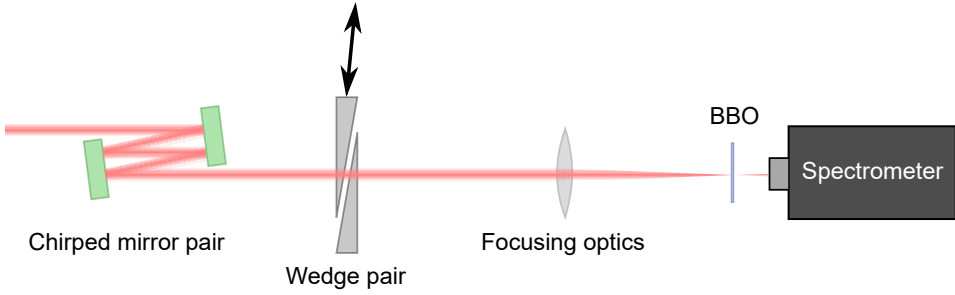


Figure 2.9: Dispersion scan (d-scan) setup. The unknown femtosecond pulse is pre-chirped with a chirped mirror pair and sent into an adjustable wedge pair, and then the laser pulse is focused into a BBO crystal for measuring second harmonic signal with a spectrometer.

signal, which is recorded and analyzed with a spectrometer⁹. The dispersion of the laser pulse is varied by changing the glass insertion of the wedge pair, and the SHG signal will be strongly affected when the laser pulse is not the most compressed. Under different glass insertions, the SHG spectra are measured and recorded in a 2D spectral-dispersion trace (figure 2.10 (a)).

To retrieve the pulse from the measured 2D trace, an algorithm is required. Here, we introduce the procedure for pulse retrieval with a relatively simple algorithm. The unknown pulse can be represented as a function of frequency $\tilde{A}(\omega)$. After passing through an additional glass material with thickness l , the pulse becomes:

$$\tilde{A}(\omega, l) = \tilde{A}(\omega) \exp [ik(\omega)l], \quad (2.22)$$

which contains a 2D information as a function of frequency and glass insertion. The pulse can be retrieved from the SHG trace with iterative steps as shown in figure 2.11. The first step is to guess an electric field in spectral representation $\tilde{A}(\omega)$, and then create a function $\tilde{A}(\omega, l)$ by multiplying the phase introduced from the glass insertion $\exp(i\phi(\omega, l))$. After performing the inverse Fourier transform, the temporal profile $A(t, l)$ is used for generating on SHG field $\tilde{A}_{\text{SHG}}(\omega, l)$. The amplitude $\sqrt{\tilde{A}_{\text{SHG}}(\omega, l)}$ is replaced by the measured trace $\sqrt{\tilde{A}_{\text{meas}}(\omega, l)}$, where the phase $\exp(i\text{Arg}\{\tilde{A}(\omega, l)\})$ is kept. The temporal function of the fundamental pulse can be obtained by multiplying with the complex conjugate of $A(t, l)$ (see figure 2.11). The last step is to remove the spectral phase introduced from glass insertion, and a new fundamental electric field $\tilde{A}(\omega)$ is obtained. The iteration will stop when the error between the experimental trace and the retrieved trace is less than a given threshold. More practical issues are considered and discussed in [44].

While d-scan traces can be very complicated, the shortest pulse is usually obtained for the glass insertion such that the SHG signal is broadest and most intense.

⁹We use an identical achromatic lens to have the same focusing condition as in high harmonic generation, which will be introduced later.

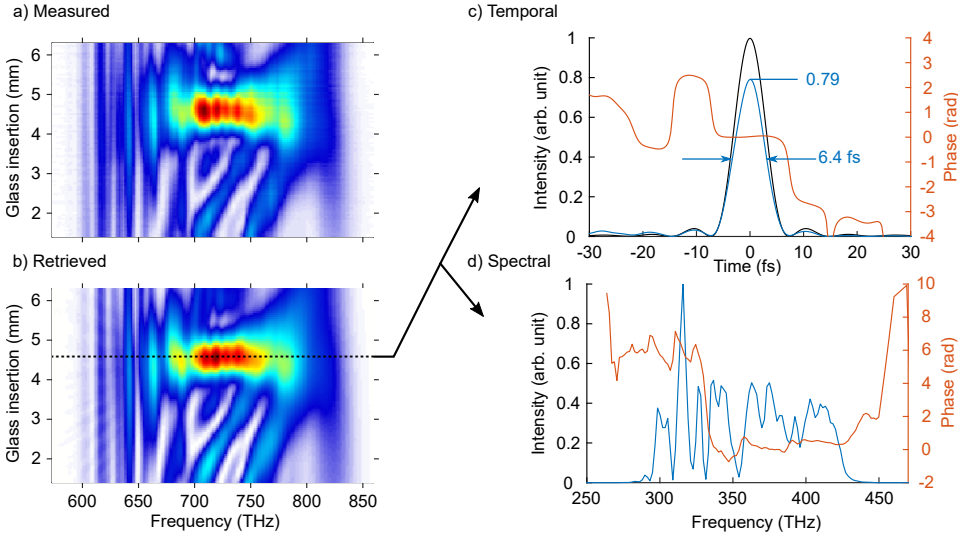


Figure 2.10: D-scan measurement of a pulse from the 2nd NOPA. (a) measured and (b) retrieved d-scan trace. (c) and (d) show the retrieved temporal and spectral profiles (blue) and phase (red). The retrieved pulse duration is 6.4 fs, and the maximum peak intensity is 0.79 of the ideal transform-limited pulse (shown in black).

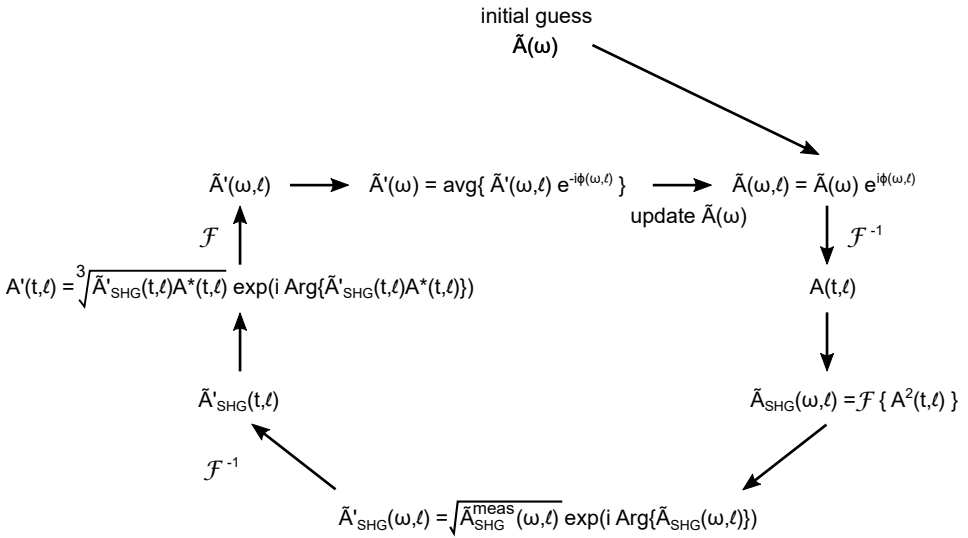


Figure 2.11: The iterative steps of the pulse retrieval algorithm.

In figure 2.10, the most compressed pulse with the broadest spectrum is obtained around 4.6 mm glass insertion, giving ultrashort 6.4 fs pulses. If the d-scan trace

is tilted, it corresponds to higher-order phase effect, which can be compensated by manipulating the phase of the seed beam with the shaper.

Spatio-Temporal Coupling

The d-scan characterization technique assumes a transversely homogeneous distribution, which is often not valid for ultrashort pulses. The dependence of the temporal (spectral) properties of ultrashort pulses on the transverse spatial (angular) coordinates is referred to as spatio-temporal coupling. For example, the spectral amplitude becomes spatially-dependent as:

$$\tilde{A}(x, y, \omega) \exp(i\phi(x, y, \omega)), \quad (2.23)$$

where x, y are the spatial coordinates in the transverse plane. A spatially-resolved Fourier transform interferometric technique has been used to characterize the pulses from the NOPA and is presented in Paper I. The method does neither require non-linear optics nor another reference pulse [45], so it is quite suitable to characterize ultrashort pulses both spatially and spectrally. The idea is to interfere a homogeneous reference pulse with the one to be characterized on the sensor of a camera, while scanning the delay between the two pulses. By this procedure, the interference between the reference and the pulse to be characterized is recorded for every pixel of the camera.

The experimental setup is shown in figure 2.12. First, the center of the beam is selected and a d-scan characterization is performed. Then, the unknown pulse is split into two beams after the first beam splitter. The reference is created by spatially filtering in one arm of the interferometer, and letting the beam expand to overfill the camera. By varying the time delay τ , the interference patterns are recorded in a 3D matrix (x, y, τ) .

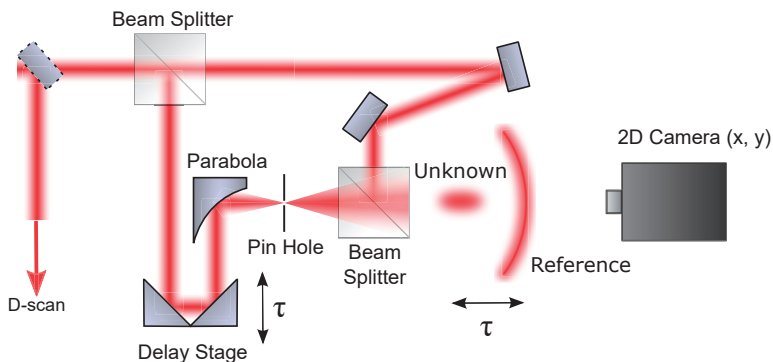


Figure 2.12: Spatial-temporal coupling measurement setup to characterize an unknown pulse using a Mach-Zehnder interferometer configuration (adapted from [45]).

The measured 3D intensity matrix $I(x, y, \tau)$ is:

$$I(x, y, \tau) = \int_{-\infty}^{\infty} dt |A(x, y, t) + A_r(x, y, t - \tau)|^2 \quad (2.24)$$

Performing a Fourier transform of equation 2.24, the expression becomes:

$$F\{I(x, y, \tau)\} = F\left\{\int dt |A(x, y, t)|^2 + \int dt |A_r(x, y, t)|^2\right\} \\ + \tilde{A}(x, y, \omega)\tilde{A}_r^*(x, y, \omega) + \tilde{A}^*(x, y, -\omega)\tilde{A}_r(x, y, -\omega) \quad (2.25)$$

These terms can be separated in the frequency domain. Conventionally, the second term (the first cross term) is chosen for characterizing the unknown pulse $\tilde{A}(x, y, \omega)$, assuming a known reference pulse.

For most applications of our OPCPA, we need to be able to focus our output beam into the smallest possible spot size and highest possible intensity. In Paper I, the measurement was done at the far field of the NOPA output, so the measured beam needs to be propagated to the focus in order to determine the focused intensity. Assuming that Fraunhofer diffraction is valid, the distributions at focus and the far-field can be connected by a spatial Fourier transform. An ideal focal distribution is compared to the actual retrieved beam in figure 2.13. The 3D iso-surface plot indicates by different colors 10%, 40%, 70% of the maximum signal on both pictures, and the projections on three different planes show the distribution spatially and temporally. The intensity ratio between the actual peak and the ideal one is defined as Strehl ratio. It is clear that the distribution of the actual beam is more spread leading to a Strehl ratio of 0.71. This analysis did not include the spectral phase of the reference pulse, but just assumed a flat spectral phase. If we use the measured spectral phase of the reference pulse, the Strehl ratio drops to 0.5.

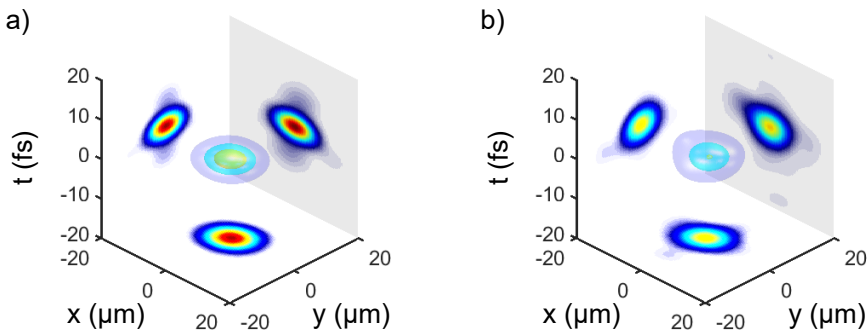


Figure 2.13: The spatio-temporal coupling measurement from the 2nd NOPA stage. (a) The ideal condition without any spatio-temporal coupling. (b) The actual retrieval with the spatio-temporal phase.

In practice, aligning NOPA stages just for power can result in significant spatio-temporal coupling, such that the focal intensity will drop. More about possible misalignment of the NOPA stages, also showing an impact on the spatio-spectral distribution and the final focal intensity, is presented in Paper [I](#).

2.3 Application — Polarization Dependence of Multiphoton Induced Electron Emission from Nanostructures

The laser system has been directly used for an application, described in Paper [VI](#), and briefly summarized here. The multiphoton induced electron emission from semiconductor nanowires has been studied as a function of the polarization direction of the incident IR pulses. The semiconductor nanowires are composed of InAs with two crystal structures, cubic zincblende (ZB) and hexagonal wurtzite (WZ). The work function of InAs is similar to gold. In both materials, the photoemission signal was recorded as a function of laser intensity and found to vary as the laser power to the power of 4, indicating that the multiphoton process requires about 4 photons to emit photoelectrons.

2.3.1 Detection Instrument and Experimental Setup

The instrument used for imaging the photoelectrons is a PhotoEmission Electron Microscope (PEEM), which provides spatial resolution of the sample surface. The schematic of the PEEM setup (from FOCUS GmbH) is presented in figure [2.14](#). The resolution of the PEEM is down to 40 nm with a few-tens of micrometers field of view. The laser beam was sent with 65° incident angle onto the sample, and the photoelectrons generated from multiphoton ionization are collected with the PEEM. The polarization of the laser field is controlled with an achromatic half-wave plate.

The PEEM experiments greatly benefit from using a high repetition rate few-cycle laser system. The first advantage is that space-charge effects can be suppressed due to high repetition rate but low pulse energy. The space-charge effect comes from densely generated photonelectrons, particularly when using ultrashort pulses as the light source, such that electrons repel each other causing a blurred image, i.e. lower spatial resolution. At high repetition rate thus, the image acquisition time can be reduced while the image quality is maintained [\[46\]](#). Another advantage is that few-cycle laser pulses can avoid unwanted photoemission signals due to the changes of optical properties, such as heating of the lattice or creating hot electrons by filling the conduction band [\[47\]](#), which occurs after a few hundred femtoseconds following the excitation.

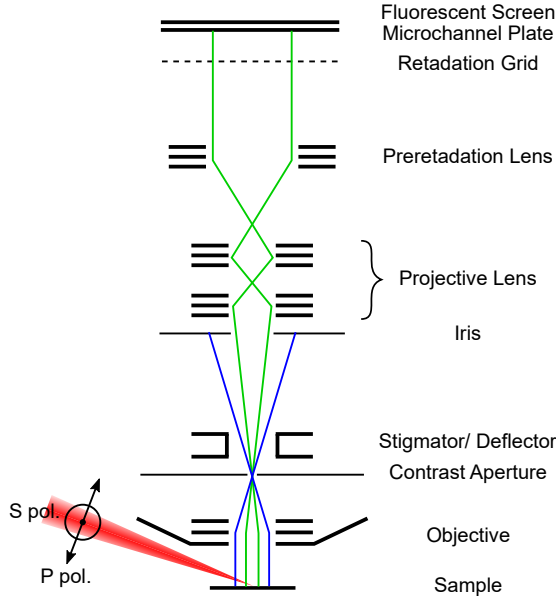


Figure 2.14: Schematic drawing illustrating the PEEM instrument used in the experiment. The incident IR beam varies between p polarization and s polarization during the measurement.

2.3.2 Numerical Approach

The commonly used method for simulating photoemission from nanostructures is the finite-difference time domain (FDTD) method, a numerical technique based on solving Maxwell's equations [48–50]. However, FDTD simulations do not predict a pronounced polarization dependence of the photoemission of the InAs nanowires. An alternative method was developed by using a microscopic description for the electron transitions between band structures. It is assumed that the photon absorption and emission are independent, such that any anisotropic photoabsorption should result in the polarization-dependent photoemission. The transition requires at least three photon absorption before the electron is emitted. If the electron transition between band structure is anisotropic, the following electron emission should have a polarization dependence. The electron transition probability between the valence band (v) and the conduction band (c) can be expressed with the dipole approximation¹⁰ [51]:

$$P_{v\mathbf{k}\rightarrow c\mathbf{k}} = \frac{2\pi}{\hbar} (eE_0)^2 |\langle \psi_{c\mathbf{k}} | \mathbf{e} \cdot \mathbf{r} | \psi_{v\mathbf{k}} \rangle|^2 \delta(E_c(\mathbf{k}) - E_v(\mathbf{k}) - \hbar\omega), \quad (2.26)$$

¹⁰The SI unit is shown here, but the reference is in Gaussian unit.

where E_0 is the amplitude of the driving field, \mathbf{k} is the wavevector, and \mathbf{e} is the polarization unit vector. $E_c(\mathbf{k})$ and $E_v(\mathbf{k})$ are the energies of the conduction band and valence band at the wavevector \mathbf{k} . The calculation needs to sum up all the contributions from various valence bands to conduction bands, so the single photon transition is written as:

$$W(\omega, \mathbf{e}) = \frac{4\pi}{\hbar} (eE_0)^2 \sum_{c\mathbf{k}} |\mathbf{e} \cdot \mathbf{M}_{cv}(\mathbf{k})|^2 \delta(E_c(\mathbf{k}) - E_v(\mathbf{k}) - \hbar\omega), \quad (2.27)$$

where $\mathbf{e} \cdot \mathbf{M}_{cv}(\mathbf{k})$ is the density matrix elements $\langle \psi_{c\mathbf{k}} | \mathbf{e} \cdot \mathbf{r} | \psi_{v\mathbf{k}} \rangle$. The additional factor 2 originates from counting the spin. In Paper VI, equation 2.27 is generalized to two and three-photon transitions. The final total transition rate is the integral of all frequencies, i.e.

$$W(\mathbf{e}) = \int d\omega W(\omega, \mathbf{e}), \quad (2.28)$$

with the incident laser spectral shape assumed to be a rectangular shape with 1 eV bandwidth from 1 eV to 2 eV.

2.3.3 Polarization-Dependent Photoemission

The photoemission of InAs nanowires was studied as a function of the polarization of the excitation laser field. We investigated different orientation of the nanowires and found that when the nanowire is almost perpendicular to the incident plane of the light, the photoemission variation between the polarizations can be maximized. In this case, the segment of WZ crystal attached to the gold seed has the photoemission maximum when the laser field is close to s-polarization. When the laser is close to p-polarization, the rest of the segments, gold seed, ZB segment, and another WZ segment have the photoemission maxima. Note that the free ended WZ segment (“lower” segment in Paper VI) has a more complicated polarization dependence.

The behavior of the first segment of WZ can be understood from the simulations of the multiphoton transition. The three-photon transition in WZ shows an anisotropic polarization dependence, which is likely to be still anisotropic as the electrons are emitted in the next ionization step. The simulation of ZB shows an isotropic multiphoton transition which supports the emission of the observation in the experiment. The complicated polarization dependence of the free-ended WZ segment could be understood from the surface effects due to different surface structure of two WZ segments in the growth process.

2.4 XUV attosecond light source

The term “XUV attosecond light source” usually refers to pulses generated from high harmonic generation (HHG). The generation of high harmonics is driven by intense visible or infrared laser pulses. It was first reported in the late 1980s

[52, 53]. We will use the semiclassical three-step model [54, 55] for describing the generation and properties of attosecond pulses emitted by a single atom. Then, the macroscopic response of an ensemble of atoms will be briefly described. The experimental setup used in this thesis for producing HHG light is shown afterwards. In the final part, the influence of dispersion of the IR field will be discussed.

2.4.1 Microscopic — Classical Three-Step Model

High harmonic generation on the microscopic scale (single-atom response) can be understood by the three-step model, which consists of tunnel ionization, propagation of the free electron in the laser field, and recombination. When an intense fundamental laser pulse is focused into a nonlinear medium, the electric field can be strong enough to pull out an electron from the atom. After the electron gets ionized, the Coulomb potential from the nucleus can be neglected. In this simple classical model, the nucleus and the electron are treated as two classical point particles, but only the electron moves along with the electric field. Since the electric field is oscillatory, the electron may turn back and recollide with the parent ion. This depends on the time when the electron gets ionized. If the electron recombines with its parent ion, it will emit its excess energy as a photon with energy equal to the electron kinetic energy (E_k) and the ionization potential (I_p).

The three-step model starts from solving the classical equations of motion:

$$\ddot{x}(t) = -\frac{eE(t)}{m_e}, \quad (2.29)$$

where e and m_e are electron charge and mass, respectively. The electric field is a sinusoidal wave $E(t) = E_0 \sin(\omega_0 t)$, where ω_0 is the oscillation frequency of the electric field. By integrating equation 2.29 twice, we can obtain the electron velocity and position:

$$v(t) = \frac{eE_0}{m_e\omega_0} [\cos(\omega_0 t) - \cos(\omega_0 t_i)], \quad (2.30a)$$

$$x(t) = \frac{eE_0}{m_e\omega_0^2} [\sin(\omega_0 t) - \sin(\omega_0 t_i) - \omega_0(t - t_i) \cos(\omega_0 t_i)], \quad (2.30b)$$

where t_i is the ionization time. When the position of the electron $x(t)$ is equal to 0 again, it means that the electron may recombine with the nucleus. The kinetic energy of the electron becomes:

$$E_k = \frac{m_e |v(t)|^2}{2} = 2U_p [\cos(\omega_0 t) - \cos(\omega_0 t_i)]^2, \quad (2.31)$$

where the ponderomotive potential U_p is proportional to the intensity of the laser field I .

$$U_p = \frac{e^2 E_0^2}{4m_e \omega_0^2} = \frac{e^2 \lambda^2 I}{8\pi^2 m_e \epsilon_0 c^3} \quad (2.32)$$

The maximum kinetic energy is $3.17U_p$, so the emitted photon energy is:

$$E_{\text{photon}} \leq I_p + 3.17U_p \quad (2.33)$$

The maximum value is also called cut-off energy in the single atom picture. Figure

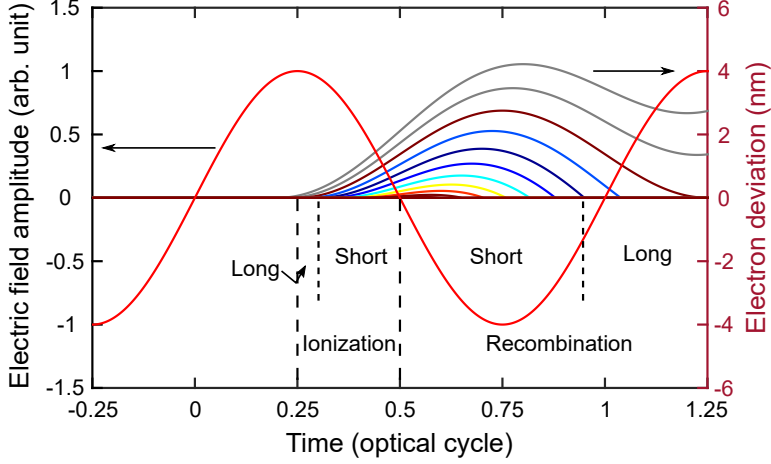


Figure 2.15: Schematic picture of classical electron trajectories within the three step model. Grey lines indicate trajectories without recombination, and different colors represent different kinetic energies of the returning electrons. The electron deviation from the nucleus is calculated for a driving laser intensity of $2.5 \times 10^{14} \text{ W/cm}^2$.

2.15 illustrates the electron trajectories. The electron gets ionized within $[0, 0.5]$ T, where T is the optical cycle. If the electron gets ionized earlier than the peak of the electric field ($t = 0.25$ T), it will never come back to recombine. Two families of electron trajectories, born between 0.25 T and 0.5 T can be identified: the short trajectory and the long trajectory. The long trajectory electrons are ionized earlier ($[0.25, 0.3]$ T) and then recombine after 0.95 T. On the other hand, the short trajectory electrons get ionized later ($[0.3, 0.5]$ T), and recombine before 0.95 T. It should be noted that different emitted wavelengths correspond to different return times, such that generated pulses are therefore usually chirped. Despite of the chirp, the generated pulses are usually less than 1 fs, leading to the name of attosecond pulses. The three step process occurs in every half cycle of the IR field (e.g. 1.3 fs for 800 nm IR field), so the attosecond pulses are separated in time by half the laser cycle.

Intensity-Dependent Dipole Phase

The single-atom response can also be treated in the framework of the strong-field approximation (SFA), which is a fully quantum mechanical treatment [56]. The SFA calculates the intensity-dependent amplitude and phase of the generated

attosecond pulses [57]. The so called dipole phase can also be derived from the classical trajectories (Paper II). Figure 2.16 shows, the electron recombination energy as function of ionization time ($[0.25 \ 0.5] \text{ T}$) and recombination time ($[0.5, 1.25] \text{ T}$). We now present an approximated expression of the dipole phase and concentrate on the recombination region.

Two straight lines tangent to the kinetic energy at half of its maximum cross the lowest (0) and the highest energy ($3.17 U_p$) with four temporal intersection points, $t_{ps}, t_{pl}, t_{cs}, t_{cl}$. The values of these four points are: $t_{ps} = 0.6784 \text{ T}$, $t_{pl} = 1.1935 \text{ T}$, $t_{cs} = 0.9006 \text{ T}$, $t_{cl} = 1.0048 \text{ T}$ ¹¹. Since figure 2.16 is normalized to ponderomotive potential (U_p), the crossing points are intensity independent.

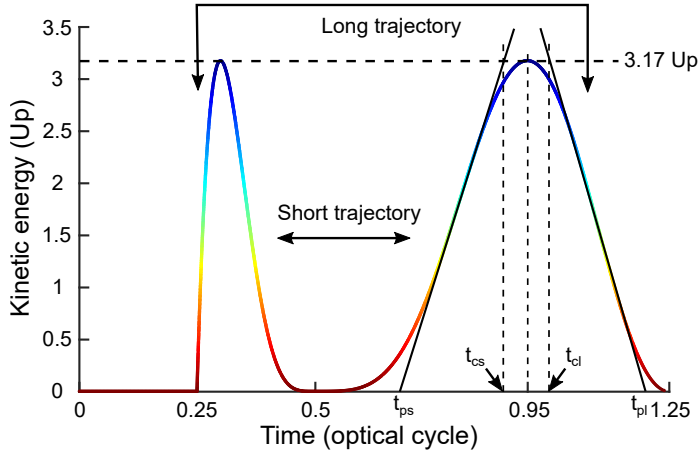


Figure 2.16: Ionization and recombination times for the long and short trajectories. The time before 0.5 optical cycles is the ionization part, and the time after 0.5 optical cycles is the recombination part.

It is assumed that the XUV emission is instantaneous as the electron recombines. By using the linear tangent lines, the group delay (GD) of the different XUV photon frequencies (Ω) can be written as:

$$GD_{(s,l)}(\Omega) = t_{(ps,pl)} + \frac{t_{(cs,cl)} - t_{(ps,pl)}}{\Omega_c - \Omega_p} (\Omega - \Omega_p) \quad (2.34)$$

The frequencies Ω_c and Ω_p denote the cut-off frequency ($I_p + 3.17 U_p$) and the frequency corresponding to the ionization threshold (I_p), respectively. The approximated expression for the dipole phase is obtained by integrating the group delay (equation 2.34):

$$\phi_{(s,l)}(\Omega) = \mathcal{C}_{(s,l)} + t_{(ps,pl)}(\Omega - \Omega_p) + \frac{t_{(cs,cl)} - t_{(ps,pl)}}{2(\Omega_c - \Omega_p)} (\Omega - \Omega_p)^2, \quad (2.35)$$

¹¹The values in Paper II are offset by 0.5 optical cycle since the origin point starts from the beginning of the recombination.

where $\mathcal{C}_{(s,l)}$ is a constant. Since the frequency difference between Ω_c and Ω_p is $3.17 U_p$, the coefficients of the expansion in equation 2.35 can be written in terms of the laser intensity I . The first term in equation 2.35 is proportional to intensity (see Paper II and [58]) so that:

$$\phi_{(s,l)}(\Omega) = \alpha_{(s,l)}I + \beta_{(s,l)}(\Omega - \Omega_p) + \frac{\gamma_{(s,l)}}{I}(\Omega - \Omega_p)^2, \quad (2.36)$$

where $\beta_{(s,l)} = t_{(ps,pl)}$, $\gamma_{(s,l)} = (t_{(cs,cl)} - t_{(ps,pl)})\hbar m_e \omega_0^2 \epsilon_0 c / (3.17 e^2)$. The $\beta_{(s,l)}$ and $\gamma_{(s,l)}$ coefficients are easily determined by the timings $t_{(ps,pl)}$ and $t_{(cs,cl)}$. In Paper II, α_s is assumed to be 0¹². When the α_s is known, the coefficient α_l can be calculated by equating $\phi_s(\Omega)$ and $\phi_l(\Omega)$ at the cut-off frequency Ω_c . It is important to note that, in previous work, the dipole phase has often been approximated as αI [57, 60].

2.4.2 Macroscopic — HHG Phase Matching

The overall XUV generation does not only depend on the single atom response. The driving field and the generated XUV light should remain in phase in the nonlinear medium to have efficient harmonic generation. In other words, the phase mismatch Δk between the fundamental driving field and the generated harmonics needs to be minimized. The phase mismatch Δk for the q^{th} harmonic is defined as¹³

$$\Delta k = qk - k_q, \quad (2.37)$$

where k_q represents the wavevector of the q^{th} harmonic. This phase mismatch consists of four contributions:

$$\Delta k = \Delta k_g + \Delta k_d + \Delta k_n + \Delta k_p \quad (2.38)$$

Δk_g is the geometrical phase mismatch between the fundamental and the q^{th} harmonic. Assuming the beam is Gaussian, Δk_g can be written as:

$$\Delta k_g = -\left(q \frac{\partial \zeta}{\partial z} - \frac{\partial \zeta_q}{\partial z}\right) = -\left(q \frac{1}{z_R + \frac{z^2}{z_R}} - \frac{1}{z_{Rq} + \frac{z^2}{z_{Rq}}}\right) \approx \frac{-q}{z_R + \frac{z^2}{z_R}} < 0, \quad (2.39)$$

where the ζ and ζ_q are the Gouy phase of the fundamental and the q^{th} harmonic, respectively. z_R is the Rayleigh range of the fundamental, and z_{Rq} is the one for the q^{th} harmonic. The Rayleigh range is inversely proportional to the wavelength. If the harmonic number q is large enough, Δk_g can be approximated to only depending on the fundamental contribution. The second term Δk_d is the phase mismatch from the dipole phase, equal on-axis to:

¹²To be accurate, the SFA suggests the short trajectory value is close to 0 with a tiny negative value [59].

¹³The sign of the equation follows the notation of the electric field. If the phase of electric field is defined as $kz - \omega t$, then it has opposite sign in Δk

$$\Delta k_d = \frac{\partial \phi_{(s,t)}(\Omega, z)}{\partial z} = \alpha \frac{\partial I}{\partial z} + \frac{\partial}{\partial z} \frac{\gamma}{I} (\Omega - \Omega_p)^2 = \frac{2\alpha z I_0}{z_R^2 (1 + \frac{z^2}{z_R^2})^2} + 2 \frac{\gamma}{I_0} \frac{z}{z_R^2} (\Omega - \Omega_p)^2. \quad (2.40)$$

The last two terms Δk_n , Δk_p , with opposite sign, are from the neutral gas dispersion and plasma, respectively.

$$\Delta k_n = q \frac{2\pi}{\lambda} (n(\omega) - n(q\omega)) > 0 \quad (2.41)$$

$$\Delta k_p = q \frac{2\pi}{\lambda} (n_p(\omega) - n_p(q\omega)) < 0 \quad (2.42)$$

All four phase mismatch contributions are summarized below:

	Δk_g	Δk_d	Δk_n	Δk_p
Sign	-	$\begin{cases} +, z > 0 \\ -, z < 0 \end{cases}$	+	-

It is worth to note that the dipole phase wavevector mismatch Δk_d changes with the position z and the laser intensity I . In principle, the phase matching condition can be satisfied by adjusting the gas pressure, the position of the medium relative to the focus, and the laser intensity. The short and long trajectories do not have the same phase matching condition, and it is difficult to phase match both trajectories efficiently at the same time. The short trajectories lead to a more collimated beam than the long trajectories [61, 62], such that the HHG is usually optimized for the short trajectories. This has been the case in this thesis work.

Our high-repetition-rate laser system for generating HHG has a pulse energy of several orders of magnitude less than conventional Ti:Sapphire lasers. Fortunately, a scale invariance of HHG can maintain the conversion efficiency with different pulse energies [63, 64]. This can be understood with figure 2.17.

We know that the intensity for generating high harmonics should be maintained when scaling. When the input pulse energy is scaled by η^2 (in our case $\eta < 1$), the focal spot D should be multiplied by the factor η^2 by scaling the focal length of the focusing element with η . Meanwhile, the interaction length L , related to the Rayleigh range z_R as well as the longitudinal coordinate z , will be scaled by η^2 . The new phase mismatch $\Delta k'$ is equal to

$$\begin{aligned} \Delta k' &= \Delta k'_g + \Delta k'_d + \Delta k'_n + \Delta k'_p \\ &= \frac{\Delta k_g}{\eta^2} + \frac{\Delta k_d}{\eta^2} + \frac{\rho'}{\rho} (\Delta k_n + \Delta k_p) \end{aligned} \quad (2.43)$$

To preserve the phase matching condition ($\Delta k \approx 0$), the pressure ρ' can be set to ρ/η^2 . Note that the number of atoms participating the harmonic generation N_{HHG} is determined by the interaction volume ($\propto z_R \times D^2$) and the gas density ρ . After the scaling, N_{HHG} is scaled by η^2 . The total HHG output energy is also scaled by the same factor η^2 and the conversion efficiency is then unchanged.

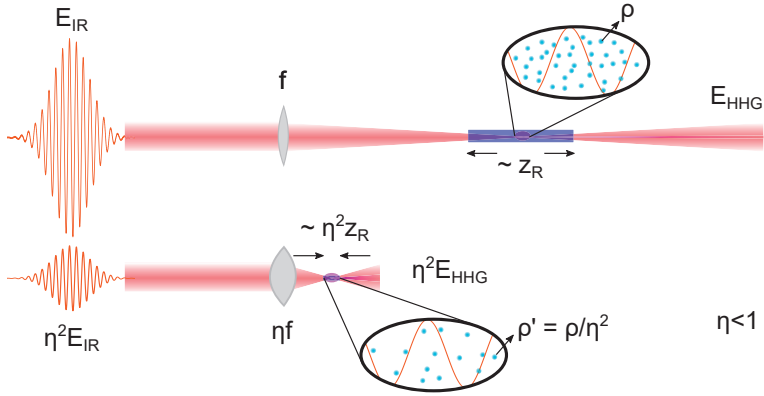


Figure 2.17: Schematic drawing, illustrating the HHG scale-invariant properties. As the input energy is scaled with η^2 , the rest of the parameters need to be changed with the proper scaling factors.

2.4.3 Experimental Setup — HHG Light Source

The high harmonic generation setup for the high repetition rate laser in Lund is made of two parts, presented in figure 2.18. The first part (left side) is dedicated to the generation. The laser beam is focused with an achromatic lens ($f = 50$ mm) into a continuous high-pressure gas jet. For light focusing, an achromat is better suited than a curved mirror and much easier to align than a parabola. The focused intensity is estimated to be more than 10^{14} W/cm² which is required for HHG. The scaling dictates that we need a high pressure and a short gas target. The high-pressure gas jet is composed of an injection nozzle with a 50 μ m diameter orifice and an extraction nozzle with 1 mm opening (Paper I). The gap between the injection and extraction nozzles is about 200 μ m, which is sufficient for the laser beam to pass through and also small enough for the extraction nozzle to capture up to 86% of the gas. According to the scaling properties for HHG, the required target gas pressure is around 1 bar for laser pulses with several μ J to generate HHG with good conversion efficiency. The gas target was simulated with the software package DS2V, which models gas flows with a the Monte Carlo method [65]. The simulation showed that 10 bars of backing pressure leads to the intended 1 bar gas density in the interaction region. With a single 550 L/s turbo pump (Leybold TURBOVAC MAG W 600 iP), the pressure in the vacuum chamber can be kept to some 10^{-3} mbar under operation. This is essential to minimize re-absorption of the generated XUV radiation.

The second part is dedicated to the characterization of the generated radiation. It is separated from the generation chamber by a 50 μ m differential pumping hole for the XUV to propagate through. Right after the differential hole, a filter wheel for selecting XUV spectra with different metallic filters (e.g. aluminum, chromium, iron, and tin) is placed. The XUV is characterized by an aberration-corrected

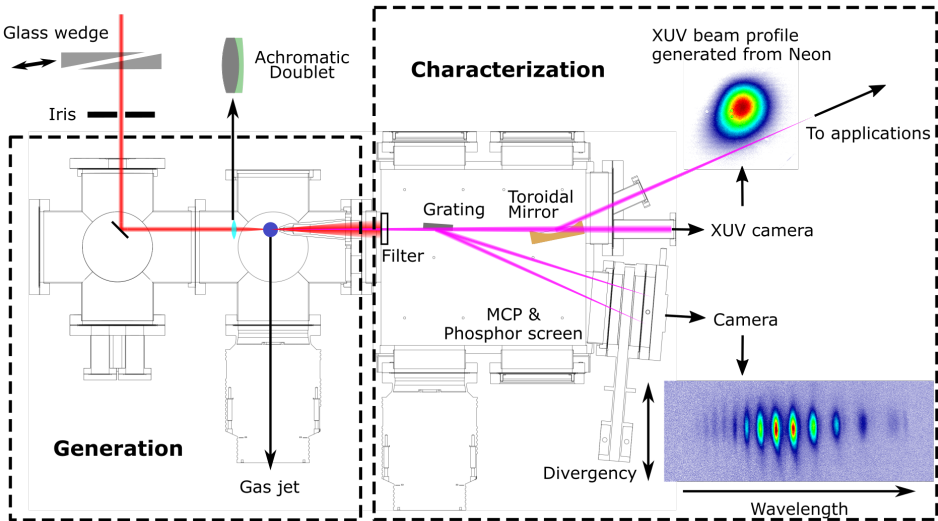


Figure 2.18: Schematic drawing of the high harmonic generation setup for the high repetition rate laser in Lund. It consists of generation and characterization chambers. In the generation chamber, the incident laser is focused with an achromatic lens to a high pressure gas jet to produce XUV via HHG. In the characterization chamber, the XUV can be filtered with metallic filters. The filtered output can be characterized spectrally with a concave grating, or spatially with an XUV camera.

concave XUV grating (Hitachi, 001-0640, 1200 grooves/mm) and detected with microchannel plates (MCP) and a phosphor screen. The fluorescence light from the phosphor screen is recorded by an external camera (Allied Vision, Pike F-505, 14 bit ADC) giving information both on the spatial divergence of the harmonics and on the harmonic spectrum. The XUV output power is characterized with an XUV camera (Andor, Ikon-L). The optimized results for different gas media are summarized in table 2.1. The grating can be removed and a gold-coated toroidal mirror (HORIBA, $f = 300$ mm) focuses the XUV radiation (and the driving IR if no metallic filter is used) through the output port of the chamber with $2f$ - $2f$ imaging for use in different applications. The experiment that we have performed with this light source will be presented in Chapter 4 and Paper IV.

2.4.4 XUV Dispersion Scan

In Paper II, the generated XUV spectra are recorded as a function of the glass insertion of a wedge pair in the path of the fundamental IR field, using the same scanning procedure as for the dispersion scan used to characterize IR pulses (see section 2.2.3). Since the IR pulse duration is only a few cycles, the generated XUV spectra are very sensitive to the IR field. This phenomenon has been observed

XX	Neon	Argon	Krypton
IR pulse energy (μJ)	5.0	3.1	2.2
Backing pressure (bar)	30	10	8
XUV pulse energy (pJ)	0.056	0.155	0.280
XUV flux (10^{10} photons/sec)	0.16	0.5	0.95
Conversion efficiency	4.0×10^{-8}	1.3×10^{-6}	4.2×10^{-6}

Table 2.1: Optimized efficiency of high harmonic generation with different noble gases. Both XUV pulse energy and flux are determined by measurements with the XUV camera. The conversion efficiency is calculated by assuming a 5 nm oxide layer on the aluminum filter, used to shield the XUV camera from the IR.

in many reports [66–69], and also reproduced with models based on the strong field approximation. In this thesis, a multiple interference approach was developed based on the three-step model, providing insight into the phase relation between consecutive attosecond pulses.

As a continuation of section 2.4.1, the overall spectral representation of the attosecond pulse train is the sum of all the attosecond pulses from each half cycle:

$$\tilde{A}_{tot}(\Omega) = \sum_m |A_m(\Omega)| \exp(i[\Omega t_m + m\pi + \Phi_m(\Omega)]), \quad (2.44)$$

where m is the index of the attosecond pulse, and $A_m(\Omega)$ the spectral amplitude of the m th attosecond pulse. The spectral amplitude is assumed to be a super-Gaussian ($n=4$) for every attosecond pulse, and the amplitude is modulated by the ionization and recombination rates. Tunnel ionization is calculated with the Ammosov-Delone-Kraĭnov (ADK) model [70], and recombination is determined from the photoionization cross sections [71]. t_m is the zero-crossing time of the fundamental field, representing the starting time of each attosecond pulse. The first phase term in equation 2.44 comes from the temporal delay between consecutive attosecond pulse, which is equal to a half cycle of the IR field. The second phase term $m\pi$ comes from the opposite sign of consecutive attosecond pulses due to the sign of the IR field changing every half cycle. The last term $\Phi_m(\Omega)$ is the dipole phase term, which has already been discussed in section 2.4.1.

In order to determine the contribution from each pulse, the phase term of equation 2.44 can be rearranged to a polynomial set:

$$\tilde{A}_{tot}(\Omega) = \sum_m |A_m(\Omega)| \exp(i[z(\Omega) + mf(\Omega) + m^2s(\Omega)]), \quad (2.45)$$

where the functions $z(\Omega)$, $f(\Omega)$, $s(\Omega)$ are as following:

$$z(\Omega) = -\frac{\Omega\varphi}{\omega_0} \left(1 + \frac{b\varphi}{2\omega_0^2}\right) + t_p(\Omega - \Omega_p) + \frac{\gamma}{I_{\max}}(\Omega - \Omega_p)^2 \quad (2.46a)$$

$$f(\Omega) = \pi + \frac{\pi\Omega}{\omega_0} + \varphi\kappa(\Omega) \quad (2.46b)$$

$$s(\Omega) = -\frac{\pi\kappa(\Omega)}{2} \quad (2.46c)$$

with the function $\kappa(\Omega)$,

$$\kappa(\Omega) = \frac{b\pi\Omega}{\omega_0^3} - \frac{2\pi\gamma}{\omega_0^2\tau^2 I_{\max}}(\Omega - \Omega_p)^2. \quad (2.47)$$

These phase terms are dependent on the peak intensity I_{\max} , the chirp rate of the fundamental field b , the CEP φ ¹⁴, and the pulse duration τ of the fundamental field. The first phase term $z(\Omega)$ is a constant phase term and independent from the number of pulses. The second term $f(\Omega)$ provides the same phase difference between consecutive attosecond pulses, which is equivalent to multiple slit interference in time. This term results in the fringes observed in the XUV dispersion scan (figure 2.19), changing periodically for every π CEP. The yellow lines in figure 2.19 show that $f(\Omega)$ is the main contribution to the interference structure of the XUV dispersion scan. The last term $s(\Omega)$ is a higher-order phase term, which partially smears the interference structure. In the temporal domain, it leads to a distortion of the attosecond pulse train.

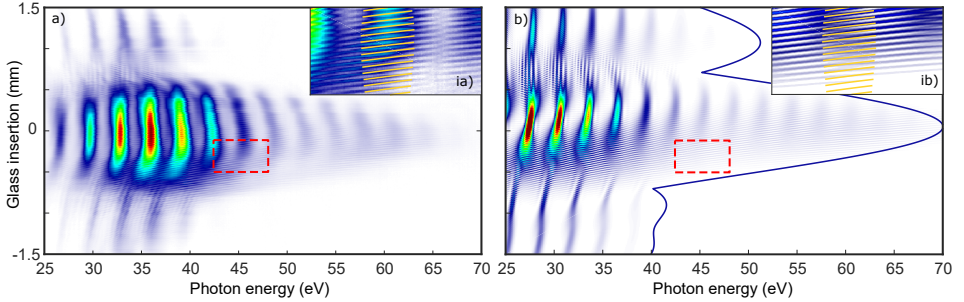


Figure 2.19: Dispersion scan of HHG spectra generated in argon (a) measured and (b) simulated. The dashed boxes are zoomed in the insertion plots (ia), (ib) on the top right corners. Yellow lines show the calculation from the first order term $f(\Omega) = 32\pi$ in equation 2.45. The blue curve in (b) indicates the classical cut-off estimated from the intensity of the fundamental pulse. (plot from Paper II)

In Paper IV, an asymmetry of the photoemission distribution is observed along the light polarization under a CEP scan of the fundamental IR. To investigate the

¹⁴The conventional way to define CEP is from a cosine wave, but the derivation is from a sine function. It will introduce a $\pi/2$ offset between φ and CEP.

interference between photoelectron wave packets, the presented multiple interference model provides accurate information on the relative phase of the attosecond pulses. The attosecond pulse trains used in this experiment are discussed in the next section, while the photoionization results will be presented in Chapter 4.

2.4.5 XUV attosecond pulses

In Paper IV, the XUV spectrum is studied as a function of IR dispersion with finer scanning steps (figure 2.20).

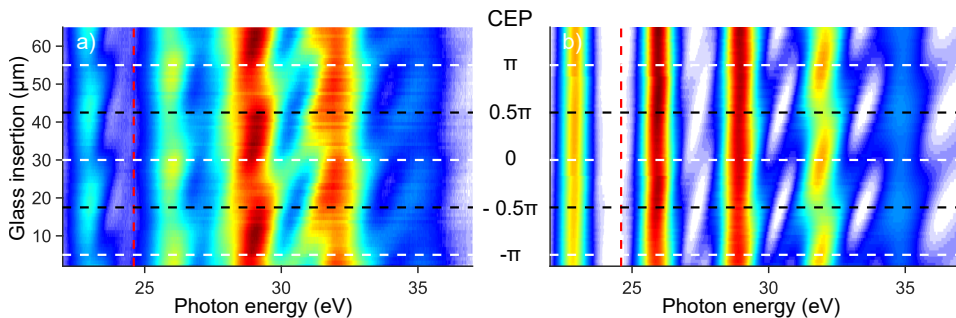


Figure 2.20: Dispersion (glass insertion thickness) scan of XUV spectra generated in argon: (a) experiment and (b) simulation. The red dashed line represents the ionization threshold of helium (24.6 eV), which is used as the gas target for the photoionization experiment. The dashed white and black lines correspond to the CEPs equal to a multiple of π and of $\pi/2$, respectively.

The experimental spectra are recorded around the most compressed IR pulse, and the simulation uses 1.1×10^{14} W/cm² as IR laser intensity. The highest observable harmonic in the spectrum is the 23rd at ~ 35 eV¹⁵. Due to the few-cycle IR driving field, the generated attosecond pulses are sensitive to the CEP of the driving field [68]. The number of attosecond pulses changes from odd to even when the CEP varies from integer π to half integer π (figure 2.21).

The experimental XUV harmonics are optimized for the short trajectories by phase matching, and the simulation only considers its contribution. Figure 2.21 also shows that the attosecond pulses are positively chirped¹⁶, which can be understood from the classical trajectories in section 2.4.1. Knowing the properties of the attosecond pulses, such as number of attosecond pulses and phase information, helps us to analyze the asymmetric photoemission under an additional weak IR field (see Paper IV and Chapter 4).

¹⁵This highest harmonic is much lower than the case in section 2.4.4

¹⁶This can be seen from the increasing oscillation period within a single attosecond pulse

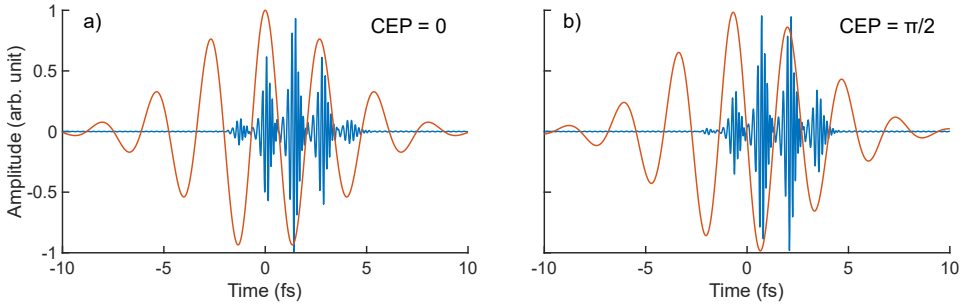


Figure 2.21: Attosecond pulses (blue) generated from the corresponding IR field (red). (a) The CEP is 0, and there is an odd number of attosecond pulses. (b) The CEP is $\pi/2$, the number of attosecond pulses is even.

2.5 Intense XUV Source — Free Electron Laser

Free electron lasers (FELs) can provide several orders of magnitude more intense radiation than any other X-ray source. This opens new possibilities for studying nonlinear effects in the X-ray regime. The intensity is sufficient to perform not only sequential multiphoton ionization, but also direct multiphoton ionization [72]. The adjustable intensity of an FEL can also provide the intermediate regime, where the difference between sequential or direct double photoionization can be studied [73].

Free electron lasers require a high-quality bunched electron beam generated from linear accelerators (figure 2.22). The initial electrons originate from a UV laser induced-photoelectric effect. The electrons are then accelerated in radio-frequency (RF) cavities. The electron bunches are further shaped with compressors and accelerators. The final electron bunch duration is from tens of femtosecond to around a hundred femtosecond, while its kinetic energy is usually from sub GeV to more than ten GeV [74–76].

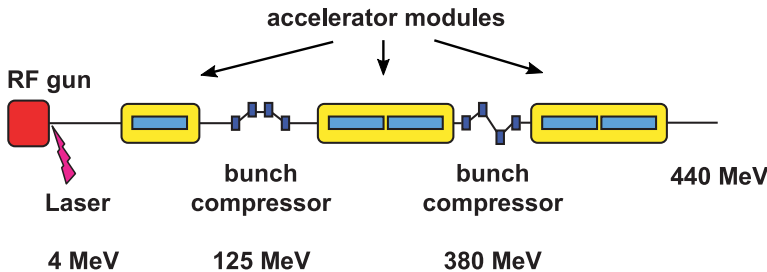


Figure 2.22: The linear accelerator of the Free-Electron LASer (FLASH) in Hamburg provides the electron source for generating FEL. The schematic drawing presents the accelerator parts for the first GW power emission in 2006 (adapted from [74]).

As the electron beam passes through a series of magnets with alternating polar-

ity, which is called undulator, the electrons will be deflected by the Lorentz force and emit radiation. These GeV electrons are sent into the undulator magnets with a relativistic velocity equal to:

$$v = \beta c = \sqrt{1 - \frac{1}{\gamma^2}} c \approx \left(1 - \frac{1}{2\gamma^2}\right) c \quad (2.48)$$

γ is the Lorentz factor, such that the electron energy is $E = \gamma mc^2$. β is the ratio between the electron velocity and the speed of light. Consider the observer in the rest frame, the wavelength of the emission from the accelerated electrons is the difference between the wavefront position of the previous emission (λ_u/β) and the current source position (λ_u). This can be approximated as:

$$\lambda = \frac{\lambda_u}{\beta} - \lambda_u \approx \frac{\lambda_u}{2\gamma^2} \quad (2.49)$$

By the contraction of the Lorentz factor γ , the emission wavelength can easily reach the X-ray regime. For instance, if we have an undulator with 27 mm period and 1 GeV electron beam, the emission wavelength is at 7 nm. By analyzing the electron motion in an undulator with the Lorentz force equation, the overall effect without considering off-axis emission is [77]:

$$\lambda = \frac{\lambda_u}{2\gamma^2} \left(1 + \frac{K^2}{2}\right), \quad K = \frac{eB_0\lambda_u}{2\pi m_e c} = 93.36 B_0[T]\lambda_u[m], \quad (2.50)$$

where K is called deflection parameter, with a value around 1 to 3. B_0 is the peak of the magnetic field from the undulators, which often provide around 1 Tesla.

The conventional way to generate FEL pulses is to operate the FEL in the self-amplified spontaneous emission (SASE) mode. It starts from an incoherent emission, and the electron bunch forms micro-bunches due to the interaction between the electrons and the emitted light. The traveling speed is slightly off between electrons and the emitted light, leading to dephasing. As the different electrons inside a bunch experience different light fields, some will be decelerated or accelerated. This leads to the microbunching and consequently coherent emission (figure 2.23). As the electrons propagate through the undulators, the emission intensity grows exponentially until it saturates when the microbunches are completely formed [78]. There are other techniques for improving the FEL quality in different aspects. For example, a seeded FEL has been demonstrated and applied to experiments [79]. More details about the different FEL light sources can be found in the following papers [76, 80–82].

The FEL facility FLASH in Hamburg was the first vacuum ultraviolet (VUV) to soft X-ray FEL. Its construction started in 1994 and the laser was commissioned in the mid of 2005 [74, 80, 83]. The FLASH facility now contains two SASE beamlines in parallel, FLASH1 and FLASH2. The schematic layout is shown in figure 2.24. The electron bunches are generated with a photoinjector induced by a laser, and then get accelerated by a superconducting linear accelerator shown as the yellow

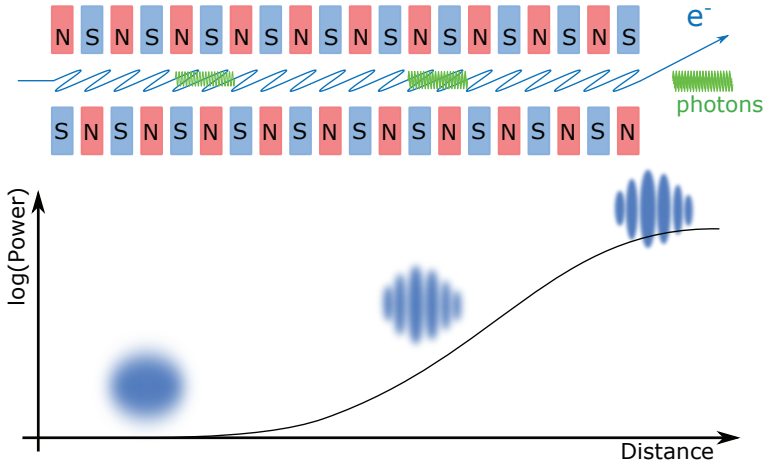


Figure 2.23: Schematic of a Free Electron Laser (FEL) operated in the self-amplified spontaneous emission (SASE) mode.

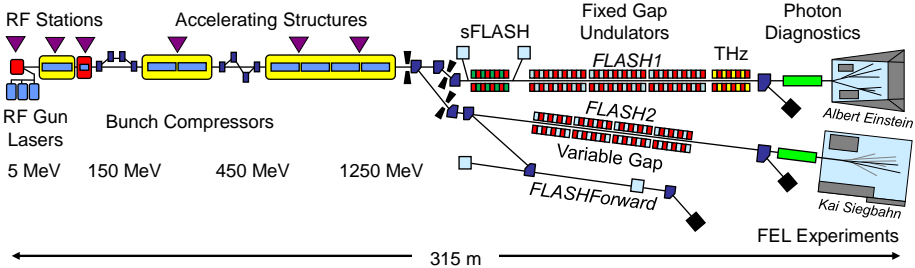


Figure 2.24: Schematic layout of the FLASH facility. Two SASE beamlines, FLASH1 and FLASH2 are in operation. The third one, FLASHForward used for plasma acceleration, is under construction [84].

part in figure 2.24. The electron bunches are split into different beamlines for lasing. The electron bunches are finally dumped and the laser photons are sent to the hatches for experiments. The electron bunches have a repetition rate of 10 Hz and each bunch contains hundreds of mini-bunches¹⁷, adjustable down to a single mini-bunch per bunch. The time interval between mini-bunches is restricted by the maximum length of the mini-bunch trains, which is 800 μs . The photon pulse duration can be adjusted by changing the electron mini-bunch's properties and the

¹⁷Don't get confused between micro- and mini-bunch, micro-bunch is the spiky structure per laser shot.

Table 2.2: The FLASH1 and FLASH2 parameters [84]

Parameters	FLASH1	FLASH2
Electron bunch charge (nC)	0.1-1.2	0.02-1
Electron bunches per second (typical/max)	300/5000	300/5000
Photon energy (eV)	24 - 295	14 - 310
Photon wavelength (nm)	51 - 4.2	90 - 4
Photon pulse duration (fs)	<30 - 200	10 - 200
Single photon pulse energy (average μJ)	1 - 500	1 - 1000
Photons per pulse	10^{11} - 10^{14}	10^{11} - 10^{14}

setting of the undulators. The adjustable range and the specification of FLASH1 and FLASH2 are summarized in table 2.2.

In the FLASH hall, there are five experimental stations (BL1, BL2, BL3, PG1, PG2) for different applications. Here, in this thesis work, we used the BL1 beamline with a multipurpose CAMP chamber including an electron-ion coincidence spectrometer. This beam line was designed to have a tight focusing with Kirkpatrick-Baez (KB) mirrors, and the focal spot was $6 \times 8 \mu\text{m}$ (design value: $3 \times 4 \mu\text{m}$). This provides an extremely small interaction volume and creates a high intensity. The FEL pulse energy can be reduced with a gas attenuation chamber and filters (Al, Si, Zr, Nb), and the combination of gas and filters reduces the intensity enough to reproduce single photon ionization conditions. In Paper V, the intensity of FEL was set to achieve sequential multiphoton ionization on the d-shell of methyl iodide (CH_3I). Further detail of this experiment will be discussed in Chapter 4.

3D ELECTRON-ION MOMENTUM IMAGING SPECTROMETER

For the past decades, the development of electron-ion momentum imaging spectrometers has resulted in kinematically complete measurements in atomic and molecular systems. This has led to a deeper insight into many ultrafast processes in atomic and molecular systems, such as Auger electron emission [85], interatomic Coulombic decay [86, 87], etc. Electron-ion spectrometers have almost become standard equipment in the field of atomic and molecular science. To construct such equipment, one of the most challenging aspects is to collect all the charged particles, especially the energetic and lightweight electrons. Therefore, we will focus on the electron momentum measurement in the following discussion.

There are several ways to collect emitted electrons, regardless of their initial momentum direction (measurement of the full solid angle). A widely applied technique called Velocity Map Imaging (VMI) uses a strong electric field to accelerate electrons towards a two-dimensional detector [88]. This method prevents energetic electrons from escaping detection, but it gives low momentum resolution in the direction perpendicular to the detector plane due to a small spread in electron time of flight. Even in a 2D momentum measurement, a 3D momentum image can be retrieved by using the inverse Abel transform [89]¹.

To have a direct 3D momentum imaging, it is necessary to reduce the electric field for obtaining the temporal information of the electrons. A pure electric field method with electrostatic lenses makes it possible to reconstruct 3D electron momentum vectors [90–93]. Electrostatic lenses are suitable for collecting charged particles with low kinetic energy (e.g. sub eV \sim few eV), but is not efficient for the collection of charged particles with a higher kinetic energy at a good resolution. To obtain a compromise solution between resolution and detection range, spectrometers can take advantage of the interaction of a moving charged particle

¹assuming cylindrical symmetry in a direction along the detector plane

with a uniform magnetic field. Thanks to the additional magnetic field, electrons are accelerated perpendicular to the magnetic field direction, leading to a cyclotron motion that keeps electrons within detection range. This technique is applied to the spectrometer built in this thesis, and it will be further discussed below.

Reaction Microscope

From a historical perspective, the 3D electron-ion momentum imaging technique that employs a magnetic field originates from Recoil Ion Momentum Spectroscopy (RIMS). It was developed in the late 1980s [94–96] for the study of collision-induced ionization of electron/ion beams. The momentum resolution was limited by the thermal motion of the gas target, and the first improvement on the ion momentum measurement was achieved by reducing the gas target temperature with supersonic expansion, leading to a well-known technique called Cold Target Recoil Ion Momentum Spectroscopy (COLTRIMS) [97]. Finally, by combining a magnetic field with a weak electric field, the full solid angle (4π steradians) electron collection efficiency of high kinetic energy electrons was no longer a limitation [98]. This high-resolution 4π detection of recoil electron-ion spectrometer is also called REaction MIcroscope (REMI) — the “bubble chamber of atomic physics” [99–101]. Since the mid-90’s, many names and acronyms have been used to designate 4π collection spectrometers depending on the research group of development or the design. In this thesis, a REMI spectrometer at the FLASH facility [102, 103] was utilized to study the molecular dissociation dynamics of methyl iodide (Paper V).

For the major part of the thesis, I have developed a 3D electron-ion momentum imaging system based on the “Coincidences entre Ions et Electrons Localisés” (CIEL) setup [104–106], which is mainly used for detecting photoelectrons with a high repetition rate laser system (Paper III, Paper IV). The following section starts by introducing the working principle of the spectrometer. The motion of the charged particles in the electric and magnetic field is then derived. This is followed by the spectrometer design of the new developed CIEL and the REMI spectrometer. Then, we present calibration work and the resolution study carried out for measurements (Paper III), and show the advantage of employing the coincidence measurement that is commonly used with this type of spectrometer.

3.1 Working Principle

The concept of 3D electron-ion momentum imaging for both ion and electrons can be illustrated as in figure 3.1. With a uniform, constant electric field and magnetic field along the z -axis, the gas phase targets (atoms, molecules, clusters, etc...) sent in as a gas jet along the x -axis are photoionized by the laser light source propagating along the y -axis. The light source can be an IR laser, XUV attosecond pulses or an intense X-ray FEL as stated in Chapter 2. After the targets are photoionized, both positively charged ions and negatively charged electrons experience the Lorentz force, and move towards the ion and electron detectors,

respectively. These detectors record the charged particle impact position (x,y) and the time of flight (t) , which can be used to calculate the initial momentum of the charged particles (p_x, p_y, p_z) .

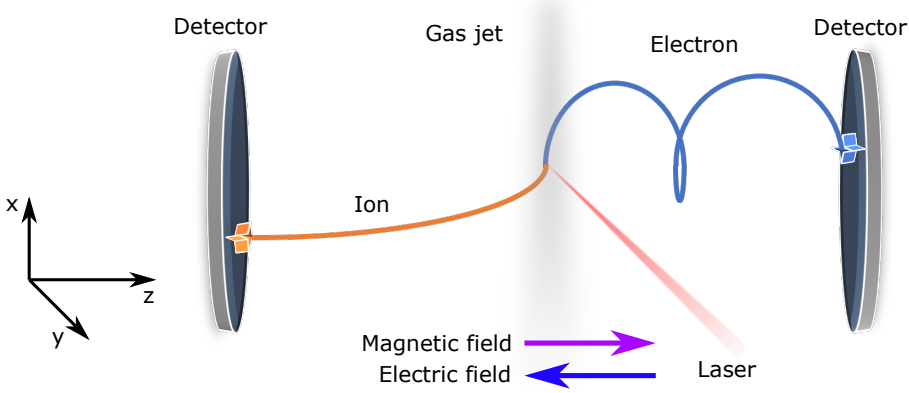


Figure 3.1: Schematic drawing of the 3D momentum imaging spectrometer.

To reconstruct the initial momentum of the charged particles, we start by solving the Lorentz force equation:

$$\mathbf{F} = q(\mathbf{E} + \mathbf{v} \times \mathbf{B}), \quad (3.1)$$

where q represents the charge, and \mathbf{v} is the velocity of the charged particle. The n multiply charged ion carries the charge $q = ne$, and the electron carries the negative charge $q = -e$, where e is the elementary electric charge. In the following equations, we describe the electron moving in the positive z -direction. The ion equation is similar, but the z coordinate is changed to $-z$ and the charge e is replaced by ne .

Under collinear electric and magnetic field configurations ($\mathbf{E} = -E \hat{\mathbf{z}}$, $\mathbf{B} = B \hat{\mathbf{z}}$), the motion of electrons can be decomposed into two parts: longitudinal (\parallel) and transverse (\perp) components.

$$\begin{cases} \mathbf{F}_{\parallel} = eE\hat{\mathbf{z}} \\ \mathbf{F}_{\perp} = -e\mathbf{v}_{\perp} \times (B\hat{\mathbf{z}}) \end{cases} \quad (3.2)$$

Longitudinal Momentum

The longitudinal motion along the spectrometer axis depends exclusively on the electric field. In this thesis, there are two types of electric field configurations as shown in figure 3.2. The drifting time (t_1) in the extraction region (with a length d) can be calculated by the impulse, which is equivalent to the change in momentum.

$$\begin{aligned} eEt_1 = \Delta p &= p_{zf} - p_z = \sqrt{2m(p_z^2/2m + eEd)} - p_z \\ t_1 &= \frac{\sqrt{p_z^2 + 2meEd} - p_z}{eE} \end{aligned} \quad (3.3)$$

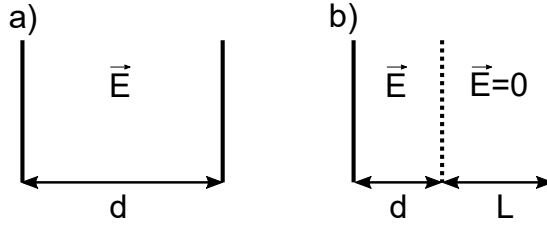


Figure 3.2: Two types of electric fields used for spectrometers: (a) a single electric field with a length d , (b) a single electric field with an additional length L field-free region.

Here, p_{zf} is the final momentum after acceleration, m is the electron mass². In the case of a single electric field spectrometer as the one shown in figure 3.2 (a), t_1 is the total drift time. The initial momentum p_z can be retrieved from Newton's equations:

$$p_z = \frac{md}{t_1} - \frac{qE}{2}t_1 \quad (3.4)$$

In the second case, as illustrated in figure 3.2 (b), by adding an additional drift tube of length L , we need to define the field-free drifting time t_2 as:

$$t_2 = \frac{L}{p_{zf}/m} = \frac{mL}{\sqrt{p_z^2 + 2meEd}}$$

The total time t is the sum of t_1 and t_2 , giving equation 3.5:

$$t = t_1 + t_2 = \frac{\sqrt{p_z^2 + 2meEd} - p_z}{eE} + \frac{mL}{\sqrt{p_z^2 + 2meEd}} \quad (3.5)$$

The momentum p_z for the spectrometer configuration shown in figure 3.2 (b) can be retrieved by solving the equation 3.5. After some rearrangement, it can be expressed as a cubic polynomial equation:

$$\begin{cases} a_3 p_z^3 + a_2 p_z^2 + a_1 p_z + a_0 = 0 \\ \begin{cases} a_3 = 2eEt \\ a_2 = (eEt)^2 - 2meE(d+L) \\ a_1 = 4me^2 E^2 dt \\ a_0 = me^2 E^2 [2eEdt^2 - m(2d+L)^2] \end{cases} \end{cases} \quad (3.6)$$

which can be solved analytically [107].

Equation 3.4 and 3.6 can be approximated to a linear equation if the energy accumulated from the extraction field is larger than the initial energy of the photoelectrons ($qEd \gg E_k$, or $2meEd \gg p_z^2$):

$$p_z = eE(t_0 - t), \quad \text{where } t_0 = \sqrt{\frac{2md}{eE}} \left(\frac{2d+L}{2d} \right) \quad (3.7)$$

²In this chapter, we use m instead of m_e for a simpler expression.

Here, t_0 stands for the nominal time of flight for the electrons with zero longitudinal momentum. This equation is also valid for the single electric field configuration (equation 3.4) by simply setting the drift tube length to zero, i.e. $L = 0$.

Transverse Momentum

From equation 3.2, it follows that the transverse motion of a charged particle depends exclusively on the magnetic field. The two-dimensional motion follows a circular path, since the force is always perpendicular to the direction of the motion. The centripetal force can be expressed as:

$$\mathbf{F}_\perp = m\vec{\omega} \times \mathbf{v}_\perp = -m\mathbf{v}_\perp \times \vec{\omega} = -e\mathbf{v}_\perp \times (B\hat{\mathbf{z}}), \quad (3.8)$$

where \mathbf{v}_\perp is the transverse velocity of the charged particle. We also introduce the cyclotron frequency $|\vec{\omega}| \equiv \omega$ and cyclotron period T_c :

$$\omega = \frac{eB}{m} \quad (3.9)$$

$$T_c = \frac{2\pi}{\omega} = \frac{2\pi m}{eB}, \quad (3.10)$$

which is the time for a charged particle to complete a full revolution. The cyclotron period thus scales linearly with the particle's mass. Considering now a typical magnetic field of ~ 10 Gauss, the cyclotron period is 36 ns for electrons, but is 262 μs for a singly charged helium ion. The typical electron time of flight is several tens of nanosecond, which is at the same order magnitude of the cyclotron period. However, the ion time of flight is usually around a few μs , such that the transverse motion of ions is safely approximated to be a linear motion without considering the magnetic field.

$$\begin{cases} p_{ix} = m_i(x_i - x_{i0})/t \\ p_{iy} = m_i(y_i - y_{i0})/t \end{cases} \quad (3.11)$$

Here, x_{i0} , y_{i0} denote the origin of the interaction point in the x-y plane. Equation 3.11 shows that the transverse momentum of ions is linearly proportional to the position displacement from the interaction point.

For the electrons, the radius of the circular motion can be derived from equation 3.8:

$$R = \frac{|\mathbf{p}_\perp|}{eB} \quad (3.12)$$

Equation 3.12 shows that the radius R is inversely proportional to the strength of the magnetic field. With a given size of the detector, the radius of the electron trajectories can thus be confined by applying a proper magnetic field. In principle, one just needs to increase the magnetic field to detect electrons with higher kinetic energies.

The initial transverse momentum of electrons can be calculated by analyzing their transverse motion from trigonometric considerations in appendix A. With a

magnetic field directed along the +z direction, the initial transverse momentum of each electron can be calculated from:

$$\begin{cases} p_x = \frac{m\omega}{2}(x \cot \frac{\omega t}{2} + y) \\ p_y = \frac{m\omega}{2}(y \cot \frac{\omega t}{2} - x) \end{cases} \quad (3.13)$$

If the magnetic field points along the -z direction, a similar equation set can be easily derived by replacing ω with $-\omega$ in equation 3.13.

Magnetic Nodes

The electron rotates with a cyclotron period T_c , which is independent of the electron's kinetic energy. This means that all electrons return to the origin periodically in the transverse plane, giving rise to so called "magnetic nodes". It is therefore impossible to determine the kinetic energy of an electron measured at a time of flight coinciding with one of these nodes. Thus, even if all electrons can be detected in full solid angle measurement, magnetic nodes can still lead to ambiguity in the measurement of their kinetic energies.

In traditional 3D momentum imaging in a magnetic field, magnetic nodes are usually unavoidable if a good resolution for the lower kinetic energy of electrons is required. In 2005, an optimization design principle of 3D momentum imaging spectrometers was proposed for 4π resolvable momentum retrieval [106]. The design includes a complete electron detection range without any non-retrievable points, i.e. no magnetic nodes. The way to avoid these magnetic nodes is by positioning all the electrons within the time interval of adjacent magnetic nodes, which corresponds to one cyclotron period.

To make this possible, the spread of the electron time of flight should be smaller than the cyclotron period. The maximum time spread of the detected photoelectrons depends on the strength of the longitudinal momentum, which is defined by the emission angle and the kinetic energy of the photoelectrons. For the highest kinetic energy electron, it reaches the detector in the shortest time when it initially moves straight forward ($+\hat{z}$) to the detector (t_{for}). If the electron initially moves to the opposite side ($-\hat{z}$), it takes the longest time to reach the detector (t_{back}). The time difference between these two ($\Delta t = t_{back} - t_{for}$) is called the "turn around" time, and corresponds to the maximum time spread in the time-of-flight spectra. The turn around time can be calculated as the additional momentum needed to turn the backward electron to move forward.

$$\Delta t = t_{back} - t_{for} = \frac{\Delta p}{F} = \frac{2 \cdot \sqrt{2mE_k}}{eE} < T_c \quad (3.14)$$

Here, Δt must be smaller than one cyclotron period T_c . The other requirement is that all the electrons' time of flight should be located between the magnetic nodes, and the nominal time t_0 is usually set to the middle of two magnetic nodes to maximize the time spread.

$$t_0 = \frac{2k-1}{2}T_c = \frac{(2k-1)\pi m}{eB}, \quad k = 1, 2, \dots \quad (3.15)$$

These two criteria are used for the CIEL design that was realized in this thesis. In Paper III, the impact of the magnetic nodes on retrieving momenta has been investigated for conventional spectrometers and the current CIEL at Lund University.

3.2 Experimental Setup

In this thesis work, two spectrometers (CIEL and REMI) were used. The CIEL was employed to detect photoelectrons and ions, while the REMI at the FLASH facility was used to study ion-ion mass and momentum correlation without applying a magnetic field. In the following, we describe the complete 3D momentum imaging system in three different parts: the spectrometer design, the magnetic coils and the detection. We focus on the CIEL design as a reference, and compare it to the REMI design whenever there is a difference.

3.2.1 Spectrometer Design

The 3D electron-ion momentum imaging spectrometer CIEL has two configurations: an electron side with a drift tube and an ion side without a drift tube. The structure is presented in figure 3.3(a). The electron side is a single-E-field Wiley-McLaren spectrometer design with the length of the field-free region L that is twice the length of the extraction distance d (i.e. $L = 2d$) [108]. This condition leads to a compensation of the interaction volume extension along the spectrometer axis, such that the resolution of the longitudinal momentum is only limited by the the E-field homogeneity and the resolution of the detectors.

With a given detector size (80 mm in diameter), the spectrometer dimension can be calculated by two criteria (equation 3.14 and equation 3.15). After these two criteria have been applied, there are still two free parameters to be determined. One is the ratio between the turn around time and cyclotron period ($f = \Delta t/T_c$), also called the “filling factor”. The other is between which two magnetic nodes the electrons are placed. For the accuracy and practical reasons, by setting the turn around time to 70 % of the cyclotron period and positioning all the electrons between the 1st and the 2nd nodes, the dimension of the CIEL spectrometer is defined: 95 mm for the extraction region and a 190-mm field-free region on the electron side.

On the ion side, the extraction length is set to 85 mm without any field free region. There are two advantages of a single extraction field design. With the same extraction length, the ions with four times higher kinetic energy can be detected with 4π collection without the Wiley-McLaren drift tube. The other advantage of the single field design is that the ion time of flight is decreased for high repetition rate experiments.

The REMI spectrometer in figure 3.3 (b) is a multipurpose spectrometer with a 200-mm single-field design for both the electron and ion sides. The center electrodes are designed in a conical shape to collect the scattered photons with a pnCCD

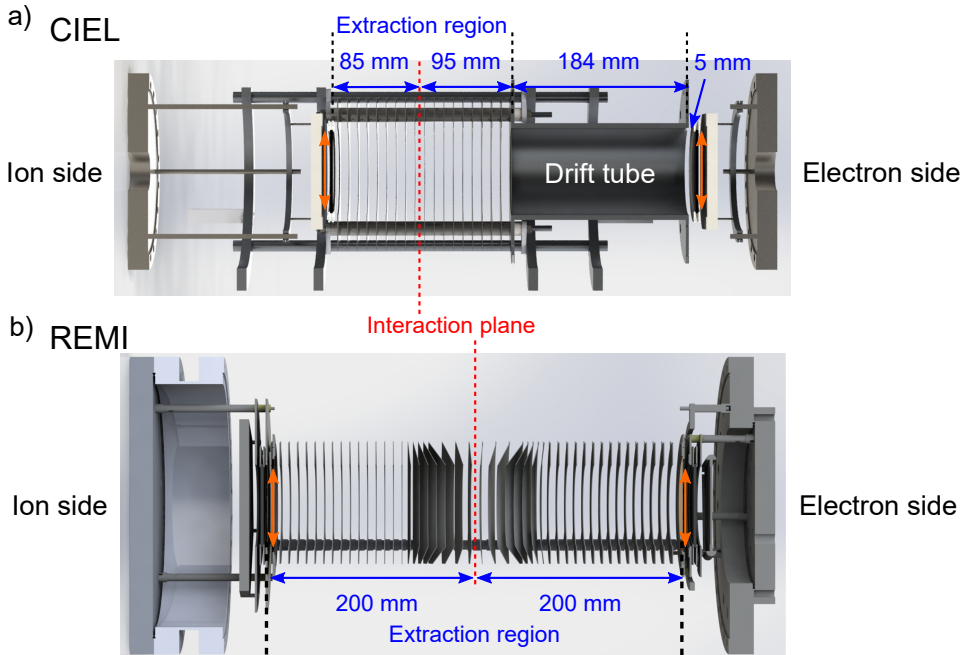


Figure 3.3: CAD drawings of two spectrometers cross-sectional view. The diameter of all the detectors marked with orange arrows are 80 mm. (a) The CIEL spectrometer in Lund: the length of the extraction region of the electron side is 95 mm, and the length of the drift tube is 184 mm. The length of the ion side is 85 mm with a single extraction region. (b) The REMI spectrometer in FLASH BL1 with a symmetric 200-mm extraction region for both electron and ion sides.

camera after the spectrometer [102, 103]. As discussed in Paper V, the ion-ion coincidence measurement uses only the ion side of the spectrometer.

3.2.2 Magnetic Coils

A controlled, homogeneous magnetic field is crucial for measuring electron momenta in our experiments. The most common way to prepare a uniform magnetic field for 3D momentum imaging spectrometers is by using a Helmholtz coil consisting of 2 identical coils separated by the radius R , which is usually large (e.g. 1.6 meters in diameter in reference [102]) and sometimes requires an additional cooling system to prevent Joule overheating.

In order to increase the volume of the uniform magnetic field without constructing large coils, several solutions have been proposed [109, 110]. These solutions mainly consist of two major coils with a few minor coils to extend the magnetic field volume. One of the most well-known solution is the Merritt 4-coil configuration, which contains four square coils of identical dimensions, but with a different

number of turns for major and minor coils (26 vs 11) [111]. The benefit of the square coils is that it becomes easier to prepare the frame of coils in different sizes. However, the shape of the uniform magnetic volume is not similar as our spectrometer shape, such that the Merritt 4-coil is not the optimum solution for having the most compact coils.

As shown in figure 3.3 (a), the geometry of our spectrometer is a long cylinder shape with an aspect ratio (length/width) of around 4. An efficient way to create a uniform magnetic field volume with a similar aspect ratio is the Lugansky 4-coil solution with coils of two different sizes [112]. The set of coils consists of two major coils in the middle with two minor coils on the sides (see figure 3.4 (a)). These four coils have the same number of turns and the same currents, such that they can be driven by a single power supply connected in series, which is practical for operation. For this reason, the Lugansky 4-coil configuration was used for the developed CIEL. From numerical simulations, we found that the uniformity of the magnetic field should be within a 0.5 % variation to ensure the accuracy of measured electron momenta. Within the magnetic field uniformity ($\pm 0.5\%$) in figure 3.4 (b), the dimension of the coils are chosen to be 80 cm and 63 cm for major and minor coils, which can be implemented with bicycle rims (36, 29 inches) without having to make circular frames, and between the coils there is an almost identical spacing (30.4, 30.7, 30.4 cm). Thus, the entire spectrometer system with magnetic coils remains compact.

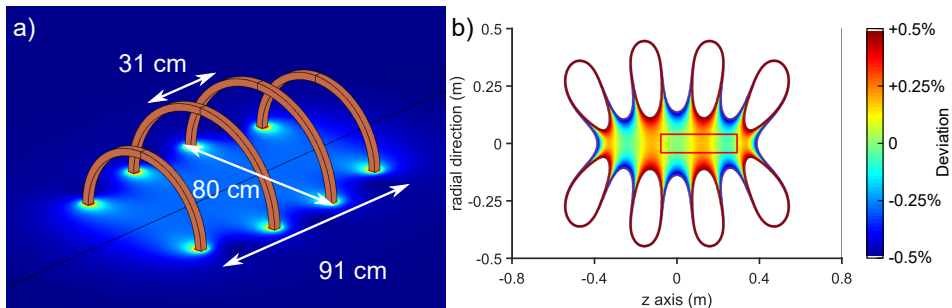


Figure 3.4: The Lugansky 4-coil solution creates a uniform magnetic field (a) simulated with COMSOL. The brown colored parts are the coils, and the cut plane shows the magnetic field generated by them. (b) The 2D plot of the cut plane shows a colored region for a $\pm 0.5\%$ magnetic field variation. The red rectangular block represents the active volume of the spectrometer.

The discussion above only concerns the main magnetic field along the z axis. Two other axes of the magnetic field also need to be compensated when the main magnetic field is not strong enough to neglect the earth/environmental magnetic field. We constructed two pairs of the rectangular shaped Helmholtz coils as the compensating coils. Two pairs of coils are installed along the x and y axes (same definition as figure 3.1) on the same aluminum frame that supports the main Lugansky coils. Due to a space constraint, we chose to create the compensating B

fields on the x-axis with two rectangular coils (y: 58 cm, z: 80 cm shown in figure 3.5 (a) separated by 30 cm), and the compensating field on the y-axis with two other rectangular coils (x: 76 cm, z: 80 cm shown in figure 3.5 (b) separated by 28 cm). We verified with simulations that the inhomogeneity introduced by these coils (4~8%) was smaller than that of the main magnetic field (e.g. $< 0.5\% \times 5 \text{ Gauss} = 25 \text{ milli Gauss}$) within the active volume of the spectrometer.

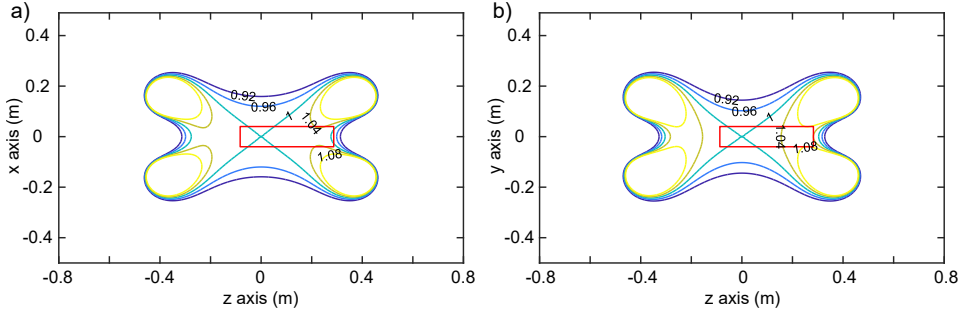


Figure 3.5: Magnetic field cut of the rectangular Helmholtz compensating coils on (a) the z-x plane and (b) the z-y plane. The color contours are 4 % per step, and the red rectangle shows the active volume of the spectrometer.

As equation 3.12 indicates, the maximum radius of the electron helical motion depends on the magnetic field, which is about 9.8 Gauss for confining 30 eV electrons within our detector radius ($R = 40 \text{ mm}$). The target magnetic field can be provided by the compact magnetic coils operating at a lower current than conventional (large) Helmholtz coils, reducing the power consumption and heat dissipation in the coils.

In our condition, each coil has 100 turns of enameled copper wire ($N = 100$). The current (I) is applied in the wire with resistance R and cross section a . The power consumption P can be directly written from Ohm's law:

$$P = I^2 R \quad (3.16)$$

The resistance R can be written as $\rho NL/a$, where ρ is the resistivity (e.g. copper: $1.68 \times 10^{-8} \Omega \cdot m$), L is the circumference of a single turn of wire.

The generated magnetic field is proportional to the current of coil (i.e. $B \propto NI \equiv \text{constant } \mathcal{C}$). Hence, the power consumption with a target magnetic field can be calculated as:

$$P = \frac{\mathcal{C}^2}{N^2} \rho \frac{NL}{a} = \mathcal{C}^2 \rho \frac{L}{A}, \quad (3.17)$$

where A is the total cross section area of the coil ($A = Na$). It shows that the power consumption is independent of the number of turns N , but inversely proportional to the total cross section area A . The diameter of the copper wire is 2 mm for

our coils, providing enough total cross section for low power consumption on each coil³.

The coils are operated without any thermal management. The temperature variation ΔT can be calculated by measuring the change in resistance [113].

$$\Delta T = \frac{1}{\alpha} \left(\frac{R}{R_{ref}} - 1 \right) \quad (3.18)$$

Here, R/R_{ref} is the relative change in resistance, which can be deduced from the variation of current during an experiment, and α is the temperature coefficient (copper: 4.041×10^{-3}). During the experiments, our coil resistance increased by 0.5 % indicating that the temperature was raised by $\sim 1.2^\circ\text{C}$. In summary, the total cross section area around 3.1 cm^2 with 80-cm diameter major coils in the Lugansky 4-coil design can confine 30 eV electrons within an 80 mm diameter detector with about 1°C of temperature rise. We therefore conclude that compact magnetic coils can be operated with only a slight increase of coil temperature without any active cooling.

3.2.3 Detection

The position sensitive detector (PSD) is composed of a delay line detector (DLD) anode and a two-stage microchannel plate (MCP) (see figure 3.6). When a charged particle hits the two-stage MCP⁴, an avalanche amplification occurs, leading to a collection of $10^7 \sim 10^8$ electrons (electron cloud). After amplification by the MCP, the electron cloud hits the DLD consisting of two orthogonal layers of copper wires inducing electronic signal. Since the two layers are orthogonal, each layer determines the corresponding coordinate.

The time of flight is usually determined by the MCP, and the position (x,y) is defined by the DLD. On the right side of figure 3.6, the time difference between signals 1 and 2 shows the position value on each axis. The calculation of position and time can be written in simple equations.

$$\begin{cases} X = x1 - x2 + O_x \\ Y = y1 - y2 + O_y \\ T_{sumx} = (x1 + x2 + \text{offset}_x) \\ T_{sumy} = (y1 + y2 + \text{offset}_y) \end{cases} \quad (3.19)$$

The last terms in each equation represent the offsets coming from different wire lengths. The last two equations are supposed to give the time of flight. All of these offsets can be compensated in the data acquisition software (Cobold PC). In the current spectrometer, 2-layer DLDs on both sides of the spectrometer are installed for coincidence detection with a low event rate per laser shot. As the experiments

³For example, in Paper III, the power dissipation of each coil was less than 10 W. The major coil and minor coil consumed 8.4 W and 6.6 W, respectively.

⁴The two-stage MCP is mounted in a chevron configuration.

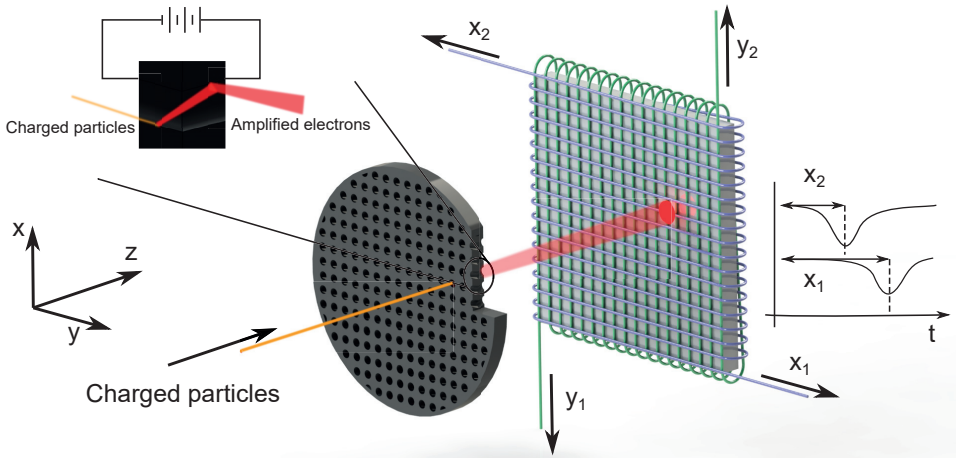


Figure 3.6: Schematic drawing showing the function of the delay line detector and microchannel plate (MCP). The two-stack MCP (black) amplifies the incoming charged particle signal and converts it into a bunch of electrons (the drawing shows the positive charge ions on the MCP). The amplified electrons hit the delay line detector and are recorded by two layers of helical wires.

need to record multiple electrons per laser shot (e.g. two-electron correlation), the DLD detector may encounter some lost events. For example, if two electron clouds hit the detector within a short period of time and with a small space separation (e.g. < 10 ns, and a few mm), the second hit will not be detected. This “dead time” period can be improved by using a Hexanode detector with three layers of copper wires [114].

Note that each layer actually has a pair of wires, which is shown in figure 3.6 as a single helical line. There are two wires used as a reference wire and a signal wire. They are biased with around 30 V potential difference in order to ensure the electron signals propagate on the signal wire. The function of the reference wire is used to remove the background signal for improving the signal-to-noise ratio.

Data Acquisition Electronics

After the light matter interaction, an ionization event can be detected by the PSDs. The electronic signals should then be processed, stored and analyzed by a computer. Figure 3.7 presents an overview for the electronics circuit for coincidence measurement.

The electronic signals arising from the PSDs are first amplified and then converted. Two different strategies are utilized in our setup with the RoentDek electronic devices. On the ion side, the ATR19 module uses a Constant Fraction Discriminator (CFD), which generates a digital pulse (NIM standard, -0.8V) at the arrival of an analog signal with almost no jitter. This method is more precise

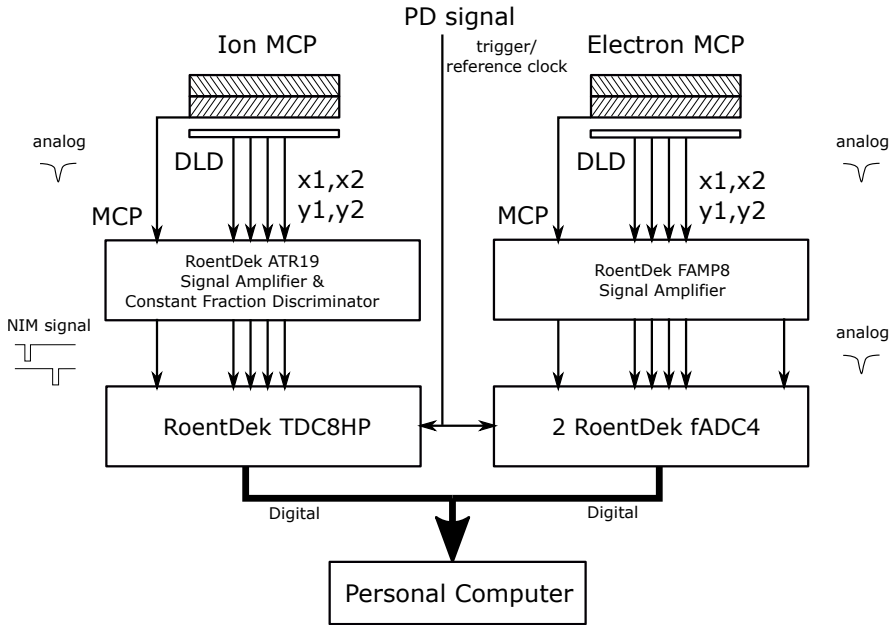


Figure 3.7: Schematic circuits for coincidence measurement with both electron and ion detectors. The PD signal is the laser photodiode signal triggering the acquisition. Both DLD detectors deliver analog signals to the signal amplifiers, after which they are processed in two different ways.

than using a linear discriminator due to the different intensity of the signal pulses. The NIM pulses are sent into a Time to Digital Converter (TDC), which converts the arrival time of the pulses into a timing sequence using a reference clock given by a photodiode signal from the laser. This method is a conventional way to process enormous amounts of electrical signals with hardware first, after which the processed signals are stored as a timing sequence for the purpose of smaller data sizes. During the experiment on the REMI spectrometer at the FLASH facility, the TDC method was also used to collect ion fragments.

On the electron side, after the signals are amplified by the amplifier (FAMP8), the fast Analog to Digital Converter (fADC4) directly converts the amplified analog signals to digital ones, and the timing of the pulses is then processed by a computer. The advantage of this approach is that it can analyze more advanced multi-hit conditions, and the fastADC techniques are more preferable for post-processing electronic signals if needed. However, the downside of this technique is the higher demand on computational power.

3.3 Commissioning of the CIEL

The first step before using the momentum imaging spectrometer is calibration. Especially, the electron side should be calibrated to demonstrate the capability of recording 4π angle-resolved photoelectron spectra. In Paper III, we performed an atomic photoionization experiment for electron calibration, and at the same time, the mass resolution on the ion side of the spectrometer was measured. Here, the electron calibration is firstly discussed, and the ion mass resolution is presented in the end of this section.

In the following, we show two parts of the electron momentum calibration. The first one discusses the calibration of the offset in time of flight and position of the photoelectron upon detection, important for the correct momentum retrieval. The second calibration procedure determines the photoelectron energy resolution, to be used as a reference in future measurements. The calibration of the electron resolution requires different kinetic energy electrons, which can be obtained from a tunable light source such as synchrotron radiation. An alternative way, without scanning the incoming photon wavelength, is to create a photoelectron spectrum with multiple narrow spectral lines, and one of the methods is to apply Above Threshold Ionization (ATI) [115] with an intense IR laser commonly found in ultrafast laser labs.

ATI is a multiphoton process, i.e. several photons are absorbed simultaneously to overcome the ionization potential of the target. It can generate a higher kinetic energy of electrons with the spacing defined by the incoming photon energy as shown in figure 3.8 (a). In this experiment, we chose the heavy noble gas krypton

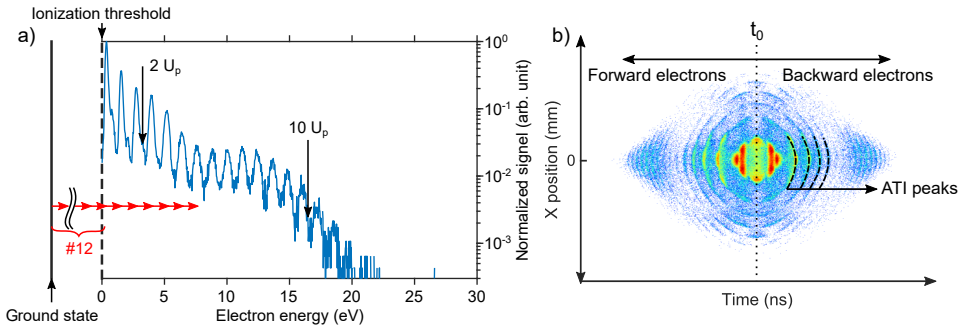


Figure 3.8: An illustration about above threshold ionization with a photoelectron spectrum generated from krypton atoms. (a) One-dimensional photoelectron peaks correspond to the generation from at least 12 IR photons. Two cut-offs ($2 U_p$ and $10 U_p$) equal to 3.2 eV and 16.2 eV, respectively. (b) Two-dimensional photoelectron distribution shows the forward and backward electrons with nominal time of flight t_0 . The ATI peaks are marked as the black arc lines.

with the ionization potential of 14.0 eV as our target. The intense IR laser was not the OPCPA laser system, but instead the Yb:KGW (ytterbium-doped potassium

gadolinium tungstate) fiber laser system (PHAROS, Light Conversion). Due to the longer pulse duration (about 170 fs FWHM), the pulses are spectrally narrow. The central wavelength of the PHAROS laser is at 1030 nm (≈ 1.2 eV), signifying that the ATI needs at least 12 photons to create photoelectrons. The two arrows $2 U_p$ and $10 U_p$ represent the direct ionization cut-off and rescattering cut-off [116]. U_p is the ponderomotive energy, which is the cycle-averaged quiver energy of the electron in the oscillating electric field.

The PHAROS laser has a tunable pulse duration from 170 fs to 500 fs. The repetition rate of the laser system can be varied from 1 kHz to 600 kHz, and the maximum pulse energy output is up to 6 mJ at 1 kHz. We chose the 170 fs transform-limited pulses with 0.2 mJ pulse energy, and we focused the laser beam into the spectrometer with a lens of 40 cm focal length. The beam diameter was focused from 3.8 mm to 135 μm , giving an intensity up to 1.6×10^{13} W/cm² corresponding to a 1.6 eV ponderomotive energy ($U_p = e^2 E^2 / 4m_e \omega_0^2$). The laser system was operated at 20 kHz to maximize the event rates in the coincidence regime⁵.

The raw data of photoelectrons acquired from the CIEL spectrometer is shown in figure 3.8 (b). The 2D spectrum contains one spatial distribution and the time-of-flight information. The structure of the rings corresponds to the ATI peaks with different kinetic energies. The time-of-flight spacing becomes narrower as it moves away from the nominal time of flight t_0 . This can be understood from equation 3.4, in which the approximated longitudinal momentum is linearly proportional to the difference in time of flight with respect to t_0 .

For the electrons close to the nominal time of flight t_0 , the ATI arc lines were not continuous (see figure 3.8 (b)). This has been studied in strong field ionization by many groups [117–120]. These structure lines are related to the ion potential, so the pattern varies with the different species of target atoms [117]. In this part, we only used the ATI spectrum for offset calibration and for studying the resolution, but our clearly angle-resolved photoelectron spectra could be useful for further investigation on the ATI angular distribution.

3.3.1 Offset Calibration

Time Offset Calibration

The time offset can be determined by using the periodicity of the magnetic nodes in the time of flight. The time calibration can be done by applying a low extraction field and a high magnetic field without generating high kinetic energy electrons. The low extraction field causes the photoelectrons to spread out along the time-of-flight axis, so that they cross the magnetic nodes forming a wiggle spectrum, as presented in figure 3.9.

With the time between magnetic nodes obtained, one can then use the cyclotron period equation 3.10 to retrieve the effective magnetic field in the spectrometer. Since the magnetic nodes are equally spaced, the origin of the time of flight can be

⁵The electron and ion count rate was around 4 kHz and 1.5 kHz, respectively.

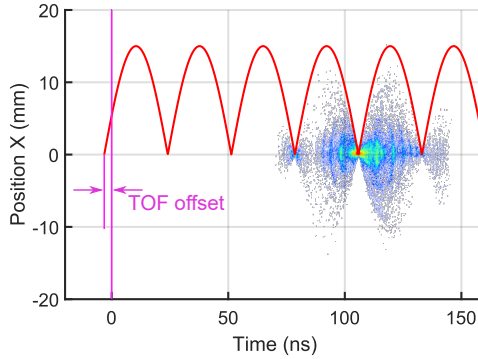


Figure 3.9: The wobble spectrum shows the magnetic nodes created by applying 3.3 V/cm electric field and a high magnetic field on the spectrometer. The temporal spacing of the magnetic nodes is around 27.3 ns corresponding to a magnetic field of 13.1 Gauss. The red line shows a trajectory with a 15-mm revolving radius (appendix equation B.3), and the time of flight (TOF) offset is found to be -3.2 ns

traced back with a multiple integer of the nodes spacing. The example in figure 3.9 shows that the actual origin of the time of flight was at -3.2 ns. This value was applied to correct the time offset from the measurement, giving the absolute timing for the momentum reconstruction.

Position Offset Calibration

Parasitic magnetic fields can affect the electron spectra, and the main contribution usually comes from the earth magnetic field⁶ Although the applied magnetic field is several times larger than the earth magnetic field, the electron spectra will still be affected. In Nordic countries, the magnetic field mainly points downward (0.473 Gauss over the total magnetic field of 0.503 Gauss [121]), which is perpendicular to the spectrometer axis. In our detector coordinate, the earth magnetic field caused a shift in the electron spectra toward the negative x direction with a tilt as shown in figure 3.10 (a). The blue line shows the symmetry line for the photoelectron spectrum to trace the tilting, and the tilted spectra are also observed when there is a misalignment of the applied magnetic field with respect to the electric field (i.e. $\mathbf{B} \nparallel \mathbf{E}$).

The tilt and offset of a photoelectron spectrum can be corrected by applying compensating magnetic fields until the center of the electron pattern ceases to change as a function of the time of flight. Figure 3.10 (b) presents a corrected photoelectron spectrum with an additional magnetic field along the positive x-direction. After performing another magnetic field compensation on the y-axis, the

⁶This takes into account that non-magnetic materials were used for the spectrometer itself and no magnetic objects were placed in the vicinity of the device.

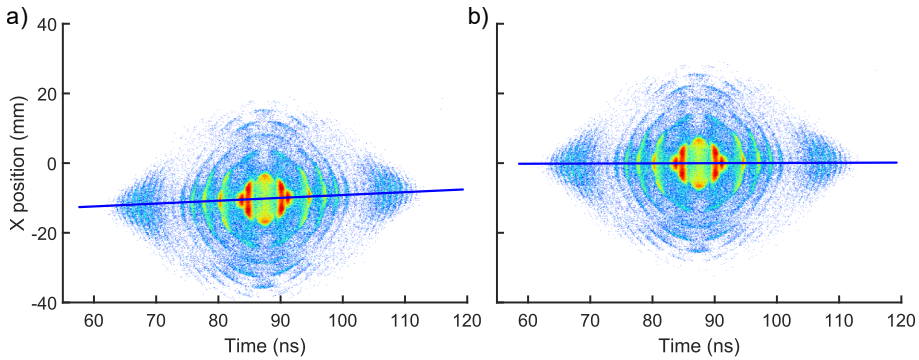


Figure 3.10: Spatial-temporal electron spectra. The electric field is set to 5.5 V/cm, and the applied magnetic field is estimated around 6.2 Gauss for both spectra. The blue lines are the symmetry line demonstrating the tilt. (a) The electron spectrum with a transverse magnetic offset, and (b) the optimized electron spectrum.

corrected photoelectron spectrum was ready to be used to retrieve the momentum in the data analysis.

Magnetic Field Calibration

After compensating the environmental magnetic field on the transverse direction, the final step was to calibrate the magnetic field along the spectrometer axis. This was done by measuring the temporal spacing between the adjacent magnetic nodes using different driving currents on the coils. In figure 3.11, the residual magnetic field along the spectrometer axis was about 0.3 Gauss in the opposite direction of the applied magnetic field, and the increasing slope of the magnetic field was found around 3.4 Gauss per ampere.

The resolution of the spectrometer is determined by its design with the response function of the detector, the homogeneity of the electric and magnetic field, and the size of the interaction volume. We first analyzed the ultimate spectral resolution which was based only on the geometry of the spectrometer and the detector response time. We then included the inhomogeneity of fields with a numerical simulation. Finally, we discussed the interaction volume effects. For the ions, since they are insensitive to the magnetic field, the resolution is only estimated with a pure electric field condition.

3.3.2 Resolution Calibration

Ultimate Resolution

In order to estimate the ultimate resolution of the spectrometer, we perform simulations that only consider the spectrometer design and the detector response under ideal conditions. It is assumed that the charged particles are generated from a single

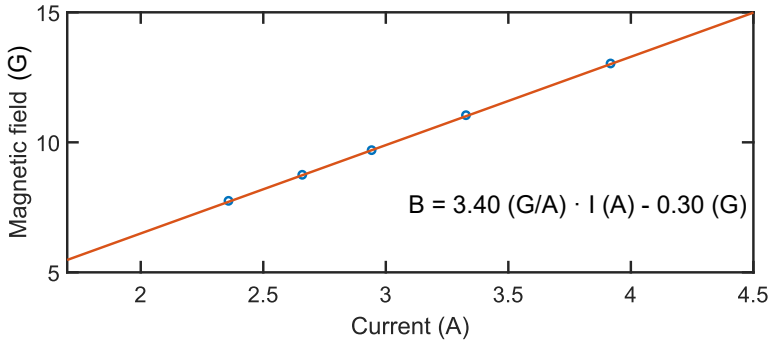


Figure 3.11: The magnetic field calibration is a fitted linear function with several measured points. Each measured point was converted from a cyclotron period to the magnetic field. The offset of the magnetic field follows from linear fitting.

source point under perfectly uniform electric and magnetic fields. The resolution of the kinetic energy ΔE_k is estimated from the deviation of the measured position σ_x, σ_y and time σ_t . If all the deviations can be described as normal distributions, the kinetic energy resolution can be written as:

$$\Delta E_k = \sqrt{\left(\frac{\partial E_k}{\partial x}\right)^2 \sigma_x^2 + \left(\frac{\partial E_k}{\partial y}\right)^2 \sigma_y^2 + \left(\frac{\partial E_k}{\partial t}\right)^2 \sigma_t^2} \quad (3.20)$$

With some algebra (see Appendix B), we obtain the final analytical expression of the electron kinetic energy resolution:

$$\Delta E_k = \sqrt{\frac{m^2 \omega^4}{16} \left(r^2 \csc^2\left(\frac{\omega t}{2}\right)\right) \sigma_x^2 + \left(\frac{p_z}{m} \frac{\partial p_z}{\partial t} - \frac{m \omega^3}{8} r^2 \left(\cot\left(\frac{\omega t}{2}\right) \csc^2\left(\frac{\omega t}{2}\right)\right)\right)^2 \sigma_t^2}, \quad (3.21)$$

where the spatial resolution in the x- and y-direction are the same (i.e. $\sigma_x = \sigma_y$). If the electron moves along the spectrometer axis toward the detector without any transverse momentum, the first term with σ_x^2 is 0. This means that the electron energy resolution is defined only by the temporal response of the detector. Second, when $\omega t/2$ is equal to odd numbers of multiple half π , the cosecant term is 1, and the cotangent is 0. In this condition, the energy resolution depends only on the spatial resolution of the detector σ_x . When $\omega t/2$ equals multiple π (even numbers of multiple half π), where the magnetic nodes are located, the value of the cosecant is infinite. This means that the energy is not resolvable, and this not an ideal condition for the spectrometer.

By inserting the upper bound of the detector resolution parameters into equation 3.21, the lower limit of the spectrometer resolution can be defined. According to the detector supplier RoentDek, the DLD spatial and temporal resolutions are <0.1 mm and <0.2 ns, leading to about few % relative resolution ($\Delta E_k/E_k$) as the

ultimate resolution of our spectrometer⁷. The resolution of the CIEL spectrometer is angular and energy-dependent, and the two dimensional analysis is shown with comparison to the REMI from the FLASH facility in Paper III.

Fields Homogeneity

Homogeneous and constant electric and magnetic fields are essential to retrieve the momenta of charged particles correctly. The inhomogeneities of both fields may hinder our spectrometer from reaching the ultimate resolution. The fields homogeneity effects in our 3D momentum imaging system were verified with the simulation package SIMION [122]. Under the radial symmetric and collinear fields assumption, the possible contributions affecting the resolution can be narrowed down to the effect of electrodes⁸ close to the interaction region and the inhomogeneities of the magnetic field.

We compared our design to perfect conditions, which correspond to identical electrodes and a uniform magnetic field. Both conditions were tested under the assumption of an ideal point source, which emitted in an isotropic 4π distribution with discrete kinetic energy spacing. The generated electrons were guided by electric and magnetic fields to the detector with a helical motion. As they hit the detector, the position and the time of arrival were recorded. The difference between the two conditions was very minor, and the relative resolution under both conditions was consistently below 0.5 %, i.e. $\Delta E_k/E_k < 0.5\%$. Moreover, the better relative resolution ($\Delta E_k/E_k < 0.2\%$) was obtained under a slightly higher kinetic energy ($> 10\%$ of maximum detection kinetic energy). In summary, the inhomogeneities of the electric and magnetic fields were almost negligible with respect to the ultimate resolution given by the detector specification ($\Delta E_k/E_k \approx \text{few}\%$).

Interaction Volume

Equally important as the design of the momentum imaging spectrometer is the gas jet that delivers the target gas. In our current spectrometer system, we started from an effusive gas jet for a higher target density. The dimensions of the interaction volume are determined by the width of the effusive jet (horizontal direction) and the laser beam waist (vertical direction), see figure 3.12 (a).

In the experiment with an XUV light source, the interaction volume follows the confocal parameter of the light source, which is twice of the Rayleigh range ($b = 2z_0 = 2 \times \pi W_0^2/\lambda$). In the IR multiphoton ionization experiments, the effect is strongly nonlinear. This corresponds to an effective shrinking of the interaction volume. Thus, the spectrometer resolution study described in Paper III was carried out with a multiphoton ionization experiment.

The experimental configuration was the same as in figure 3.1. The interaction volume along the laser propagation direction was still not negligible with multipho-

⁷It depends on the applied fields and the electron emission angle.

⁸Two pairs of electrodes (74 mm, and 82 mm in diameter) close to the interaction region are smaller than others (90 mm in diameter).

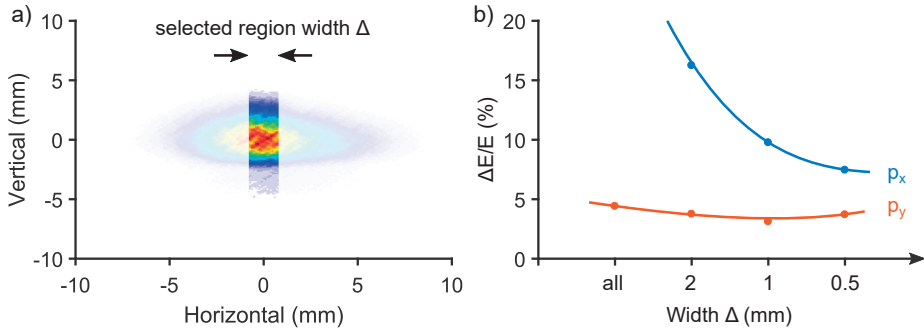


Figure 3.12: Relation between the selected region width and the relative resolution. (a) The selected region width Δ shows on the ion detector image. (b) The relative resolution plot for p_x and p_y .

ton ionization experiment. The elongation of the interaction volume was parallel to the detector plane, which degraded the resolution in the transverse direction⁹. Since the gas target used in this multiphoton experiment was krypton, the heavy atomic ions were insensitive to the recoil force from the electrons¹⁰. In addition, the experiment was measured in coincidence, so the photoelectrons were filtered by selecting the corresponding detected krypton ions. With this method, an effectively shorter interaction volume were reached by applying a narrower width of the selected region on the recorded ion signal. Figure 3.12 (a) shows the ion image recorded by the ion detector with a selected region as the coincidence filter. The relative resolution in figure 3.12 (b) demonstrates that the momentum component p_x was strongly affected by the effective interaction volume, but that the other momentum component p_y was almost independent of the filter width. Since the interaction volume became longer along the y-axis, and according to the momentum retrieval equation 3.13, the broadening happened only on the p_x component.

In Paper III, we estimated the elongation of the interaction volume to be around 1.5 mm, which is similar to the typical XUV experiments with a molecular beam system. To further reduce the interaction volume of the XUV experiments, a molecular beam with an orifice or slit could be used.

3.3.3 Ions Resolution

This thesis work involves photoionization of atomic systems. Under this special condition, the 3D momentum imaging system acted as a mass spectrometer.

Since ions are much heavier than electrons, the magnetic field can be neglected. The charged ions were accelerated with an electric field towards the detector, and the longitudinal motion of the ions was resolved temporally with the PSD, which

⁹The Wiley-McLaren spectrometer design can correct only the volume extension perpendicular to the detector (longitudinal direction).

¹⁰The transverse motion of krypton ions were rather stationary.

had a relatively small impact on the resolution. The theoretical analysis was similar to that in section 3.1, and we assumed that the resolution was determined by the initial kinetic energy of the ions.

With the initial kinetic energy E_{ki} , the ions had a time spread in the time-of-flight, denoted as Δt_i . The relation between mass resolution, time spread, and the time of flight was derived from the time-of-flight equation (i.e. $m_i/\Delta m_i = TOF/(2\Delta t_i)$). Then, the mass resolution can be expressed as follows [108]:

$$\frac{m_i}{\Delta m_i} = \frac{1}{2} \sqrt{\frac{qEd}{E_{ki}}}, \quad (3.22)$$

where q is the ion's charge and d is the length of the extraction region. In mass spectroscopy, the mass resolution is usually defined as a resolving power ($m/\Delta m$), also called the maximum resolvable mass.

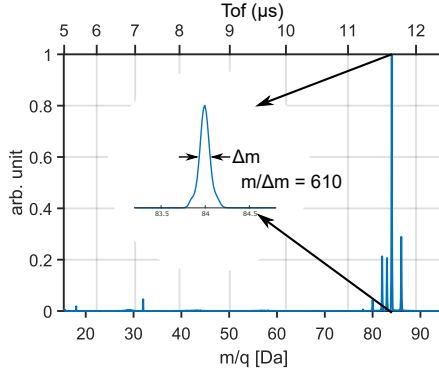


Figure 3.13: A time-of-flight spectrum showing the krypton isotopes and its mass resolution with some residual elements. The insertion shows the resolving power 610 at mass 84 Da. The CIEL spectrometer was operated under 11.1 V/cm extraction field and 8.66 Gauss magnetic field. The residual elements were oxygen (atomic mass = 32) and water (atomic mass = 18) left inside the chamber.

Figure 3.13 depicts the experimental result from ionizing krypton is plotted against two axes, i.e. time-of-flight and mass-to-charge ratio. The mass-to-charge ratio (m/q) is proportional to the square of the time-of-flight, giving rise to an unequal spacing for the time of flight when the spectrum shows an equal spacing of m/q . For the most abundant krypton isotopes with an atomic mass of 84 (Da)¹¹, the experimental resolving power was 610 (Δm in FWHM), which corresponds to $\Delta m_i = 0.138$ (Da).

The initial kinetic energy of the ions originates from the thermal motion, which puts the limit for the ion resolution. The thermal noise can be reduced by using a molecular beam. If the gas target is cold enough, the recoil momentum from

¹¹atomic mass units

the emitted electron can be seen [101]. Some other factors may also disturb the ion resolution, such as the power supplies for electric field. If there is about 0.2% fluctuation in the power supply, the resolution linewidth will broaden at the same level as we measured in the experiment.

APPLICATIONS

This chapter provides an overview of the measurements performed on atomic and molecular systems. The first experiment in Paper [IV](#) was done with XUV Attosecond Pulse Trains (APTs) in conjunction with few-cycle IR pulses. We observed an asymmetric angular photoelectron distribution which was controlled by changing the CEP of the IR field. The few-cycle IR pulses were used both as a probe of the photoionization process but also to generate the APTs. The asymmetry phenomenon could be explained as the result of interference between electron wave packets generated by attosecond pulses. The second experiment in Paper [V](#) was performed with an intense XUV light source from the FLASH facility in Hamburg. We used this light source to multiply ionize the methyl iodide molecules, creating many localized holes and leading to the Coulomb explosion of the molecule. We developed a model to rationalize the Kinetic Energy Release (KER) upon dissociation. This allowed us to understand the complex interplay between photoionization, Auger decay and charge transfer dynamics.

4.1 Electron Wave Packet Interferometry

Interferometry is a general technique giving access to small changes. In optics, interferometry can resolve the structure or properties of the objects with a precision of about a fraction of the wavelength. For instance, optical interferometry is used to measure the length difference between two optical arms, such as the laser interferometer gravitational wave observatory (LIGO) for detecting small ripples in space-time [\[123\]](#). Another example in biology and medical applications is optical coherence tomography (OCT), which provides a non-invasive and non-destructive imaging technique for diagnostic.

A fundamental property of quantum mechanics is that particles (atoms, electrons) are also waves and therefore interfere with each other. Already in 1927, Germer and Davisson observed the wave property of electrons by bombarding elec-

trons on a solid target [124]. The wave properties of the electron provides another tool for investigating matter on the atomic scale.

Interference of electron wavepacket is at the cornerstone of attosecond science [125–128]. A first example is the process of high harmonic generation itself, where a fraction of the EWP in the continuum interferes with its bounded counterpart during recombination (see Chapter 2). A second example can be found during the ionization process by a train of attosecond pulses in the presence of a dressing IR field. The additional IR field manipulates the momentum and phase of the electron wave packets leading to an interesting interference structure [127]. In our case, as the number of attosecond pulses reduces to only two or three and as the IR is very weak (Paper IV), we found the interference pattern to behave differently, leading to asymmetric photoelectron angular distribution.

4.1.1 Theory

The interaction between an atom and a weak light field (i.e. an attosecond pulse) can be described with first order perturbation theory. The time dependent Schrödinger equation (TDSE) of the interaction is written as:

$$[\hat{T} + \hat{V}(r) + \hat{V}_I] |\Psi(t)\rangle = i\hbar \frac{\partial}{\partial t} |\Psi(t)\rangle, \quad (4.1)$$

where \hat{T} is the kinetic energy operator, \hat{V} is the atomic binding potential, and \hat{V}_I is the interaction term between the attosecond pulse and the atom. When the wavelength of the attosecond pulses is much longer than the atom size (i.e. $\lambda \gg 1\text{\AA}$), the interaction term can be approximated by the electric dipole $\hat{V}_I = ezE(t)$, assuming that the laser polarization direction is along the z-direction (i.e. $\mathbf{E} = E(t)\hat{z}$).

To solve approximately the TDSE, three assumptions are made:

- No depletion of the ground state
- Only the ground state is considered as a bound state.
- The electron in the continuum can be treated as a free particle without the influence of the atomic potential.

For most of the photoionization conditions, the first assumption is usually valid. The second assumption means there is no transition between bound states. When the electron is ionized by the XUV field, the last assumption is valid for photoelectrons with high kinetic energy.

Electrons in the Continuum

Before solving the TDSE, we first need to consider the solution for a free electron in the continuum with the presence of a dressing field. It is equivalent to effectively

ignore the atomic potential term $V(r)$ in equation 4.1:

$$[\hat{T} + \hat{V}_I] |\tilde{k}\rangle = i\hbar \frac{\partial}{\partial t} |\tilde{k}\rangle, \quad (4.2)$$

where $|\tilde{k}\rangle$ is called Volkov state. Equation 4.2 can be solved analytically. In a one-dimensional case, the equation can be written as:

$$\left[-\frac{\hbar^2}{2m} \frac{\partial^2}{\partial z^2} + ezE(t) \right] \psi_k(t, z) = i\hbar \frac{\partial}{\partial t} \psi_k(t, z) \quad (4.3)$$

A Volkov state can be written as a product of plane wave and time-dependent phase [129], as:

$$\psi_k(t, z) = \frac{1}{\sqrt{2\pi}} \exp \left[i \left(k + \frac{eA(t)}{\hbar} \right) z - i \frac{S(k, t)}{\hbar} \right], \quad (4.4)$$

where $A(t)$ is the vector potential:

$$A(t) = - \int_{-\infty}^t dt' E(t'), \quad (4.5)$$

and $S(k, t)$ is the phase accumulated during propagation in the vector potential $A(t)$:

$$S(k, t) = \frac{\hbar^2}{2m_e} \int_{-\infty}^t dt' \left[k + \frac{eA(t')}{\hbar} \right]^2 \quad (4.6)$$

Similar to the one-dimensional solution, a generalized three-dimensional Volkov state is:

$$\psi_k(t, \mathbf{r}) = \frac{1}{(2\pi)^{3/2}} \exp \left[i \left(\mathbf{k} + \frac{e\mathbf{A}(t)}{\hbar} \right) \cdot \mathbf{r} - i \frac{S(\mathbf{k}, t)}{\hbar} \right], \quad (4.7)$$

In bracket notation, this expression is:

$$|\tilde{k}\rangle = \left| \mathbf{k} + \frac{e\mathbf{A}(t)}{\hbar} \right\rangle \exp \left[-i \frac{S(\mathbf{k}, t)}{\hbar} \right], \quad (4.8)$$

Transition Amplitude in a Two-color Field

In a two-color field, the time-dependent electron wave function can be written as a superposition of states:

$$|\Psi(t)\rangle = |\tilde{i}\rangle + \int d^3\mathbf{k} c_{\mathbf{k}}(t) |\tilde{k}\rangle, \quad (4.9)$$

The ground state wave function can be written as $|\tilde{i}\rangle \approx |i\rangle \exp[iI_p t/\hbar]$ (due to the nondepleted ground state assumption), where $|i\rangle$ is the time-independent wave function. The interaction term V_I now includes two components V_{IR} and V_{XUV}

with a time delay τ , such that the overall interaction term in the length gauge is written as:

$$V_I = V_{IR} + V_{XUV} = e\mathbf{r} \cdot (\mathbf{E}_{IR}(t) + \mathbf{E}_{XUV}(t - \tau)) \quad (4.10)$$

Inserting equation 4.9 into the TDSE equation 4.1, including the Volkov state (equation 4.2) and the property of the ground state, we should solve:

$$i\hbar \int d^3\mathbf{k} \dot{c}_{\mathbf{k}}(t) |\tilde{k}\rangle = V_I(t) |\tilde{i}\rangle + V(r) \int d^3\mathbf{k} c_{\mathbf{k}}(t) |\tilde{k}\rangle \quad (4.11)$$

By projecting onto the Volkov state $\langle \tilde{k}'|$, the differential equation can be further simplified:

$$i\hbar \dot{c}_{\mathbf{k}}(t) = \langle \tilde{k}'| V_I(t) |\tilde{i}\rangle + \int d^3\mathbf{k} c_{\mathbf{k}}(t) \langle \tilde{k}'| V(r) |\tilde{k}\rangle \quad (4.12)$$

The left term related to continuum to continuum interaction is neglected¹. Only the XUV electric field can ionize the ground state atom to the continuum, and the remaining interaction term V_I is approximated to V_{XUV} . Thus, equation 4.12 can be integrated:

$$c_{\mathbf{k}}(t) = -\frac{i}{\hbar} \int_{-\infty}^t dt' \langle \tilde{k}(t')| e\mathbf{r} \cdot \mathbf{E}_{XUV}(t' - \tau) |\tilde{i}(t')\rangle \quad (4.13)$$

The transition amplitude $a(\mathbf{p}, \tau) = c_{\mathbf{k}}(\infty)$ can be expressed as:

$$a(\mathbf{p}, \tau) = -\frac{i}{\hbar} \int_{-\infty}^{\infty} dt \mathbf{d}_{\mathbf{p}_c} \mathbf{E}_{XUV}(t - \tau) \exp \left[\frac{i}{\hbar} I_p t - \frac{i}{\hbar} \int_t^{\infty} dt' \frac{\mathbf{p}_c^2(t')}{2m_e} \right], \quad (4.14)$$

where $\mathbf{p}_c = \mathbf{p} + e\mathbf{A} = \hbar\mathbf{k} + e\mathbf{A}$ is the canonical momentum, and $\mathbf{d}_{\mathbf{p}_c}$ is the dipole matrix element. In a hydrogen-like system, the dipole matrix element $\mathbf{d}_{\mathbf{p}_c}$ takes a simple form [56]:

$$\mathbf{d}_{\mathbf{p}_c}(t) = \left\langle \mathbf{k} + \frac{e\mathbf{A}(t')}{\hbar} \left| e\mathbf{r} \right| i \right\rangle \propto i \frac{\mathbf{p}_c(t)}{(\mathbf{p}_c^2(t)/2m_e + I_p)^3} \quad (4.15)$$

As the dressing IR field is weak (i.e $|\mathbf{p}| \gg |e\mathbf{A}|$), equation 4.14 can be reduced to:

$$a(\mathbf{p}, \tau) = -\frac{i}{\hbar} \int_{-\infty}^{\infty} dt \mathbf{d}_{\mathbf{p}} \mathbf{E}_{XUV}(t - \tau) \exp \left[\frac{i}{\hbar} \left(I_p + \frac{\mathbf{p}^2}{2m_e} \right) t - \frac{ie}{m_e \hbar} \int_t^{\infty} dt' \mathbf{p} \cdot \mathbf{A} \right], \quad (4.16)$$

which is the starting equation used in Paper IV.

¹This can be done because the non-depleted ground state is the dominant part of the electron wave function in equation 4.9.

Example: Single Photoionization and EWP interferences

To understand the photoionization dynamics with APTs, we first switch off the IR dressing field. The transition amplitude is reduced to:

$$a_{\mathbf{p}} = -\frac{i}{\hbar} \int_{-\infty}^{\infty} dt \mathbf{d}(\mathbf{p}) \cdot \mathbf{E}_{\mathbf{XUV}}(t) \exp \left[\frac{i}{\hbar} \left(\frac{\mathbf{p}^2}{2m_e} + I_p \right) t \right], \quad (4.17)$$

From equation 4.17, the angular distribution of the transition amplitude is proportional to the inner product of $\mathbf{d}(\mathbf{p})$ (and therefore \mathbf{p}) with the electric field $\mathbf{E}_{\mathbf{XUV}}$. The momentum distribution of photoelectrons ionized by a single 500-as pulse is shown in figure 4.1 (a).

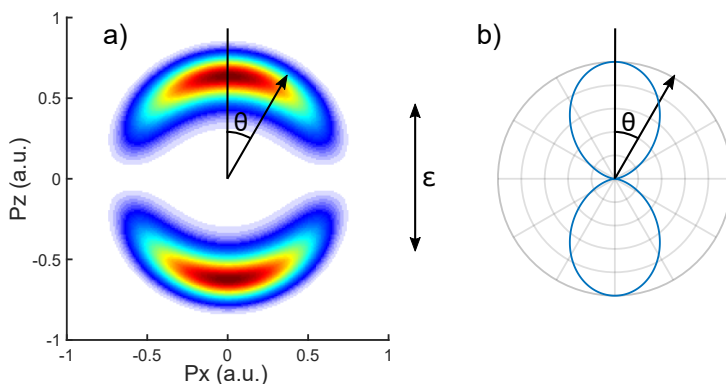


Figure 4.1: The $p_x - p_z$ plane of the 3D photoelectron distribution of helium. The helium atom is ionized by a single XUV pulse at 30 eV with 500 as pulse duration. The polarization axis of the XUV field is along the z-axis. (a) Momentum distribution. The momentum axes are labeled in atomic units (1 a.u. = 2.0×10^{-24} kg m/s). (b) Photoelectron intensity with momentum 0.63 a.u. shown in polar coordinates.

With a fixed polarization of the electric field along the z-axis, we define the θ angle as the polar angle between the momentum \mathbf{p} and the z-axis (electric field polarization). The inner product of \mathbf{p} and $\mathbf{E}_{\mathbf{XUV}}$ is proportional to $\cos\theta$. The transition probability is the square of the amplitude (i.e. $|a_{\mathbf{p}}|^2$), so the angular distribution of photoionization from s-orbital electrons is a $\cos^2\theta$ function, which reflects the distribution of a p-orbital (i.e. $1s \rightarrow \epsilon p$)². The distribution in intensity is presented in figure 4.1 (b) at a specific momentum (energy)³.

Electron wave packets interference is now illustrated in figure 4.2 for different characteristics of the attosecond light source. A short single attosecond pulse

²The angular distribution has rotational symmetry along the polarization axis z.

³The differential cross section, i.e. the photoelectron angular distribution, is $I(\theta) = \sigma[1 + \beta_2 P_2(\cos\theta)]/4\pi$, where β_2 is the anisotropy parameter and P_2 is the second-order Legendre polynomial [130]. For helium, β_2 is equal to -1.

generates a single EWP with a broad spectral distribution as in figure 4.2 (a). With more pulses, since each attosecond pulse produces a corresponding EWP, the generated EWPs interfere in the spectral domain. In figure 4.2 (b), we show the EWP interference due to two attosecond pulses with a sign flip (section 2.4.1). The photoemission spectrum has a periodic structure due to the spectral interference of the two pulses. If the temporal spacing between the attosecond pulses is double, the energy separation is divided by two, leading to the interference structure in figure 4.2 (c). Finally, figure 4.2 (d) presents the interference pattern due to three attosecond pulses. In addition to the main structure, similar to those in figure 4.2 (a), secondary maxima appear. This is similar to the Young's interference experiment with a three-slit condition.

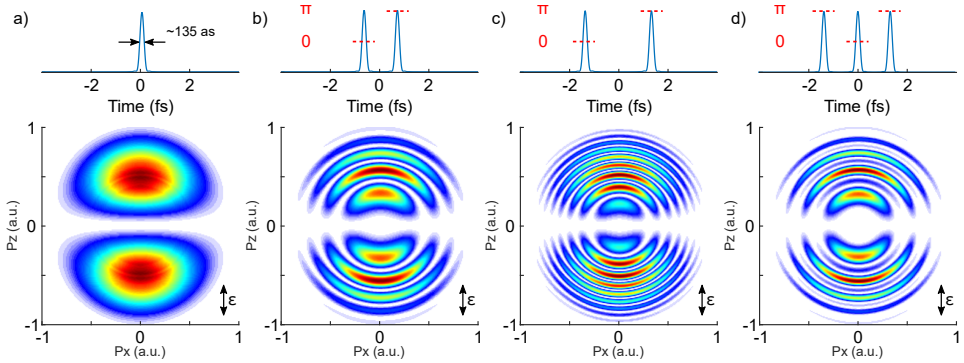


Figure 4.2: Electron wave packets interference. EWPs are generated from various number of XUV attosecond pulses with different phases. (a) single EWPs, (b) two EWPs with a π phase shift, (c) two EWPs with a π phase shift and a double temporal spacing, and (d) three EWPs with π phase shift between adjacent EWPs.

4.1.2 Method

The experimental setup used in Paper [IV](#) is shown in figure [4.3](#) (see also section [2.4.3](#)). The IR laser pulses were delivered from the high-repetition-rate few-cycle OPCPA laser system and focused into argon gas to produce an attosecond pulse train with only a few pulses (see section [2.4.5](#)). Both the IR and XUV fields with horizontal polarization were focused with a toroidal mirror into an helium gas jet in the 3D momentum imaging spectrometer. The intensity of IR field in the spectrometer was decreased from passing through the differential pumping hole, leading to a much reduced intensity ($< 10^{12}$ W/cm²) in the 3D momentum spectrometer. By changing the glass wedge insertion, we varied the CEP of the IR field, and recorded the corresponding photoelectron spectra.

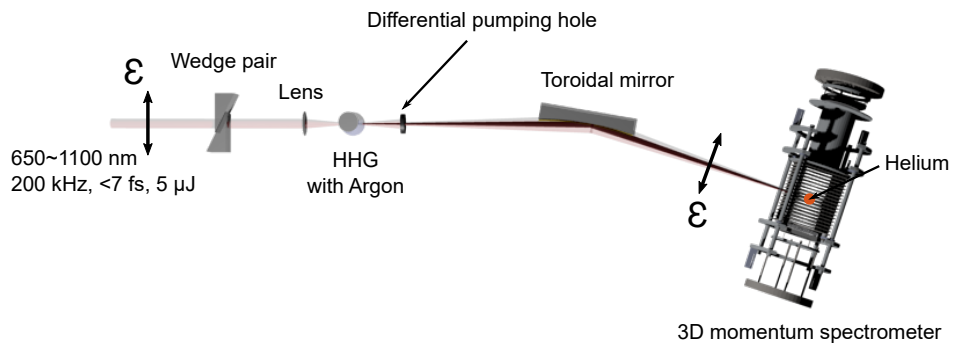


Figure 4.3: Illustration of the experimental setup for studying EWP interference. The ε shows the polarization direction.

4.1.3 Result

The CEP dependent photoelectron spectra are presented in figure [4.4](#)⁴. Asymmetric angular photoemission relative to the plane perpendicular to the polarization axis is observed when both XUV and IR interact with helium atoms. There are two special cases. When the CEP is equal to $(n+1/2)\pi$ where n is an integer, the photoemission pattern shifts towards positive or negative momentum p_z . In this case, an even number of EWPs is interfering. When the CEP of the IR field is an integer multiple of π , the photoemission process arises from the interference of an odd number of EWPs.

We show in Paper [IV](#) that the simulation can reproduce the experimental results. Analytical derivation is given to provide a deeper insight into the photoionization process. In the following parts, we present a summary of the simulation together with the mathematical expressions to discuss the origin of the asymmetry in photoemission.

⁴Data is presented as differential cross sections (see Appendix [C](#)).

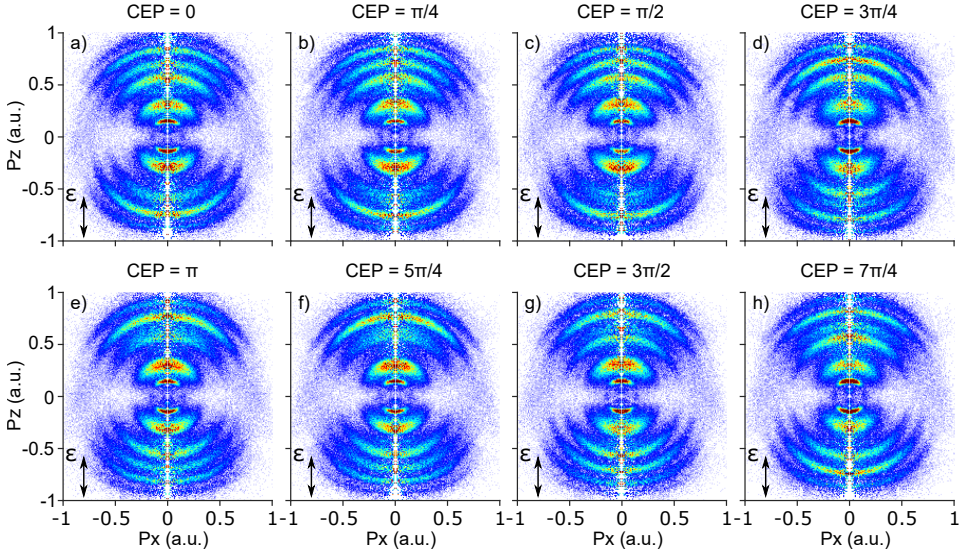


Figure 4.4: CEP dependent photoelectron spectra generated with XUV and IR fields. The images are integrated with azimuthal angles and replicated to produce a circular pattern.

Simulation: Two-color Photonization

The IR dressing field introduces an additional phase on each EWP depending on the delay between the EWP and the IR field. From equation 4.16, the additional phase difference between EWPs is the phase term:

$$\Delta\phi_{IR} \propto - \int_t^\infty dt' \mathbf{p} \cdot \mathbf{A}(t'). \quad (4.18)$$

The attosecond pulses are generated every half cycle of the IR field, a fraction of which is the dressing field. Due to the sign of the IR field changing every half cycle, consecutive attosecond pulses are opposite in sign, and the phase induced by the dressing field also changes sign.

We start with an ideal case where XUV pulses are transform-limited. In figure 4.5 (a), we present the effect of the phase modulation on the electron wave packet. When two electron wave packets, labeled as $m=0$ and 1 in figure 4.5 (a), spaced with half IR cycle are generated when the vector potential $\mathbf{A}(t)$ is zero, the acquired phase difference between the EWPs is maximized⁵.

The shaded area is positive, causing the second EWP ($m=1$) to have a negative phase shift with respect to the first EWP ($m=0$). The interference pattern shows a momentum shift in negative momentum direction ($-p_z$). The ionization probability

⁵This is equivalent to a quarter cycle shift with respect to the IR field defined as the sine function.

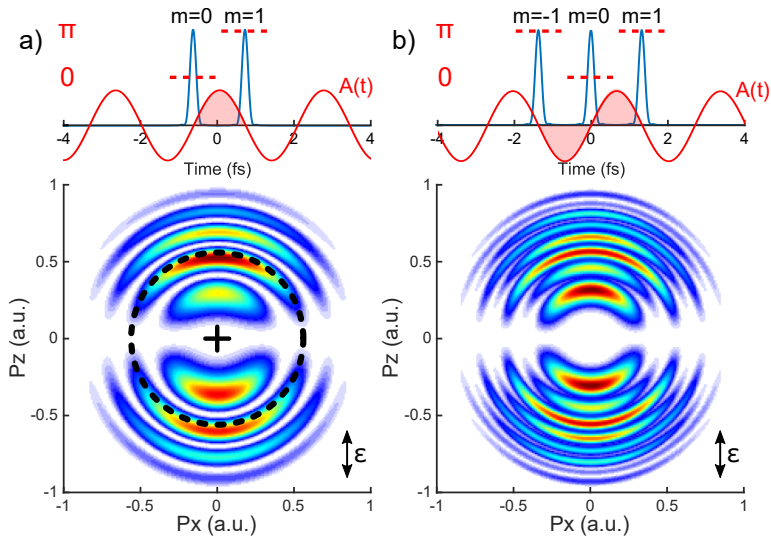


Figure 4.5: Electron wave packets interference with a weak IR field. The attosecond pulses/EWPs are labeled with index m , which is used as the sequence in time. For example, the $m=0$ EWP is earlier than the $m=1$ EWP. (a) Two EWPs have maximum phase difference from the IR field, and the black dashed circle shows the original position of the second ring counted from the center. (b) Three EWPs have maximum relative phase shifts between adjacent EWPs.

amplitude can be expressed as follows:

$$|a(\mathbf{p})|^2 \propto \sin^2 \left(\frac{\pi\Omega}{2\omega} + \eta_p \right), \quad (4.19)$$

where $\Omega = (I_p + \mathbf{p}^2/2m_e)/\hbar$, and ω is the laser frequency. The quantity η_p

$$\eta_p = \frac{e\mathbf{p} \cdot \mathbf{A}_0}{m_e \hbar \omega} \sin(\omega\tau) \quad (4.20)$$

is equal to the shift observed in the experiment. In our experimental condition, the IR field is weak, leading to a small value of η_p (i.e. $\eta_p < 1$).

In figure 4.5 (b), a third EWP ($m=-1$) is added. The $m=-1$ and $m=1$ EWPs are identical without any phase difference introduced by the IR. In this case sidebands appear, and there is no asymmetry.

In reality, XUV pulses are not transform-limited because each attosecond pulse in every half-cycle of the short driving pulse will be different due to the dipole phase. This in turn will offset the interference pattern as shown in figure 4.6⁶. In Paper IV, we show that the amplitude transition of three EWPs with the IR field

⁶The dipole phase is calculated with the same intensity 1.1×10^{14} W/cm² as in section 2.4.5.

can be simplified to:

$$|a(\mathbf{p})|^2 \propto 1 + 4r^2 \cos^2\left(\frac{\pi\Omega}{\omega}\right) - 4r \cos\left(\frac{\pi\Omega}{\omega}\right) \cos(s - 2\eta_p), \quad (4.21)$$

where r is the amplitude ratio between the outer two ($m=\pm 1$) and the central ($m=0$) attosecond pulses, and s is the spectral phase difference between them (see equation 2.46 in section 2.4.4). The last term in equation 4.21 is responsible for the appearance of the sidebands. If s is zero, the sign of the η_p , meaning the direction of \mathbf{p} , does not change the cosine value, and the momentum distribution is symmetric. On the other hand, if s is not equal to zero, it will lead to an enhancement or reduction of the sidebands depending on the sign of η_p , and consequently to an asymmetric distribution.

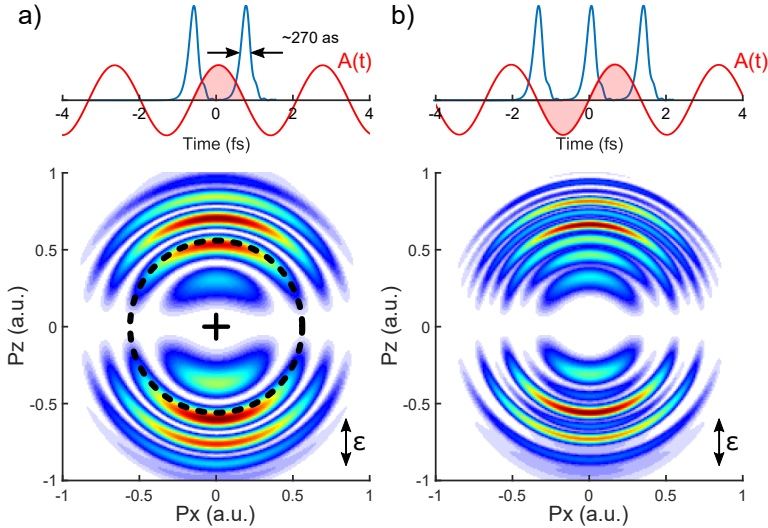


Figure 4.6: Electron wave packet interference generated from the attosecond pulses in presence of IR field. The phase of attosecond pulses are from the HHG simulation of 6 fs IR pulse. The intensity of the pulses are assumed to be the same ($r=1$). The pulse duration of attosecond pulses increases to 270 as, and each attosecond pulses/EWPs are labeled with m . (a) Two EWPs condition: The black dashed circle shows the original position of the second ring relative to the center. (b) Three EWPs condition. Side bands appear, which are more pronounced on the top.

In two EWPs case, the photoelectron distribution in figure 4.6 (a) is similar to the transform-limited attosecond pulse condition. The difference occurs when there are three EWPs. The photoelectron distribution difference between positive p_z and negative p_z can be clearly seen in figure 4.6 (b). The asymmetric pattern is, as expected from equation 4.21, from the small offset introduced by s .

Analogy: Slit Experiment

The interference between two or three EWPs in t-E (time vs energy) domain can be also understood with a slit experiment in x-k (space vs reciprocal space) domain. If we do not consider the dipole matrix element contribution in equation 4.16, the amplitude transition is close to a Fourier transform function with an energy offset (I_p) and the phase modulation from IR. The EWP additional phase from IR causes a temporal phase, which is equivalent to a spectral shift in energy domain. In the slit experiment, the spacing between slit is similar to the temporal spacing of the EWPs. The additional phase can be due to a phase plate on one of the slit, leading to a shift of the interference pattern.

Discussion: Spectral Interferometry

RABBIT⁷ is usually performed with a relatively long IR field from a conventional Ti:Sapphire laser system, which leads to a train of several attosecond pulses. The difference between this condition and our case can be understood in the spectral domain as illustrated in figure 4.7.

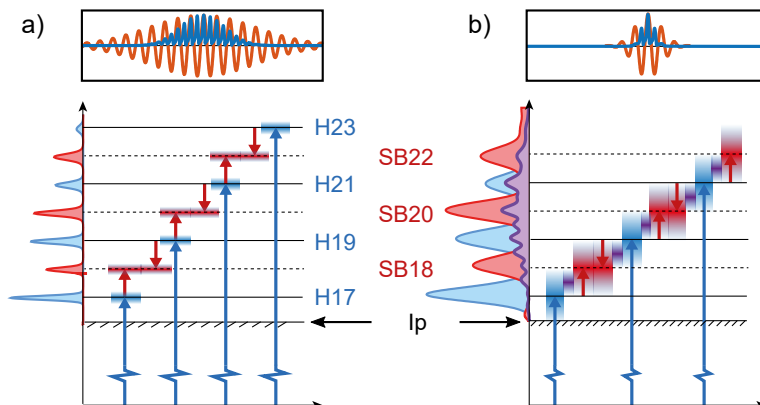


Figure 4.7: The photoionization of helium with XUV harmonics (blue) with an additional IR dressing field (red) are illustrated in the energy domain. (a) The harmonics are generated with a 25 fs IR pulse, and (b) with a 6 fs IR pulse. I_p is the helium ionization potential. HXX represents the harmonic XX^{th} , and the SBY stands for the side band YY^{th} .

The 25 fs IR pulse generates multiple attosecond pulses with the narrow blue colored spectrum, and the sidebands are created from absorption or emission of additional IR photons. Both harmonics and sidebands are quite narrow due to multiple EWPs interference. In our experimental condition, the few-cycle IR pulse (6 fs) generates only few attosecond pulses. The corresponding EWPs interference spectrum is relatively broader than the one created from the 25 fs driving

⁷Reconstruction of attosecond beating by interfering two-photon transitions [131]

pulse. The sidebands are created similarly with additional IR photon absorption or emission processes. However, they overlap spectrally with the photoelectrons due to absorption of harmonics (figure 4.7 (b)). The purple colored part marks the overlap region. The implication of the spectral overlap leads to interference between single EWPs originating from single XUV photon ionization ($1s \rightarrow \epsilon p$) and EWPs originating from two-photon ionization ($1s \rightarrow \epsilon p \rightarrow \epsilon d/\epsilon s$). Thus, mixing wavefunction of different parity leads to asymmetric momentum distribution [132].

4.2 Ultrafast electron dynamics of methyl iodide dissociation

Charge transfer refers to the reaction describing the charge moving from one atom to the other. This mechanism occurs widely in physics, chemistry, and biology [133–135]. In ion-atom collision experiments, the neutral atom is ionized by losing electrons to the incoming ion beam [136]. The similar charge transfer effect in ion collision has also been observed in astronomy. The surface of a comet hit by solar winds, containing highly charged ions, produces charge transfer ionization [137]. In molecules, it has been shown that when the internuclear distance between two fragments is too long, the charge transfer is prohibited [133, 138, 139].

The study of ultrafast charge transfer dynamics requires temporal information to follow the time evolution. The usual approach is to use a pump-probe technique, which has been applied from diatomic to polyatomic molecules [138, 139]. Another approach with FEL is to create many charges in a molecule with the absorption of several hard X-rays photons and to study the dynamics within a pulse duration (e.g. 10~30 fs) [140, 141]. In Paper V, we investigated the ultrafast dissociation dynamics of methyl iodide (CH_3I) induced by an XUV pulse after ionization of the 4d shell, at the shape resonance. We developed a classical model to understand the nuclear dynamics within the pulse duration, and discussed the electron dynamics.

4.2.1 Background

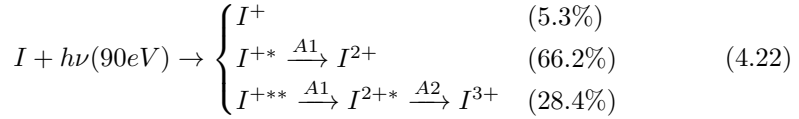
In this section, the relevant processes occurring in our study are briefly reviewed. The photoionization of the methyl iodide is discussed after single photon absorption and multiphoton absorption. The subsequent dissociation can be studied by measuring the kinetic energy of the fragments. We thus present the correspondence between the kinetic energy of the fragment and the molecular potential energy curve. Finally, it was shown that the electron transfer dynamics is effecting the molecular dissociation. We therefore introduce the commonly used model to describe the charge transfer process.

Single Photon Ionization and Fragmentation

Studies of methyl iodide upon photoionization of the iodine 4d shell are relatively scarce [142–145]. In the vicinity of the shape resonance, the respective cross section of atomic iodine, carbon, hydrogen are about 20, 0.6, 0.03 Mb (10^{-18} cm²), respectively [146, 147]. Since the photoionization of iodine dominates, it is useful for understanding the electronic relaxation behaviors of methyl iodide to consider the atomic case.

After photoionization on the 4d shell of neutral iodine, electronic relaxation via Auger decay can lead to two different charge states. The branching ratios at 90 eV

photon energy have been studied by Nahon et al. in atomic iodine vapor [148].



The probability of having a singly charged final state is relatively low ($\sim 5\%$), since the 5s/5p states ionization cross sections are small with respect to 4d shell ionization cross section. The doubly charged final state of iodine is essentially produced with Auger decay (A1) after relaxation of the 4d hole. The valence ionization of the 5s/5p state with a shake-off process also results in a doubly charged state around 4% out of 66%, but this is a minor contribution and is thus neglected in the following. The excited I^{2+*} state will undergo a second Auger decay (A2) when the internal energy exceeds the triple ionization threshold. The A1 Auger decay time of the methyl iodide molecule is found to be around 2 fs [149]. An estimate of the A2 Auger decay time on methyl iodide can be deduced from the iodine molecule I_2 (23 ± 11 fs) and the xenon atom (30.8 ± 1.4 fs) [150, 151] (due to the similar electron configuration of the iodine and the xenon atoms).

Since the most prominent dissociation channel is $CH_3I^{2+} \rightarrow CH_3^+ + I^+$ [152], the focus will be placed on breaking the carbon-iodine bond in the following discussion.

Multiphoton Ionization

The FEL photons flux is high enough for multiphoton absorption/ionization to occur. To the best of our knowledge, no studies have been carried out on highly charged molecular ions, so the data of atomic ions is used to understand the formation of highly charged states of methyl iodide. The cross sections of ionic iodine I^+ and I^{2+} are around 20 Mb due to the shape resonance as in the neutral iodine [153–155], leading to Auger decays after photoionization. To further estimate the evolution of the cross section for higher charge states, we continue to use the similarity of the electronic configuration between iodine and xenon [156–158]. As illustrated in figure 4.8, for the first two charge states of iodine and xenon, the cross sections as a function of the photon energy are similar with essentially an energy shifts of about 10 eV in the position of the shape resonance. We expect that the shape resonance vanishes for the charge states above I^{3+} as in xenon [156, 157], and that mainly the $4d \rightarrow nf(np)$ transitions can occur [154, 155]. Hence, the electronic relaxation should lead to the formation of excited ions.

Sequential photon ionization dominates for low charge states [142]. Instantaneous two photon absorption may occur to overcome the ionization potential of iodine above 7+, but this process is unlikely in our experiment. Figure 4.9 summarizes the energy potential of iodine and the ionization potential of different iodine charge states.

It is worth mentioning the contribution of carbon atom upon photoionization of methyl iodide. The cross section of carbon ions are about 0.5 Mb for both C^+ [161]

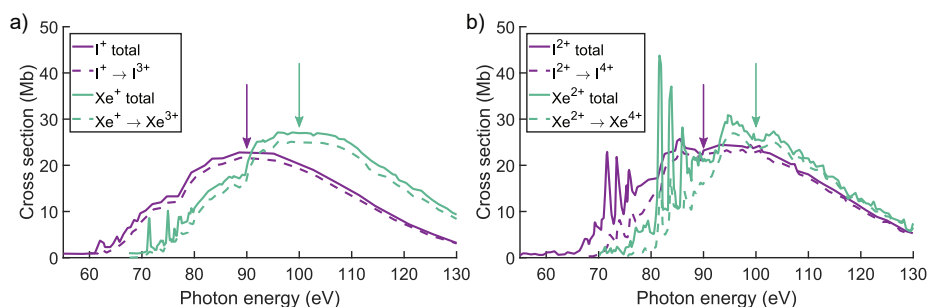


Figure 4.8: Comparison of the ionic iodine and xenon cross sections with main ionization products starting from (a) 1+ and (b) 2+ charge states. The solid lines represent the total ionization cross section, and the dashed lines are the dominant products after photoionization. The iodine lines are purple, and the xenon lines are shown in green. The arrows are used to indicate a 10-eV shift from iodine to xenon in the cross section spectra. The iodine data has been digitized from reference [154], and the xenon data from reference [159]

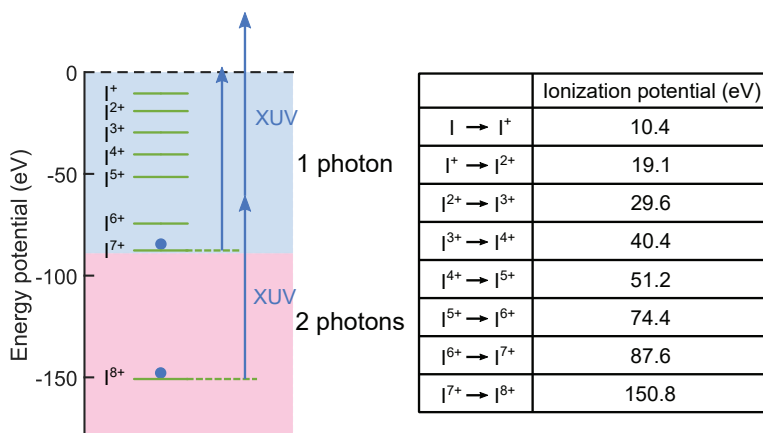


Figure 4.9: Energy potential diagram of atomic iodine with different charges and an ionization potential table. The blue dots represent the remaining electrons, indicating that the current charge state is I⁶⁺. Two different-colored regions in the energy potential are separated at -90 eV. The light blue region can be ionized with a single 90-eV photon, which provides the highest charge number 7+. The pink region requires two 90-eV photons for ionization, moving the iodine charge state from I⁷⁺ to I⁸⁺. (The higher theoretical ionization energy values can be found in the data base [160])

and C²⁺ [162, 163], which is similar to the neutral cross section (0.6 Mb). Since the cross section difference is large (I: 20 Mb vs C: 0.5 Mb), the sequential multiphoton ionization of iodine is a priori expected to dominate, leading to localized charges

on the iodine atom. We found that this hypothesis may not always hold.

Kinetic Energy Release

The Kinetic Energy Release (KER) during dissociation is related to the conversion of the potential energy of the highly charged molecule to the kinetic energy of ionic fragments. For charged ionic fragments, this leads to a Coulomb explosion and is illustrated in figure 4.10 for two charged fragments.

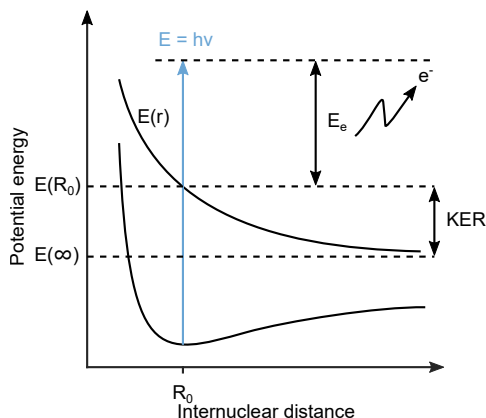


Figure 4.10: Schematic of the kinetic energy release (KER) for dissociation into two fragments. The potential of the excited state is $E(r)$, and the potential energy at infinite distance $E(\infty)$ is called the dissociation limit.

After photoionization, the molecule is prepared in a highly dissociative state. Part of the excess energy E_e is carried out by the photoelectron. The ionized molecule starts to release its potential energy from $E(R_0)$ to the dissociation limit $E(\infty)$. In many cases, the highly dissociative state can be described as a pure Coulomb potential, which is a suitable assumption for studying highly charged molecules [164–166]. In a simple two body break-up case, the kinetic energy release from the Coulomb potential of two charged particles (denoted A, B with p , q charges) separated by a distance R_{eff} can be written as:

$$KER = \frac{pqe^2}{4\pi\epsilon_0 R_{\text{eff}}} \quad (4.23)$$

The momenta of the two charged particles are equal, but with opposite directions. The kinetic energy is shared according to the mass of the fragments:

$$KER(m_A) = \frac{m_B}{m_A + m_B} KER \quad (4.24)$$

$$KER(m_B) = \frac{m_A}{m_A + m_B} KER \quad (4.25)$$

In the methyl iodide molecule, the molecular potential energy curve of the first two molecular charge states and the neutral molecule are shown in figure 4.11. The light blue arrow illustrate the vertical transition from the ground state of the molecule to higher charge states. Except for a few meta stable states in the dication molecule, most of the methyl iodide's ion potential energy curves are close to a Coulomb potential for the larger internuclear distance, as shown by the dashed lines. Especially, the trication states are already similar to the Coulombic potential. It is thus reasonable to assume that the dissociation dynamics of charge states higher than a trication state behave as a pure Coulomb explosion.

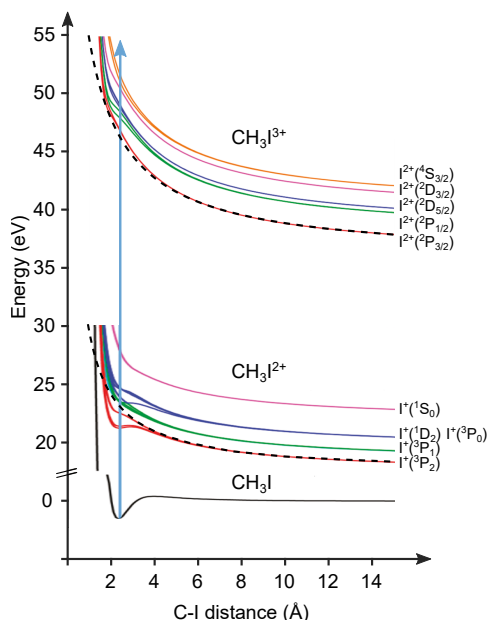
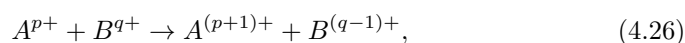


Figure 4.11: Potential energy along the C-I bond of the different CH₃I charge states. The dashed lines for the dication CH₃I and trication CH₃I states represent the Coulomb potential. The potential curves are extracted from reference [166].

Charge transfer

In many FEL experiments, the charge transfer process is important for explaining the delocalization of electron holes in molecules. This mechanism is often described with the Classical Over-the Barrier (COB) model [167]. This model only includes the Coulomb potential between two charged fragments. Assuming there is a charged diatomic molecule AB with localized charge numbers p^+ and q^+ on both atoms, and the charge transfer process is:



the charge transfer should follow the principle of minimum energy. If AB is the diatomic molecule, p must be smaller than $q-1$. We define a coordinate that the electron donor ion with charge number p^+ is at the origin, and the neighbor ion with charge number q^+ is placed at R . The Coulomb potential of the molecular system seen by the charge transfer electron can be written as:

$$V(r, R) = -\left(\frac{p+1}{R-r} + \frac{q}{r}\right), \quad (4.27)$$

where r is the position of the charge transfer electron. The local maximum potential can be determined by setting the derivative of the potential to zero.

$$r_{max} = \frac{R\sqrt{q}}{\sqrt{q} + \sqrt{p+1}}, \quad (4.28)$$

such that the maximum potential is:

$$V(r_{max}, R) = -\frac{q + 2\sqrt{q(p+1)} + (p+1)}{R} \quad (4.29)$$

As long as the electron overcomes the Coulomb barrier with the same potential as the ionization potential of the neighboring atom, the charge transfer can take place. The critical (maximum) distance between two atoms is:

$$-\frac{q + 2\sqrt{q(p+1)} + (p+1)}{R} = -\frac{q}{R} - I_p, \quad (4.30)$$

where I_p is the ionization potential of atom A . The right hand side is the total potential that the electron experiences. If we rewrite equation 4.30, the critical distance of the COB model can be expressed as:

$$R_{crit} = \frac{(p+1) + 2\sqrt{(p+1)q}}{I_p} \quad (4.31)$$

Table 4.1 lists the three atomic ionization potentials for methyl iodide. The ionization energy of C^{2+} to C^{3+} (47.9 eV) is larger than the ionization energy of I^{3+} to I^{4+} . This means that iodine should need more positive charge to attract an electron from C^{2+} . By using equation 4.31, we can calculate the critical distance R_{crit} of each ion pair. The values are listed in table 4.2.

As it can be seen from table 4.2, a higher charge difference gives a larger R_{crit} . In the literature, the COB model provides a good estimation of the charge transfer process at larger internuclear distance [133, 139]. However, at shortest internuclear distances, there is little study on it. The COB model was shown to provide reasonable result for iodine molecule down to 5 Å [168, 169]. In our simulation, the COB model was assumed to be generalizable for all the charge states between carbon and iodine. According to table 4.2, the higher charge state of carbon (electron donor) would require that the charge transfer process can be still described classically. In the methyl group (CH_3), the hydrogen-carbon critical distance is 4.05 Å. We also assumed that the hydrogen atoms could continuously provide electrons until the methyl group is fully charged.

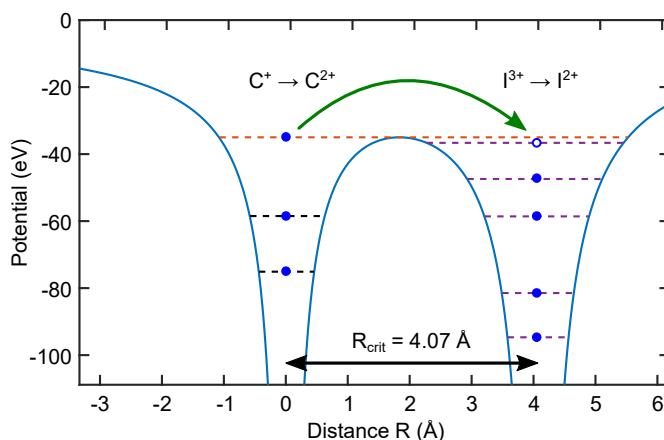


Figure 4.12: Charge transfer between carbon and iodine in the Classical Over the Barrier model. The outermost electron in the C^+ potential is higher than the hole in the I^{3+} potential. As the internuclear distance between carbon and iodine is smaller than the critical distance R_{crit} , the electron can move from carbon to iodine.

Table 4.1: Atomic ionization potential of carbon, hydrogen, and iodine [160].

Charge number	Hydrogen	Carbon	Iodine
0 \rightarrow 1	13.6	11.3	10.4
1 \rightarrow 2		24.4	19.1
2 \rightarrow 3		47.9	29.6
3 \rightarrow 4		64.5	40.4
4 \rightarrow 5		392.1	51.2
5 \rightarrow 6		490.0	74.4
6 \rightarrow 7			87.6

unit eV

4.2.2 Data Analysis of Ions

The experiment was performed with the maximum pulse energy $0.9 \mu\text{J}$ FEL laser at 90 eV with around 75 fs pulse duration. The laser beam was tightly focused down to a $6 \times 8 \mu\text{m}^2$ spot size interacting with the methyl iodide molecules. The configuration of the experimental setup was similar to the one discussed in section 3.1. The methyl iodide ion fragments were collected in coincidence by a reaction microscope (REMI) spectrometer. The highest charged state of the carbon-iodine pair was observed up to (C^{3+} , I^{7+}). The mass correlation between carbons and iodines can be investigated with a photoion-photoion coincidence (PIPICO) 2D

Table 4.2: R_{crit} values as calculated from the COB model. The p and q charge numbers represent the initial charge states before charge transfer. The red values are not allowed energetically, meaning that the charge transfer requires more external energy in order to occur.

		Carbon charge number C^{p+}			
		p=0	p=1	p=2	p=3
I^{q+}	q=1	3.84	2.85	1.94	1.79
	q=2	4.90	3.54	2.38	2.16
	q=3	5.71	4.07	2.71	2.44
	q=4	6.39	4.52	2.99	2.68
	q=5	7.00	4.92	3.23	2.89
	q=6	7.54	5.27	3.45	3.08
	q=7	8.05	5.60	3.66	3.26

unit Å

map.

In figure 4.13, such a 2D map is presented, we can identify the dominant ions time of flight between different charged carbons (C^{p+} , with p=1, 2, 3) and iodines (I^{q+} , with q=2, 3, 4, 5, 6). If a single event creates two charged ions, collected at times t_a and t_b , this event is then recorded as one count on the PIPICO map with the coordinates (t_a, t_b) . Due to momentum conservation, we can observe tilted lines on the PIPICO map. As one charged ion moves forward toward the detector giving a shorter time of flight, another correspondingly charged ion moves backward which results in a longer time of flight.

Transverse velocity correction

Methyl iodide was introduced into vacuum through a supersonic expansion. The molecular beam, hence produced, had a high transverse velocity, which can be seen as the transverse offsets for different ions.

Figure 4.14 presents the spatial-temporal map of methyl iodide molecules. The molecular ions with large mass-to-charge ratios take longer to reach the ion detector, such that a negative transverse offset, shown by the magenta line, can be observed. The transverse velocity of the gas jet can be determined by converting the position to momentum for ions. To this case, the transverse momentum of ions should be written as follows:

$$\begin{cases} p_{ix} = m_i((x_i - x_{i0})/t - \mathbf{V}_{jet}) \\ p_{iy} = m_i(y_i - y_{i0})/t \end{cases} \quad (4.32)$$

We found that the transverse velocity of the CH_3I^{n+} molecule was about 380 ± 80 m/s, which is close to the theoretical molecular beam velocity of methyl iodide at

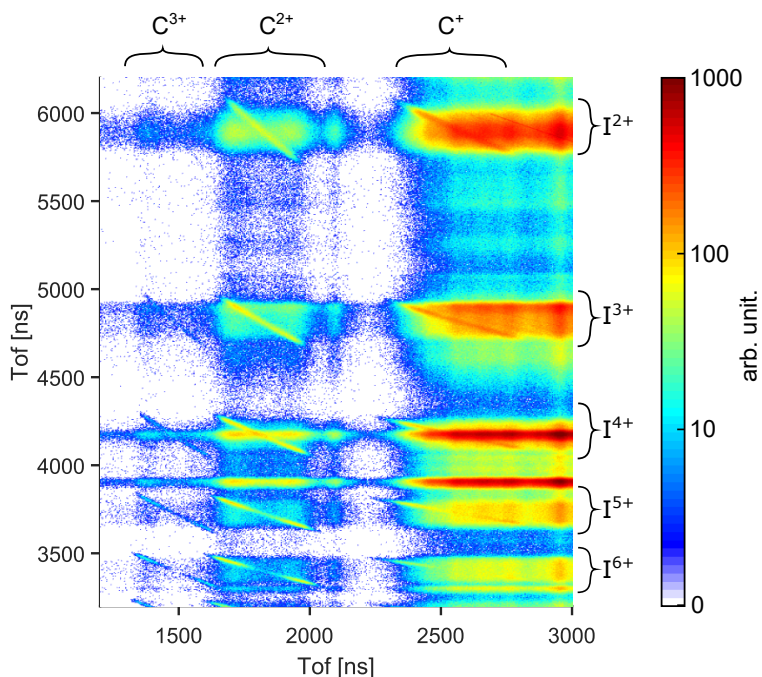


Figure 4.13: Photoion-photoion coincidence (PIPICO) showing the relation between charged carbon groups and iodine ions. The feature with tilted lines corresponds to the break up between carbon and iodine.

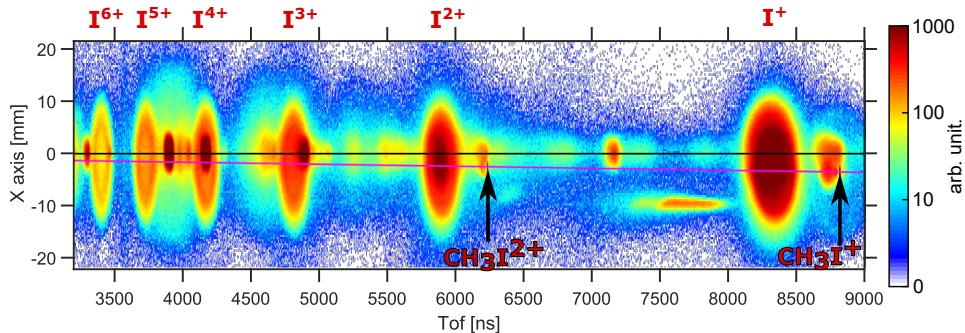


Figure 4.14: The spatial-temporal spectrum showing the heavier fragments of methyl iodide generated from the free electron laser FLASH. The singly and doubly charged methyl iodide molecules (CH_3I^+ and CH_3I^{2+}) appear in the magenta line. The slope of the magenta line corresponds to the transverse velocity of the molecular jet. The black line shows the reference line for the background signals, which do not have any transverse velocities from the molecular jet.

room temperature (~ 320 m/s) [170–172].

Acceptance of Detection

Even though, the REMI spectrometer was operated at a strong electrostatic field (≈ 80 V/cm) in the methyl iodide experiment, the most energetic carbon ions were not collected with a 4π acceptance angle. To determine the effective acceptance angle, we used SIMION simulations with the experimental KER of carbon ions. The simulation result is shown in table 4.3, and these value were used to correct the experimental branching ratio.

Table 4.3: Simulated acceptance solid angle of the carbon ions in different carbon-iodine pairs (in unit of 4π)

		Carbon charge number C^{p+}		
		p=1	p=2	p=3
I^{q+}	q=1	1	0.991	-
	q=2	0.979	0.998	-
	q=3	0.918	0.975	0.983
	q=4	0.869	0.927	0.949
	q=5	0.807	0.837	0.845
	q=6	0.744	0.703	0.723
	q=7	-	0.660	0.669

4.2.3 Classical Sequential Ionization Model

In Paper V, we developed a model based on classical mechanics to study the molecular dissociation of methyl iodide. The model assumes a sequential charging mechanism which includes photoionization and Auger decays. The charge transfer from the iodine to the methyl carbon follows the Classical Over the Barrier (COB) model. The distribution of positive charges in the methyl group is described by fractional charges.

Sequential Ionization

Multiphoton sequential ionization can produce many final charged states, and a general approach to solve this problem is done by using a set of coupled rate equations [173]. As the system absorbs more photons, it can be very difficult to determine all the parameters, such as the actual cross sections of different charged ions. The sequential ionization timing then becomes very ambiguous. To determine the sequential ionization timing on methyl iodide, we used a randomly distributed time sequence weighted by the FEL intensity profile for photoionization timing.

The Auger decays were added right after photoionization on iodine ions with less than 3+ charges (i.e. I^{q+} , with $q < 3$).

After we defined the sequential ionization timing, the nuclear dynamics can be calculated by assuming Coulomb potential curves as illustrated in figure 4.15 [16]. The carbon-iodine dissociation dynamics follow the different potential curves, and the accumulated potential energy from the sequential charging process is released into KER.

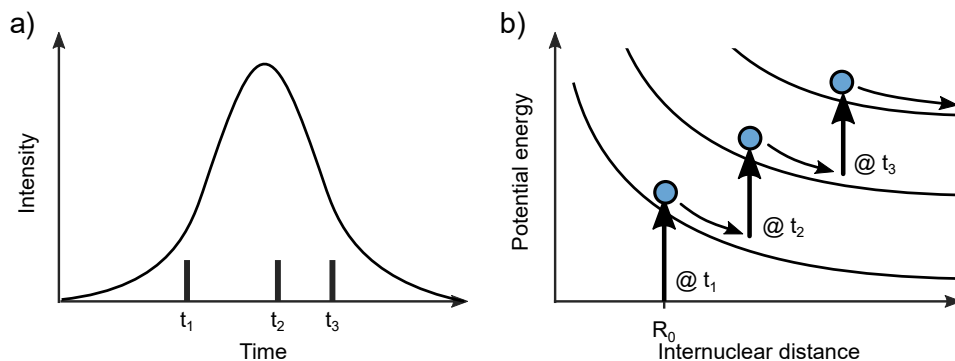


Figure 4.15: Illustration of the sequential ionization for the carbon-iodine pair transiting between Coulomb potential curves. (a) The time sequence (t_1, t_2, t_3) is randomly generated within the FEL pulse duration. The Auger decays are also included in the ionization time sequence. (b) The principle of the classical model shows the accumulate potential energy of the charge states during the sequential ionization process.

By applying a Monte Carlo method, the ensemble of ionization time sequence is represented in a temporal distributions, which can be used to determine the spatial distribution of the internuclear distance, and thereby study the nuclear wave packet dynamics along the C-I bond.

Fractional Charge Distribution

It was reported that hydrogen atoms in the methyl group become protons during the multiple photoionization [140, 141]. To include the hydrogen contribution during the methyl iodide dissociation, we assumed a three-fold symmetry breakup. As the methyl group gets positively charged via charge transfer from the iodine ion, the charges do not purely localized on the carbon atom. Instead, the charges are shared by all the atoms in methyl group. In our work, we introduced a factor to describe the sharing called the fractional charge ζ . For the first charge on the methyl group, the fractional charge ζ on each hydrogen can vary from 0 to 1/3, whereas the remaining charge is placed on the carbon. For example, when the first positive charge is shared in the methyl group, a 10 % fractional charge gives $1 - 3 \times 10\% = 70\%$ charge on the carbon and 10% on each hydrogen. The subsequent charging on the methyl group follows the principle of minimum energy, i.e. three

10% charged hydrogens share the next charge with $3 \times 30\%$, and the remaining 10% is placed on the 70% charged carbon. This process continues until three hydrogens are fully charged (i.e. $10\% \rightarrow 40\% \rightarrow 70\% \rightarrow 100\%$) and the charge number on the carbon becomes an integer (i.e. $70\% \rightarrow 80\% \rightarrow 90\% \rightarrow 100\%$) for producing a higher charge state of carbons in the later charge transfer process.

4.2.4 Results

Thanks to 3D momentum imaging spectrometer, the momentum and kinetic energy of ions can be calculated. The momentum correlation between the carbon ions and iodine ions can inform about the hydrogen contribution during the dissociation. One example is given for the momentum correlation between C^{2+} and I^{3+} in figure 4.16.

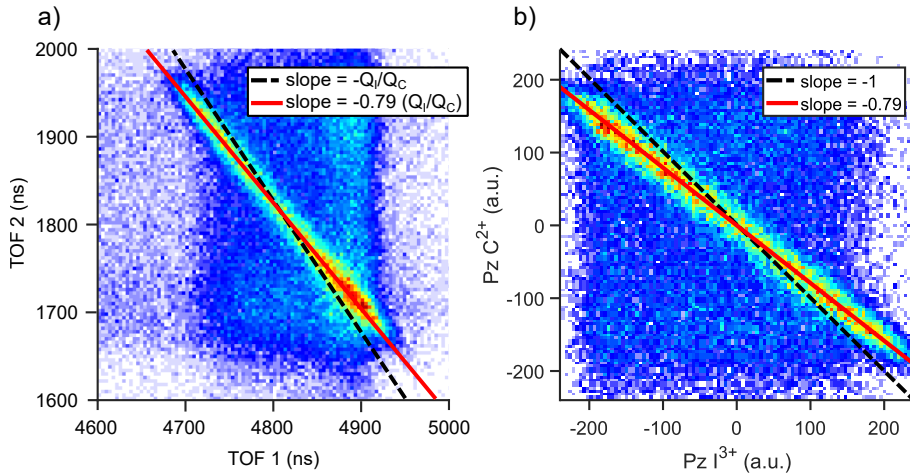


Figure 4.16: Momentum correlation of C^{2+} and I^{3+} in two representation. (a) Time of flight (b) Momentum. The black dashed lines are for ideal two body break-up, and red solid lines are the experimental fitted lines.

During the dissociation process, the hydrogen atoms provide momenta to the carbon ion with an opposite direction. The final momentum ratio between carbon and iodine is only 79 % left in this (C^{2+} , I^{3+}) final charge states. The ratio is called momentum correlation k in Paper V.

As one could expect from a dissociation driven by Coulomb explosion, the KERs of all pairs increase as a function of the iodine charge state, as well as the carbon charge state. By comparing the measured KER to an instantaneous Coulomb explosion model, shown as straight lines in the figure 4.17 (a) for different initial internuclear distances between C^{p+} and I^{q+} , we can conclude that nuclear dynamics plays a central role, as was already seen in Erk et al. studies [174]. The KER of the pair C^+ and I^+ corresponds typically to the instantaneous formation of two charges at a distance around 2.14 Å, while the pair C^+ and I^{6+} can be

understood as the formation of 7 charges at a distance longer than 4 Å. In figure 4.17 (b), the error bar of each charge state represents the standard deviation width ($\pm\sigma$), or also called the Kinetic Energy Distribution (KED).

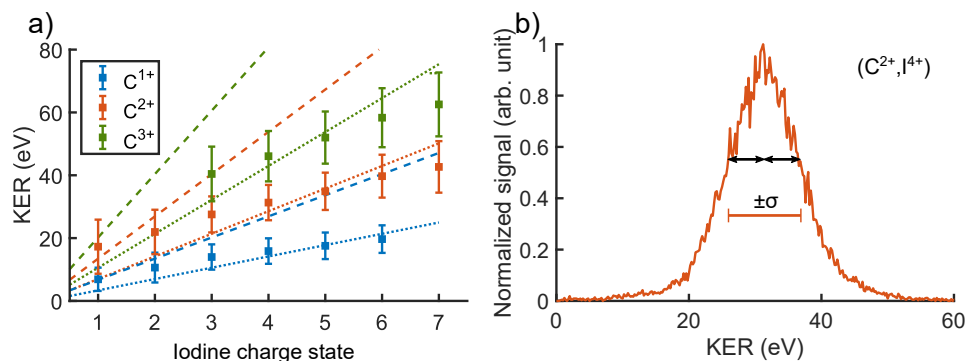


Figure 4.17: Kinetic energy release of observed carbon-iodine charged states. The data are presented in three colors for three different carbon charge states. (a) Measured KER of all charge states with support lines calculated from Coulomb explosion model. The dashed and dotted lines represent Coulomb explosion from instantaneous charge formation at equilibrium internuclear distance 2.14 Å and at 4 Å, respectively. (b) The KED is defined with two standard deviation in the KER of C²⁺ and I⁴⁺ charge state.

Charge Transfer Discussion

The simulation reproduces the three measurable quantities, i.e. the momentum correlation between carbon and iodine, the branching ratio, and the KER. We found that the charge transfer plays an important role on both branching ratio and KER. Here, we list out two main observations from studying charge transfer dynamics.

For each charge state, each possible charge transfer is checked individually. As we let one charge transfer path open, the other charge transfer paths are switched off. With this analysis, we found that the charge transfers from C⁺-I³⁺ to C²⁺-I²⁺ and C⁺-I⁴⁺ to C²⁺-I³⁺ are the main contributions to produce the C²⁺ state. The charge transfer strength comes from the interplay between the sequential ionization and the charge transfer. During the sequential ionization, the carbon-iodine bond continues to elongate. If the charging speed is slow, the bond will be longer than the critical distance, so the charge transfer is forbidden. Thus, the charge transfer condition is more preferable to occur at the earlier time. By studying the charge transfer from C⁺ to C²⁺ condition, the COB model seems to work around 4.1~4.5 Å in the methyl iodide dissociation.

For the C³⁺ charge states, the charging process cannot be described with COB model due to our measured KER of the C³⁺ charge states that are too low. By considering the additional ionization on carbon, the simulation shows good agree-

ment with the experimental observation. The possible mechanisms of the ionization are either the carbon photoionization or a process similar to Penning ionization, which is the ionization from interchanging electrons in an excited atom. Since the photoionization of iodine can possibly populate Rydberg states, the excited electron can be ionized after charge transfer. For example, a precursor state $C^{2+}-I^{4+*}$ could evolve into $C^{3+}-I^{4+}$, where a precursor state refers to the non-stationary wave packet leading to the dissociation channel (C^{2+}, I^{4+*}) or (C^{3+}, I^{4+}) .

SUMMARY AND OUTLOOK

In this thesis, we have presented experimental tools and supporting models for studying ultrafast electron dynamics in atomic and molecular systems with two advanced sources of XUV radiation, i.e. a high repetition rate laboratory source of attosecond pulse trains and intense FEL pulses from the FLASH facility.

At the core of the presented work, is the design and development of a compact electron and ion angle-resolved momentum imaging spectrometer (CIEL), which is a perfect match to our high repetition rate OPCPA laser source. During commissioning of the spectrometer, electron-ion coincidence detection rates of tens of kHz were achieved, which constitutes a major step compared to the low repetition rate laser sources that are commonly used in the field of attosecond science. The spectrometer is presented in Paper [III](#), where we also discuss in detail the angle resolved electron resolution, an aspect often neglected in the literature. The advantage of our spectrometer design is that electrons can be resolved with a full solid angle in a single measurement. This avoids patching together independent measurements, which otherwise could be compromised by fluctuations of the light source. Furthermore, valuable acquisition time is saved.

Another essential ingredient to the success of the presented work is the continuous further development of the high-repetition rate, CEP-stable, few-cycle OPCPA laser source. The laser is discussed in detail in Paper [I](#). Apart from driving HHG, the laser was used for studying metallic and semiconductor nanostructures in conjunction with PEEM imaging (Paper [VI](#)). The repetition rate of the laser is two orders of magnitude higher than what is common in the field of attosecond science. The combination of the laser and our spectrometer can pave the way for advanced coincidence detection schemes in attosecond time-resolved spectroscopy, while convenient data acquisition time can be maintained. The high repetition rate of the laser system however comes at the price of low energy per pulse. To address this issue, a high pressure generation gas target was developed to generate XUV attosecond pulses efficiently via HHG (Paper [I](#)). A higher focal intensity in the gas should further improve the generation efficiency in Neon [\[36\]](#), enabling to address

ionization dynamics beyond the valence shell, e.g. the 4d shells in xenon or iodine [175]. Further advance into the soft-X-ray spectral range (e.g. carbon K-shell 284 eV) can be achieved with longer wavelengths laser sources in the mid-infrared spectral range [176] for driving HHG [177]. Such approaches will open up for routinely studying the dynamics of the inner atomic shells with attosecond time resolution.

The thesis comprises two key studies of ultrafast electron dynamics. In Paper IV, the OPCPA driven high repetition rate attosecond source was used to investigate the interference of EWPs, originating from the ionization of helium atoms in the presence of a dressing IR field. In Paper V, FEL pulses were employed to study the interplay between photoionization, Auger decay and electron charge transfer during the dissociation of methyl iodide molecules.

In Paper IV, we showed that the photoionization can be asymmetric with respect to the polarization axis of the radiation, an initially unexpected effect. Within the plane wave approximation, i.e. neglecting the influence of the ionic potential in our theoretical description, the asymmetric photoemission can be explained by only considering the properties of the attosecond pulses and the dressing IR field. The resulting photoelectron spectrum can then be interpreted as interference between one-photon and two-photon induced EWPs. Furthermore, the interference should also be influenced by the phase of the two-photon transition matrix elements [178, 179]. Recently, it was shown that angularly resolved measurements close to the ionization threshold are very sensitive to two-photon ionization dynamics [180, 181]. Such effects go beyond the approximations considered in our work, but would be very interesting to investigate with our apparatus. The approach of scanning the CEP of the IR field, used in Paper II and Paper IV, provides another degree of freedom for acquiring information about photoionization dynamics. This should in the future be combined with pump-probe techniques to obtain two-dimensional scans that carry additional information and improve our understanding of the electron dynamics.

In Paper V, the FEL pulse energy was sufficient to ionize methyl iodide molecules by sequential multiphoton ionization on a similar time scale as the molecule dissociates, allowing us to study the role of charge transfer in the molecule. A classical model was developed providing insights into the electron dynamics. While charge transfer for the internuclear distance (≥ 4 Å) is well understood, our analysis points out that 4d shell ionization dynamics cannot be neglected for shorter internuclear distance (≤ 4 Å). However, to directly resolve electron dynamics in the highly nonlinear regime, a shorter FEL pulse and a pump-probe experiment would be inevitable. Large efforts are currently undertaken at FEL facilities to solve technical issues like the temporal jitter between optical lasers and FEL pulses [182–185] as well as obtaining shorter pulses from FELs [186, 187]. Recently, pump-probe attosecond pulses have been generated from an FEL in the hard X-ray regime [188].

To conclude, this thesis has dealt with advanced aspects of ultrafast electron dynamics in atomic and molecular systems. The developed experimental tools can be fundamental for further advancing the research field of attosecond science.

TRANSVERSE ELECTRON MOTION IN UNIFORM ELECTRIC AND MAGNETIC FIELD

With two different direction of magnetic field, the electron circular motion will move in counter clockwise or clockwise (figure A.1). Consider the magnetic field is along the $+z$ direction, the counter clockwise motion can be solved as following. The electron is assumed to have an initial momentum \mathbf{p}_\perp , and the trajectory is moving in an cyclotron frequency ω . The transverse motion of electron r can be written as the following equation when the electron hits the detector at a certain time t :

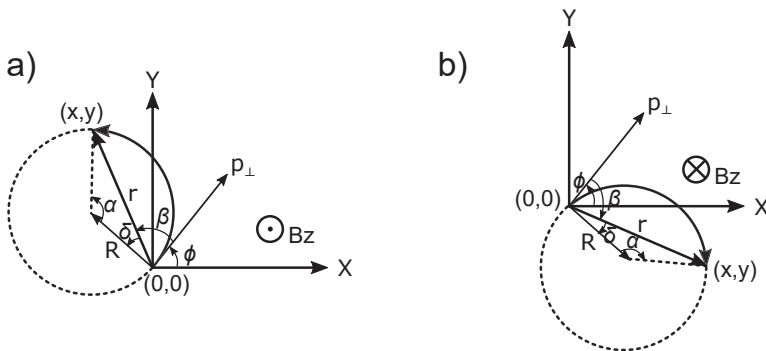


Figure A.1: The electron transverse motion in a uniform magnetic field B . (a) When magnetic field is along the z axis, the electron moves in counter clockwise direction. (b) As the magnetic field switch to opposite direction, the electron moves in clockwise direction.

$$r = 2R \sin \frac{\alpha}{2} = 2R \sin \frac{\omega t}{2} \quad (\text{A.1})$$

The amplitude of the momentum \mathbf{p}_\perp can be expressed as a function of cyclotron frequency by substituting equation A.1 to equation 3.12.

$$|\mathbf{p}_\perp| = p_\perp = ReB = \frac{reB}{2 \sin \frac{\omega t}{2}} = \frac{rm\omega}{2 \sin \frac{\omega t}{2}} \quad (\text{A.2})$$

By solving the geometry problems, $\delta = \pi/2 - \alpha/2$, $\beta = \pi/2 - (\pi/2 - \alpha/2) = \alpha/2$. The angle of ϕ is equal to $\tan^{-1}(y/x) - \alpha/2$. Then, the momentum p_x and p_y can be written as a function of x, y, t with trigonometric identities (**counter clockwise**):

$$\begin{cases} p_x = p_\perp \cos \phi = p_\perp \left(\frac{x}{r} \cos \frac{\alpha}{2} + \frac{y}{r} \sin \frac{\alpha}{2} \right) = \frac{m\omega}{2} (x \cot \frac{\omega t}{2} + y) \\ p_y = p_\perp \sin \phi = p_\perp \left(\frac{y}{r} \cos \frac{\alpha}{2} - \frac{x}{r} \sin \frac{\alpha}{2} \right) = \frac{m\omega}{2} (y \cot \frac{\omega t}{2} - x) \end{cases} \quad (\text{A.3})$$

If the magnetic field is along the -z direction, it only needs to change the sign of the cyclotron frequency to rotate in **clockwise** direction:

$$\begin{cases} p_x = \frac{m\omega}{2} (x \cot \frac{\omega t}{2} - y) \\ p_y = \frac{m\omega}{2} (y \cot \frac{\omega t}{2} + x) \end{cases} \quad (\text{A.4})$$

RESOLUTION OF THE SPECTROMETER

Electrons energy resolution

Since the electron is moving in helical trajectory, it is necessary to introduce some parameters before we calculate the resolution of kinetic energy. First, we have an electron with initial velocity v and with θ angle to the z axis. The radial distance r to the origin can be written in as

$$r = 2 \frac{v \sin \theta}{\omega} \sin\left(\frac{\omega t}{2}\right) \quad (\text{B.1})$$

The v_z is the component for electron moving in the z axis, and it can be represented as:

$$v_z = \frac{L}{t} - \frac{qE}{2m}t \quad (\text{B.2})$$

After square of the v_z , and we can plug the equation (B.1) in, then we have the r represented in t:

$$\begin{aligned} v_z^2 &= v^2(\cos^2 \theta) = v^2(1 - \sin^2 \theta) \\ \left(\frac{L}{t} - \frac{qE}{2m}t\right)^2 &= v^2\left(1 - \left(\frac{r\omega}{2v}\right)^2 \frac{1}{\sin^2\left(\frac{\omega t}{2}\right)}\right) \end{aligned}$$

More steps,

$$\begin{aligned} \frac{1}{4}r^2\omega^2 \frac{1}{\sin^2\left(\frac{\omega t}{2}\right)} &= v^2 - \left(\frac{L}{t} - \frac{qE}{2m}t\right)^2 \\ r &= 2\sqrt{v^2 - \left(\frac{L}{t} - \frac{qE}{2m}t\right)^2} \left| \frac{\sin\left(\frac{\omega t}{2}\right)}{\omega} \right| \\ r &= 2\sqrt{\frac{2E_k}{m} - \left(\frac{L}{t} - \frac{qE}{2m}t\right)^2} \left| \frac{\sin\left(\frac{\omega t}{2}\right)}{\omega} \right| \quad (\text{B.3}) \end{aligned}$$

The next step is to estimate the energy deviation/error from the detector resolution. The measurable quantities are position (x,y) and time t, and they are assumed to be independent with each other. Additionally, the error of measured quantities from detector is assumed to be normal distribution, the energy deviation can be written as:

$$\Delta E_k = \sqrt{\left(\frac{\partial E_k}{\partial x}\right)^2 \sigma_x^2 + \left(\frac{\partial E_k}{\partial y}\right)^2 \sigma_y^2 + \left(\frac{\partial E_k}{\partial t}\right)^2 \sigma_t^2} \quad (\text{B.4})$$

The total energy E_k can be written as the three different direction of momentum:

$$E_k = \frac{1}{2m}(p_x^2 + p_y^2 + p_z^2) \quad (\text{B.5})$$

The differential E_k with respect to x is:

$$\begin{aligned} \frac{\partial E_k}{\partial x} &= \frac{1}{2m} \frac{\partial}{\partial x} [p_x^2 + p_y^2] = \frac{1}{2m} [2p_x \frac{m\omega}{2} \cot\left(\frac{\omega t}{2}\right) - 2p_y \frac{m\omega}{2}] \\ &= \frac{\omega}{2} [p_x \cot\left(\frac{\omega t}{2}\right) - p_y] = \frac{\omega}{2} \left[\frac{m\omega}{2} (x \cot\left(\frac{\omega t}{2}\right) + y) \cot\left(\frac{\omega t}{2}\right) - \frac{m\omega}{2} (y \cot\left(\frac{\omega t}{2}\right) - x) \right] \\ &= \frac{m\omega^2}{4} [x \csc^2\left(\frac{\omega t}{2}\right)] \end{aligned} \quad (\text{B.6})$$

Similarly, the y component differential is:

$$\begin{aligned} \frac{\partial E_k}{\partial y} &= \frac{1}{2m} \frac{\partial}{\partial y} [p_x^2 + p_y^2] = \frac{1}{2m} [2p_x \frac{m\omega}{2} + 2p_y \frac{m\omega}{2} \cot\left(\frac{\omega t}{2}\right)] \\ &= \frac{\omega}{2} [p_x + p_y \cot\left(\frac{\omega t}{2}\right)] = \frac{\omega}{2} \left[\frac{m\omega}{2} (x \cot\left(\frac{\omega t}{2}\right) + y) + \frac{m\omega}{2} (y \cot\left(\frac{\omega t}{2}\right) - x) \cot\left(\frac{\omega t}{2}\right) \right] \\ &= \frac{m\omega^2}{4} [y \csc^2\left(\frac{\omega t}{2}\right)] \end{aligned} \quad (\text{B.7})$$

The time differential is slightly complicated:

$$\begin{aligned} \frac{\partial E_k}{\partial t} &= \frac{1}{2m} [2p_x \frac{\partial p_x}{\partial t} + 2p_y \frac{\partial p_y}{\partial t} + 2p_z \frac{\partial p_z}{\partial t}] \\ &= \frac{1}{2m} [2p_x \frac{m\omega}{2} x \frac{\omega}{2} (-\csc^2\left(\frac{\omega t}{2}\right)) + 2p_y \frac{m\omega}{2} y \frac{\omega}{2} (-\csc^2\left(\frac{\omega t}{2}\right)) + 2p_z \frac{\partial p_z}{\partial t}] \\ &= \frac{\omega^2}{4} \left[\frac{m\omega}{2} (x \cot\left(\frac{\omega t}{2}\right) + y) x (-\csc^2\left(\frac{\omega t}{2}\right)) + \frac{m\omega}{2} (y \cot\left(\frac{\omega t}{2}\right) - x) y (-\csc^2\left(\frac{\omega t}{2}\right)) \right] + \frac{p_z}{m} \frac{\partial p_z}{\partial t} \\ &= \frac{\omega^2}{4} \frac{m\omega t}{2} \left[[x^2 \cot\left(\frac{\omega t}{2}\right) + xy] + [y^2 \cot\left(\frac{\omega t}{2}\right) - xy] \right] (-\csc^2\left(\frac{\omega t}{2}\right)) + \frac{p_z}{m} \frac{\partial p_z}{\partial t} \\ &= \frac{m\omega^3}{8} r^2 \cot\left(\frac{\omega t}{2}\right) (-\csc^2\left(\frac{\omega t}{2}\right)) + \frac{p_z}{m} \frac{\partial p_z}{\partial t} \end{aligned} \quad (\text{B.8})$$

Additionally, with the equation set (3.13) and assuming the Δx is as same as Δy , the ΔE_k can be derived:

$$\Delta E_k = \sqrt{\frac{m^2 \omega^4}{16} (r^2 \csc^2(\frac{\omega t}{2})) \sigma_x^2 + (\frac{p_z}{m} \frac{\partial p_z}{\partial t} - \frac{m \omega^3}{8} r^2 (\cot(\frac{\omega t}{2}) \csc^2(\frac{\omega t}{2})))^2 \sigma_t^2} \quad (\text{B.9})$$

Electrons momentum resolution

The momentum resolution is commonly used in COLTRIMS experiments. As similar as energy resolution, the measurable parameters are still position (x,y) and time t. The momentum error can be written down similarly:

$$\Delta p = \sqrt{(\frac{\partial p}{\partial x})^2 \sigma_x^2 + (\frac{\partial p}{\partial y})^2 \sigma_y^2 + (\frac{\partial p}{\partial t})^2 \sigma_t^2} \quad (\text{B.10})$$

The momentum p is the magnitude of the momentum.

$$p = \sqrt{p_x^2 + p_y^2 + p_z^2} \quad (\text{B.11})$$

Without writing down the complete equation, the difference between momentum error and the energy error is:

$$\Delta E_k = \frac{p \Delta p}{m} \quad (\text{B.12})$$

It means that the energy error increases as the momentum goes up. Another resolution representation is normalized momentum/energy. After rewriting the equation above, the normalized momentum ($\Delta p/p$) only differs with a constant factor 0.5 to the normalized energy ($\Delta E_k/E_k$), i.e:

$$\frac{\Delta p}{p} = \frac{1}{2} \frac{\Delta E_k}{E_k} \quad (\text{B.13})$$

DIFFERENTIAL CROSS SECTION

The measured 3D momentum imaging can be converted to differential cross section ($d\sigma/d\Omega$). The relation between the measured momentum and the differential cross section is as shown as the followings.

Since we have a full angular resolved spectrometer, all the events are collected with 4π solid angle. Under the same number of incoming photons, the photoionization cross section σ is proportional to the total number of counts N_{tot} . Within a small solid angle $\Delta\Omega$, the measured counts N is then proportional to a finite size of the cross section $\Delta\sigma$. The relation between all the parameters above can be written as:

$$\frac{N}{N_{tot}} = \frac{\Delta\sigma}{\sigma} \quad (\text{C.1})$$

The finite size of cross section can be expressed as the differential cross section $d\sigma/d\Omega$ times the small solid angle $\Delta\Omega$ under first order approximation.

$$\Delta\sigma \approx \frac{d\sigma}{d\Omega} \Delta\Omega \quad (\text{C.2})$$

If the system has a symmetric axis (conventionally along z axis or polarization axis) with rotational symmetry, the small solid angle can be integrated along the azimuthal angle ϕ , giving only one polar angle dependence θ . The measured differential cross section with rotational symmetry can be represented as a function of the polar angle θ in spherical coordinates:

$$\frac{d\sigma}{d\Omega} \approx \frac{\sigma}{N_{tot}} \frac{N_{int\phi}}{\Delta\Omega_{int\phi}} = \frac{\sigma}{N_{tot}} \frac{N_{int\phi}}{2\pi \sin\theta \Delta\theta} \quad (\text{C.3})$$

, where $N_{int\phi}$ and $\Delta\Omega_{int\phi}$ denote the integration along the azimuthal angle ϕ for number of counts and solid angle, respectively. The cross section σ is given by the literature, and the small polar angle $\Delta\theta$ is the step size of the measured histogram. To have the differential cross section plot from the 3D momentum measurements, the azimuthal integrated histogram should be corrected by the $\sin\theta$ factor.

COMMENTS ON THE PAPERS

I **Compact 200 kHz HHG source driven by a few-cycle OPCPA**

Anne Harth, Chen Guo, Yu-Chen Cheng, Arthur Losquin, Miguel Miranda, Sara Mikaelsson, Christoph M Heyl, Oliver Prochnow, Jan Ahrens, Uwe Morgner, Anne L'Huillier and Cord L Arnold.

Journal of Optics **20**, 014007 (2017).

An efficient high order harmonic generation (HHG) based on a high-repetition rate 200 kHz OPCPA few cycle laser, which provides 6 fs pulses with 9 μJ pulse energy, was built and characterized. The HHG source has been tested with three different inert gas, neon, argon, and krypton, and the highest conversion efficiency was found around 10^{-6} with only 3 μJ incident pulse energy in krypton. This high conversion efficiency was achieved by optimizing the OPCPA spatially and temporary and with a well-designed high pressure gas jet.

I contributed to the measurement of the OPCPA laser, and characterized the temporal pulse width with dispersion scan. Also, I also built a slow-feedback loop for temporal stabilization by monitoring the idler of the 1st NOPA stage output. For the HHG part, I worked with Anne Harth and Chen Guo for characterizing the harmonics spectrum, spatial profiles, and the conversion efficiency.

II Phase control of attosecond pulses in a train

Chen Guo, Anne Harth, Stefanos Carlström, Yu-Chen Cheng, Sara Mikaelsson, Erik Mårzell, Christoph Heyl, Miguel Miranda, Mathieu Gisselbrecht, Mette B Gaarde, Kenneth J Schafer, Anders Mikkelsen, Johan Mauritsson, Cord L Arnold and Anne L’Huillier.

Journal of Physics B: Atomic, Molecular and Optical Physics **51**, 034006 (2018).

The high harmonic generation (HHG) source presented in this work was studied by varying the CEP and the dispersion of the fundamental field with the goal to control the phase of attosecond pulses. A theoretical model was developed to quantify the properties of the HHG source. The experimental results supported by our model show that the phase of attosecond pulses can be controlled precisely with the fundamental driving field.

I worked on gathering the HHG dispersion scan data, contributed to the scientific discussion and prepared part of the figures for the manuscript.

III A compact electron-ion coincidence spectrometer for attosecond time-resolved spectroscopy at high repetition rate

Yu-Chen Cheng, Saikat Nandi, Lisa Rämisch, Sara Mikaelsson, Bart Oostenrijk, Neven Ibraković, Anna Olofsson, Emma Simpson, Johan Mauritsson, Anne L’Huillier, and Mathieu Gisselbrecht.

(2019) *in manuscript*.

A new 3D momentum imaging spectrometer was built in Lund. The paper discusses the electron resolution of momentum imaging spectrometer with various design, and the limitations of the electron resolutions were identified and quantified with measurements.

I have designed and constructed the instrument, performed the experiment, analyzed the data, developed the simulation codes, and written the part of the paper.

IV CEP controlled photoelectron emission using wave packet interference

Yu-Chen Cheng, Sara Mikaelsson, Saikat Nandi, Lisa Rämisch, Chen Guo, Anne Harth, Jan Vogelsang, Miguel Miranda, Cord L. Arnold, Anne L'Huillier, and Mathieu Gisselbrecht.
(2019) *in manuscript*.

We studied the photoelectron angular distribution asymmetry after two photon absorption from XUV attosecond pulses and few-cycle femtosecond IR field. The asymmetric pattern is from electron wave packet interference, and can be controlled by the CEP of IR field. With the help of the theoretical model, we found that the interference is similar to a slit experiment in time. I have worked on constructing experimental setups, performed the experiments, analyzed the data, and contributed to the redaction of the manuscript.

V Ultrafast dynamics of methyl iodide studied with XUV Free Electron Laser

Yu-Chen Cheng, Bart Oostenrijk, Jan Lahl, Sylvain Maclot, Sven Augustin, Georg Schmid, Kirsten Schnorr, Severin Meister, Dimitrios Rompotis, Bastian Manschwetus, Cédric Bomme, Benjamin Erk, Daniel Rolles, Rebecca Boll, Pavel Olshin, Artem Rudenko, Michael Meyer, Per Johnsson, Robert Moshhammer, and Mathieu Gisselbrecht.
(2019) *in manuscript*.

The XUV multiphoton ionization of methyl iodide has been studied experimentally and analyzed by developing a classical model to describe the dissociation dynamics. This classical model provides us a picture for understanding the interplay between ultrafast processes, such as multiple ionization, charge transfer, that occur within the femtosecond pulse duration. I have worked during the beam time, analyzed the data, developed the model and simulations, and written the majority of the paper.

VI Spatial Control of Multiphoton Electron Excitations in InAs Nanowires by Varying Crystal Phase and Light Polarization

Erik Mårzell, Emil Boström, Anne Harth, Arthur Losquin, Chen Guo, Yu-Chen Cheng, Eleonora Lorek, Sebastian Lehmann, Gustav Nylund, Martin Stankovski, Cord L. Arnold, Miguel Miranda, Kimberly A. Dick, Johan Mauritsson, Claudio Verdozzi, Anne L'Huillier, and Anders Mikkelsen.

Nano Letters **18**, 907-915 (2018).

In this paper, we studied the multiphoton electron emission from InAs nanowires with different crystal structure and polarization of laser source. The nanowire consists of two crystalline segments wurtzite and zincblende, and their electron emission are strongly depending on the incident polarization of laser. This study shows how the crystal structure can affect the electron emission under multiphoton excitation.

I participated in the experiments and mainly worked on providing and maintaining the OPCPA laser light source.

ACKNOWLEDGEMENTS

The works that has been done in this thesis is impossible for me to accomplish without many people's help. During my PhD study period, I got plenty of help from too many people. Especially, I would like to thank my supervisor, Mathieu. You are an inspiring adviser providing many ideas on the research studies. As I was too deeply digging into technical things, your thoughts usually help. Thank you for the knowledge on the electronics of the DLD detectors. Without your help, it would be tough to complete a measurement. Besides, you always share your philosophical thoughts, and that is quite interesting.

I would like to thank my co-supervisor Anne. You are the most approachable professor I have ever met, and your special personality broke my impression about the "big bosses". Thank you for letting me to join your group, and it is honor to be in this group.

I also would like to thank my co-supervisor Cord. You provide many insight point of view about the laser optics and technologies, which are very useful for working with our cutting-edge high-repetition-rate laser system.

Thanks to my MHz colleagues (Please forgiving me for omitting the 0.2). Thanks Anne H. You are always positive and work with passion. This really affects me on the research. Thank you Chen, thank you for being my mentor since I started my PhD. It is very nice to have a chinese colleague that can chat with more precise words on describing things. Thanks Arthur, I really enjoyed the time we worked and shared ideas. Thank you Saikat. I think if I was the only one working on the spectrometer, it would not come out the asymmetric photoemission experiment. Thank you for your help and the vacuum knowledge. Thanks Sara, each time when I talk with you, I always get influence from your positive attitude. That is really nice. Thank you Jan V, you are very outstanding on handling several lab things. It is impressive for me. Thank you Fabian, it was very enjoyable to chat with you and ask plenty of questions. Thank you Ivan, for sharing the experience about the Russia and also some cool stories. Thank you Lisa for your brightness and sharing your thoughts. I would like to also thank Miguel for his expertise on the laser system. Thank you everyone for the contribution on the MHz laser system.

Thanks for the close colleagues working in the same big group. I appreciate that we have several groups cooperating with each other. Thanks Atto group

people: David K, Esben, Maïte, Hugo L, Shekhar, Lana, Marcus, Christoph, Ello, Stefanos, Bastian, Marija, Anna, Simon, Timothé. Thanks to intense beam line group people: Jasper, Linnea, Filippo, H el ene, Hugo D. If you are not listed above, be patient: Thank you Samuel for your positive attitude on everything. Thank you Ello, I really like your kindness and empathy. Thank you Shiyang for listening some nonsense stuffs from me. Thank you Neven for your special thoughts. Thanks David B for very nice scientific discussion. Thank you Emma, you are always gentle, polite, and full with happiness when I asked some simple questions. Thank you Hampus, I remember you answer so many questions from me when I just started my PhD. Thank you Sylvain for letting me know some crazy things (at least in my point of view). Thank you Piotr for sharing your experience and idea. Thank you Jan L, I appreciate your help on so many things, especially something related to MEDEA.

MEDEA program, one of the horizon 2020 project, gave me so many good memories. Not only the traveling, but also the science (important !). I really appreciate for all the people participating in this program. Thanks Per and Johan about your help and contribution in this project. Thank you Anders for giving many good advice on the presentation skills. I also want to thank the organizers and coordinators, you made the project move smoother than expected.

I would like to thank all the people in atomic physics, you provide a great working environment and atmosphere here. I really appreciate Xiaocui, Jimmy, Amelie, Qian, Adam, Chunyan, Lars, Stefan... too many colleagues that I can not list here. But, I want to especially thanks our administrative people: Anne P, Jakob, and  Ake. Thank you for taking care of all the important things that usually seem difficult for me.

I also want to thank my friends I met in Lund, thank you for sharing the thoughts that help me to move on. Besides, I would like to thank people that are not mentioned above, but you also helped me a lot during my PhD study. Thank you for all the people again, and it is my pleasure to be here.

In the end, I would like to thank my parents for their upbringing and their supports, such that I can pursue my PhD without considering other things. Besides, I also want to thank my previous supervisor Andy. Without his help, I would probably not have a chance to be here with you guys.

REFERENCES

1. J. Martin, A. Migus, C. Poyart, Y. Lecarpentier, R. Astier and A. Antonetti. *Femtosecond photolysis of CO-ligated protoheme and hemoproteins: appearance of deoxy species with a 350-fsec time constant*. Proceedings of the National Academy of Sciences **80**, 173–177 (1983).
2. C. L. Thomsen, D. Madsen, J. A. Poulsen, J. Thøgersen, S. K. Jensen and S. R. Keiding. *Femtosecond photolysis of aqueous HOCl*. The Journal of Chemical Physics **115**, 9361–9369 (2001).
3. A. Hu, J. Sanderson, A. Zaidi, C. Wang, T. Zhang, Y. Zhou and W. Du-ley. *Direct synthesis of polyene molecules in acetone by dissociation using femtosecond laser irradiation*. Carbon **46**, 1823–1825 (2008).
4. M. Dantus, M. J. Rosker and A. H. Zewail. *Real-time femtosecond probing of “transition states” in chemical reactions*. The Journal of Chemical Physics **87**, 2395–2397 (1987).
5. M. J. Rosker, M. Dantus and A. H. Zewail. *Femtosecond clocking of the chemical bond*. Science **241**, 1200–1202 (1988).
6. A. H. Zewail. *Femtochemistry: Atomic-scale dynamics of the chemical bond*. The Journal of Physical Chemistry A **104**, 5660–5694 (2000).
7. P. Auger. *Sur l’effet photoélectrique composé*. Journal de Physique et le Radium **6**, 205–208 (1925).
8. T. Gaumnitz, A. Jain, Y. Pertot, M. Huppert, I. Jordan, F. Ardana-Lamas and H. J. Wörner. *Streaking of 43-attosecond soft-X-ray pulses generated by a passively CEP-stable mid-infrared driver*. Optics Express **25**, 27506–27518 (2017).
9. P. M. Paul, E. Toma, P. Breger, G. Mullot, F. Augé, P. Balcou, H. Muller and P. Agostini. *Observation of a train of attosecond pulses from high harmonic generation*. Science **292**, 1689–1692 (2001).
10. M. Hentschel, R. Kienberger, C. Spielmann, G. A. Reider, N. Milosevic, T. Brabec, P. Corkum, U. Heinzmann, M. Drescher and F. Krausz. *Attosecond metrology*. Nature **414**, 509 (2001).

11. I. Sola, E. Mével, L. Elouga, E. Constant, V. Strelkov, L. Poletto, P. Villoresi, E. Benedetti, J.-P. Caumes, S. Stagira et al. *Controlling attosecond electron dynamics by phase-stabilized polarization gating*. *Nature Physics* **2**, 319 (2006).
12. S. Gilbertson, M. Chini, X. Feng, S. Khan, Y. Wu and Z. Chang. *Monitoring and controlling the electron dynamics in helium with isolated attosecond pulses*. *Physical Review Letters* **105**, 263003 (2010).
13. M. Isinger, R. Squibb, D. Busto, S. Zhong, A. Harth, D. Kroon, S. Nandi, C. Arnold, M. Miranda, J. M. Dahlström et al. *Photoionization in the time and frequency domain*. *Science* **358**, 893–896 (2017).
14. F. Calegari, D. Ayuso, A. Trabattoni, L. Belshaw, S. De Camillis, S. Anumula, F. Frassetto, L. Poletto, A. Palacios, P. Decleva et al. *Ultrafast electron dynamics in phenylalanine initiated by attosecond pulses*. *Science* **346**, 336–339 (2014).
15. P. M. Kraus, B. Mignolet, D. Baykusheva, A. Rupenyan, L. Horný, E. F. Penka, G. Grassi, O. I. Tolstikhin, J. Schneider, F. Jensen et al. *Measurement and laser control of attosecond charge migration in ionized iodoacetylene*. *Science* **350**, 790–795 (2015).
16. J. P. Nibarger, S. V. Menon and G. N. Gibson. *Comprehensive analysis of strong-field ionization and dissociation of diatomic nitrogen*. *Physical Review A* **63**, 053406 (2001).
17. L. Young, E. Kanter, B. Krässig, Y. Li, A. March, S. Pratt, R. Santra, S. Southworth, N. Rohringer, L. DiMauro et al. *Femtosecond electronic response of atoms to ultra-intense X-rays*. *Nature* **466**, 56 (2010).
18. V. Stert, W. Radloff, C. Schulz and I. Hertel. *Ultrafast photoelectron spectroscopy: Femtosecond pump-probe coincidence detection of ammonia cluster ions and electrons*. *The European Physical Journal D-Atomic, Molecular, Optical and Plasma Physics* **5**, 97–106 (1999).
19. P. F. Moulton. *Spectroscopic and laser characteristics of Ti: Al₂O₃*. *Journal of the Optical Society of America B* **3**, 125–133 (1986).
20. D. H. Sutter, G. Steinmeyer, L. Gallmann, N. Matuschek, F. Morier-Genoud, U. Keller, V. Scheuer, G. Angelow and T. Tschudi. *Semiconductor saturable-absorber mirror-assisted Kerr-lens mode-locked Ti: sapphire laser producing pulses in the two-cycle regime*. *Optics Letters* **24**, 631–633 (1999).
21. U. Morgner, F. X. Kärtner, S.-H. Cho, Y. Chen, H. A. Haus, J. G. Fujimoto, E. P. Ippen, V. Scheuer, G. Angelow and T. Tschudi. *Sub-two-cycle pulses from a Kerr-lens mode-locked Ti: sapphire laser*. *Optics Letters* **24**, 411–413 (1999).
22. R. Ell, U. Morgner, F. X. Kärtner, J. G. Fujimoto, E. P. Ippen, V. Scheuer, G. Angelow, T. Tschudi, M. J. Lederer, A. Boiko et al. *Generation of 5-fs*

- pulses and octave-spanning spectra directly from a Ti: sapphire laser*. Optics Letters **26**, 373–375 (2001).
23. L. Matos, D. Kleppner, O. Kuzucu, T. Schibli, J. Kim, E. Ippen and F. Kaertner. *Direct frequency comb generation from an octave-spanning, prismless Ti: sapphire laser*. Optics Letters **29**, 1683–1685 (2004).
 24. D. J. Jones, S. A. Diddams, J. K. Ranka, A. Stentz, R. S. Windeler, J. L. Hall and S. T. Cundiff. *Carrier-envelope phase control of femtosecond mode-locked lasers and direct optical frequency synthesis*. Science **288**, 635–639 (2000).
 25. B. E. Saleh and M. C. Teich. *Fundamentals of Photonics*. Wiley New York (2007).
 26. D. Strickland and G. Mourou. *Compression of amplified chirped optical pulses*. Optics Communications **55**, 447–449 (1985).
 27. A. Dubietis, G. Jonušauskas and A. Piskarskas. *Powerful femtosecond pulse generation by chirped and stretched pulse parametric amplification in BBO crystal*. Optics Communications **88**, 437–440 (1992).
 28. R. Butkus, R. Danielius, A. Dubietis, A. Piskarskas and A. Stabinis. *Progress in chirped pulse optical parametric amplifiers*. Applied Physics B **79**, 693–700 (2004).
 29. A. Shirakawa and T. Kobayashi. *Noncollinearly phase-matched femtosecond optical parametric amplification with a 2000 cm⁻¹ bandwidth*. Applied Physics Letters **72**, 147–149 (1998).
 30. A. Shirakawa, I. Sakane, M. Takasaka and T. Kobayashi. *Sub-5-fs visible pulse generation by pulse-front-matched noncollinear optical parametric amplification*. Applied Physics Letters **74**, 2268–2270 (1999).
 31. A. Baltuška, T. Fuji and T. Kobayashi. *Visible pulse compression to 4 fs by optical parametric amplification and programmable dispersion control*. Optics Letters **27**, 306–308 (2002).
 32. T. Lang, A. Harth, J. Matyschok, T. Binhammer, M. Schultze and U. Morgner. *Impact of temporal, spatial and cascaded effects on the pulse formation in ultra-broadband parametric amplifiers*. Optics Express **21**, 949–959 (2013).
 33. A. L. Oien, I. T. McKinnie, P. Jain, N. A. Russell, D. M. Warrington and L. A. Gloster. *Efficient, low-threshold collinear and noncollinear β -barium borate optical parametric oscillators*. Optics Letters **22**, 859–861 (1997).
 34. J. Rothhardt, S. Demmler, S. Hädrich, J. Limpert and A. Tünnermann. *Octave-spanning OPCPA system delivering CEP-stable few-cycle pulses and 22 W of average power at 1 MHz repetition rate*. Optics Express **20**, 10870–10878 (2012).
 35. S. Prinz, M. Haefner, C. Y. Teisset, R. Bessing, K. Michel, Y. Lee, X. T.

- Geng, S. Kim, D. E. Kim, T. Metzger et al. *CEP-stable, sub-6 fs, 300-kHz OPCPA system with more than 15 W of average power*. Optics Express **23**, 1388–1394 (2015).
36. F. J. Furch, T. Witting, A. Giree, C. Luan, F. Schell, G. Arisholm, C. P. Schulz and M. J. Vrakking. *CEP-stable few-cycle pulses with more than 190 μJ of energy at 100 kHz from a noncollinear optical parametric amplifier*. Optics Letters **42**, 2495–2498 (2017).
37. R. Budriūnas, T. Stanislauskas, J. Adamonis, A. Aleknavičius, G. Veitas, D. Gadonas, S. Balickas, A. Michailovas and A. Varanavičius. *53 W average power CEP-stabilized OPCPA system delivering 5.5 TW few cycle pulses at 1 kHz repetition rate*. Optics Express **25**, 5797–5806 (2017).
38. D. J. Kane and R. Trebino. *Characterization of arbitrary femtosecond pulses using frequency-resolved optical gating*. IEEE Journal of Quantum Electronics **29**, 571–579 (1993).
39. C. Iaconis and I. A. Walmsley. *Spectral phase interferometry for direct electric-field reconstruction of ultrashort optical pulses*. Optics Letters **23**, 792–794 (1998).
40. V. V. Lozovoy, I. Pastirk and M. Dantus. *Multiphoton intrapulse interference. IV. Ultrashort laser pulse spectral phase characterization and compensation*. Optics Letters **29**, 775–777 (2004).
41. J. R. Birge, R. Ell and F. X. Kärtner. *Two-dimensional spectral shearing interferometry for few-cycle pulse characterization*. Optics Letters **31**, 2063–2065 (2006).
42. I. A. Walmsley and C. Dorrer. *Characterization of ultrashort electromagnetic pulses*. Advances in Optics and Photonics **1**, 308–437 (2009).
43. M. Miranda, C. L. Arnold, T. Fordell, F. Silva, B. Alonso, R. Weigand, A. L’Huillier and H. Crespo. *Characterization of broadband few-cycle laser pulses with the d-scan technique*. Optics Express **20**, 18732–18743 (2012).
44. M. Miranda, J. Penedones, C. Guo, A. Harth, M. Louisy, L. Neoričić, A. L’Huillier and C. L. Arnold. *Fast iterative retrieval algorithm for ultrashort pulse characterization using dispersion scans*. Journal of the Optical Society of America B **34**, 190–197 (2017).
45. M. Miranda, M. Kotur, P. Rudawski, C. Guo, A. Harth, A. L’Huillier and C. L. Arnold. *Spatiotemporal characterization of ultrashort laser pulses using spatially resolved Fourier transform spectrometry*. Optics Letters **39**, 5142–5145 (2014).
46. S. H. Chew, K. Pearce, C. Späth, A. Guggenmos, J. Schmidt, F. Süßmann, M. F. Kling, U. Kleineberg, E. Mårzell, C. L. Arnold et al. *Imaging Localized Surface Plasmons by Femtosecond to Attosecond Time-Resolved Photoelectron Emission Microscopy—“ATTO-PEEM”*. Attosecond Nanophysics: From Basic

- Science to Applications **10**, 1 (2015).
47. T. Suemoto, H. Nansei, S. Tomimoto and S. Saito. *Femtosecond luminescence of nonequilibrium carriers in InAs*. Journal of Luminescence **76**, 141–144 (1998).
 48. E. Mårzell, R. Svärd, M. Miranda, C. Guo, A. Harth, E. Lorek, J. Mauritsson, C. L. Arnold, H. Xu, A. L’Huillier et al. *Direct subwavelength imaging and control of near-field localization in individual silver nanocubes*. Applied Physics Letters **107**, 201111 (2015).
 49. E. Lorek, E. Mårzell, A. Losquin, M. Miranda, A. Harth, C. Guo, R. Svärd, C. L. Arnold, A. L’Huillier, A. Mikkelsen et al. *Size and shape dependent few-cycle near-field dynamics of bowtie nanoantennas*. Optics Express **23**, 31460–31471 (2015).
 50. E. Mårzell, A. Losquin, R. Svärd, M. Miranda, C. Guo, A. Harth, E. Lorek, J. Mauritsson, C. L. Arnold, H. Xu et al. *Nanoscale imaging of local few-femtosecond near-field dynamics within a single plasmonic nanoantenna*. Nano Letters **15**, 6601–6608 (2015).
 51. J. J. Sakurai and E. D. Commins. *Modern Quantum Mechanics, revised edition*. Addison-Wesley (1995).
 52. A. McPherson, G. Gibson, H. Jara, U. Johann, T. S. Luk, I. McIntyre, K. Boyer and C. K. Rhodes. *Studies of multiphoton production of vacuum-ultraviolet radiation in the rare gases*. Journal of the Optical Society of America B **4**, 595–601 (1987).
 53. M. Ferray, A. L’Huillier, X. Li, L. Lompre, G. Mainfray and C. Manus. *Multiple-harmonic conversion of 1064 nm radiation in rare gases*. Journal of Physics B: Atomic, Molecular and Optical Physics **21**, L31 (1988).
 54. P. B. Corkum. *Plasma perspective on strong field multiphoton ionization*. Physical Review Letters **71**, 1994 (1993).
 55. K. Schafer, B. Yang, L. DiMauro and K. Kulander. *Above threshold ionization beyond the high harmonic cutoff*. Physical Review Letters **70**, 1599 (1993).
 56. M. Lewenstein, P. Balcou, M. Y. Ivanov, A. L’huillier and P. B. Corkum. *Theory of high-harmonic generation by low-frequency laser fields*. Physical Review A **49**, 2117 (1994).
 57. K. Varju, Y. Mairesse, P. Agostini, P. Breger, B. Carré, L. Frasinski, E. Gustafsson, P. Johnsson, J. Mauritsson, H. Merdji et al. *Reconstruction of attosecond pulse trains using an adiabatic phase expansion*. Physical Review Letters **95**, 243901 (2005).
 58. C. Guo. *A high repetition rate attosecond light source based on optical parametric amplification*. PhD thesis Lund University (2018).
 59. S. Carlström, J. Preclíková, E. Lorek, E. W. Larsen, C. M. Heyl, D. Paleček,

- D. Zigmantas, K. J. Schafer, M. B. Gaarde and J. Mauritsson. *Spatially and spectrally resolved quantum path interference with chirped driving pulses*. New Journal of Physics **18**, 123032 (2016).
60. P. Balcou, A. S. Dederichs, M. B. Gaarde and A. L’Huillier. *Quantum-path analysis and phase matching of high-order harmonic generation and high-order frequency mixing processes in strong laser fields*. Journal of Physics B: Atomic, Molecular and Optical Physics **32**, 2973 (1999).
61. E. Brunetti, R. Issac and D. Jaroszynski. *Quantum path contribution to high-order harmonic spectra*. Physical Review A **77**, 023422 (2008).
62. C. Heyl, J. Gdde, U. Hfer and A. L’Huillier. *Spectrally resolved maker fringes in high-order harmonic generation*. Physical Review Letters **107**, 033903 (2011).
63. C. Heyl, J. Gdde, A. L’Huillier and U. Hfer. *High-order harmonic generation with μ J laser pulses at high repetition rates*. Journal of Physics B: Atomic, Molecular and Optical Physics **45**, 074020 (2012).
64. C. Heyl, H. Coudert-Alteirac, M. Miranda, M. Louisy, K. Kovcs, V. Tosa, E. Balogh, K. Varj, A. L’Huillier, A. Couairon et al. *Scale-invariant nonlinear optics in gases*. Optica **3**, 75–81 (2016).
65. G. Bird. *The DSMC method*. CreateSpace Independent Publishing Platform (2013).
66. E. Mansten, J. Dahlstrm, J. Mauritsson, T. Ruchon, A. L’Huillier, J. Tate, M. B. Gaarde, P. Eckle, A. Guandalini, M. Holler et al. *Spectral signature of short attosecond pulse trains*. Physical Review Letters **102**, 083002 (2009).
67. M. Krebs, S. Hdrich, S. Demmler, J. Rothhardt, A. Zair, L. Chipperfield, J. Limpert and A. Tnnermann. *Towards isolated attosecond pulses at megahertz repetition rates*. Nature Photonics **7**, 555 (2013).
68. P. Rudawski, A. Harth, C. Guo, E. Lorek, M. Miranda, C. M. Heyl, E. W. Larsen, J. Ahrens, O. Prochnow, T. Binhammer et al. *Carrier-envelope phase dependent high-order harmonic generation with a high-repetition rate OPCPA-system*. The European Physical Journal D **69**, 70 (2015).
69. C. Hernndez-Garca, W. Holgado, L. Plaja, B. Alonso, F. Silva, M. Miranda, H. Crespo and I. Sola. *Carrier-envelope-phase insensitivity in high-order harmonic generation driven by few-cycle laser pulses*. Optics Express **23**, 21497–21508 (2015).
70. M. Ammosov, N. Delone, V. Krainov, A. Perelomov, V. Popov, M. Terent’ev, G. L. Yudin and M. Y. Ivanov. *Tunnel ionization of complex atoms and of atomic ions in an alternating electric field*. Soviet Physics, Journal of Experimental and Theoretical Physics **64**, 1191–1194 (1986).
71. J. Samson and W. C. Stolte. *Precision measurements of the total photoionization cross-sections of He, Ne, Ar, Kr, and Xe*. Journal of Electron Spec-

- troscopy and Related Phenomena **123**, 265–276 (2002).
72. A. Sorokin, M. Wellhöfer, S. Bobashev, K. Tiedtke and M. Richter. *X-ray-laser interaction with matter and the role of multiphoton ionization: Free-electron-laser studies on neon and helium*. Physical Review A **75**, 051402 (2007).
 73. A. Rudenko, Y. Jiang, M. Kurka, K. Kühnel, L. Foucar, O. Herrwerth, M. Lezius, M. F. Kling, C. Schröter, R. Moshhammer et al. *Exploring few-photon, few-electron reactions at FLASH: from ion yield and momentum measurements to time-resolved and kinematically complete experiments*. Journal of Physics B: Atomic, Molecular and Optical Physics **43**, 194004 (2010).
 74. V. Ayvazyan, N. Baboi, J. Bähr, V. Balandin, B. Beutner, A. Brandt, I. Bohnet, A. Bolzmann, R. Brinkmann, O. Brovko et al. *First operation of a free-electron laser generating GW power radiation at 32 nm wavelength*. The European Physical Journal D-Atomic, Molecular, Optical and Plasma Physics **37**, 297–303 (2006).
 75. R. Akre, D. Dowell, P. Emma, J. Frisch, S. Gilevich, G. Hays, P. Hering, R. Iverson, C. Limborg-Deprey, H. Loos et al. *Commissioning the linac coherent light source injector*. Physical Review Special Topics - Accelerators and Beams **11**, 030703 (2008).
 76. P. Emma, R. Akre, J. Arthur, R. Bionta, C. Bostedt, J. Bozek, A. Brachmann, P. Bucksbaum, R. Coffee, F.-J. Decker et al. *First lasing and operation of an ångstrom-wavelength free-electron laser*. Nature Photonics **4**, 641 (2010).
 77. J. A. Clarke. *The Science and Technology of Undulators and Wigglers*. Number 4. Oxford University Press on Demand (2004).
 78. J.-E. Rubensson. *Synchrotron Radiation: An Everyday Application of Special Relativity*. Morgan & Claypool Publishers (2016).
 79. E. Allaria, R. Appio, L. Badano, W. Barletta, S. Bassanese, S. Biedron, A. Borga, E. Busetto, D. Castronovo, P. Cinquegrana et al. *Highly coherent and stable pulses from the FERMI seeded free-electron laser in the extreme ultraviolet*. Nature Photonics **6**, 699 (2012).
 80. K. Tiedtke, A. Azima, N. Von Bargen, L. Bittner, S. Bonfigt, S. Düsterer, B. Faatz, U. Frühling, M. Gensch, C. Gerth et al. *The soft x-ray free-electron laser FLASH at DESY: beamlines, diagnostics and end-stations*. New Journal of Physics **11**, 023029 (2009).
 81. T. Ishikawa, H. Aoyagi, T. Asaka, Y. Asano, N. Azumi, T. Bizen, H. Ego, K. Fukami, T. Fukui, Y. Furukawa et al. *A compact X-ray free-electron laser emitting in the sub-ångström region*. Nature Photonics **6**, 540 (2012).
 82. E. Seddon, J. Clarke, D. Dunning, C. Masciovecchio, C. Milne, F. Parmigiani, D. Rugg, J. Spence, N. Thompson, K. Ueda et al. *Short-wavelength free-electron laser sources and science: a review*. Reports on Progress in Physics

- 80**, 115901 (2017).
83. J. Feldhaus. *FLASH—the first soft x-ray free electron laser (FEL) user facility*. Journal of Physics B: Atomic, Molecular and Optical Physics **43**, 194002 (2010).
84. DESY: FLASH. <http://flash.desy.de/> (Accessed: 16-07-2018).
85. F. Sturm, M. Schöffler, S. Lee, T. Osipov, N. Neumann, H.-K. Kim, S. Kirschner, B. Rudek, J. Williams, J. Daughhetee et al. *Photoelectron and Auger-electron angular distributions of fixed-in-space CO 2*. Physical Review A **80**, 032506 (2009).
86. T. Jahnke, H. Sann, T. Havermeier, K. Kreidi, C. Stuck, M. Meckel, M. Schöffler, N. Neumann, R. Wallauer, S. Voss et al. *Ultrafast energy transfer between water molecules*. Nature Physics **6**, 139 (2010).
87. U. Hergenhahn. *Interatomic and intermolecular coulombic decay: The early years*. Journal of Electron Spectroscopy and Related Phenomena **184**, 78–90 (2011).
88. A. T. Eppink and D. H. Parker. *Velocity map imaging of ions and electrons using electrostatic lenses: Application in photoelectron and photofragment ion imaging of molecular oxygen*. Review of Scientific Instruments **68**, 3477–3484 (1997).
89. L. M. Smith, D. R. Keefer and S. Sudharsanan. *Abel inversion using transform techniques*. Journal of Quantitative Spectroscopy and Radiative Transfer **39**, 367–373 (1988).
90. M. Lebeck, J. Houver and D. Dowek. *Ion–electron velocity vector correlations in dissociative photoionization of simple molecules using electrostatic lenses*. Review of Scientific Instruments **73**, 1866–1874 (2002).
91. C. Bomme, R. Guillemin, T. Marin, L. Journel, T. Marchenko, D. Dowek, N. Trcera, B. Pilette, A. Avila, H. Ringuenet et al. *Double momentum spectrometer for ion–electron vector correlations in dissociative photoionization*. Review of Scientific Instruments **84**, 103104 (2013).
92. J. Laksman, D. Céolin, E. Månsson, S. L. Sorensen and M. Gisselbrecht. *Development and characterization of a multiple-coincidence ion-momentum imaging spectrometer*. Review of Scientific Instruments **84**, 123113 (2013).
93. E. P. Månsson, S. L. Sorensen, C. L. Arnold, D. Kroon, D. Guénot, T. Fordell, F. Lépine, P. Johnsson, A. L’Huillier and M. Gisselbrecht. *Multi-purpose two- and three-dimensional momentum imaging of charged particles for attosecond experiments at 1 kHz repetition rate*. Review of Scientific Instruments **85**, 123304 (2014).
94. J. Levin, R. Short, H. Cederquist, S. Elston, J. Gibbons, I. Sellin, H. Schmidt-Böcking et al. *Steep dependence of recoil-ion energy on coincident projectile and target ionization in swift ion-atom collisions*. Physical Review A **36**,

- 1649 (1987).
95. J. Ullrich and H. Schmidt-Böcking. *Time-of-flight spectrometer for the determination of microradian projectile scattering angles in atomic collisions*. Physics Letters A **125**, 193–196 (1987).
 96. R. Olson, J. Ullrich and H. Schmidt-Böcking. *Dynamics of multiply charged ion-atom collisions: $U32^{++}$ Ne*. Journal of Physics B: Atomic and Molecular Physics **20**, L809 (1987).
 97. R. Dörner, J. Ullrich, H. Schmidt-Böcking and R. Olson. *Three-body interactions in proton-helium angular scattering*. Physical Review Letters **63**, 147 (1989).
 98. R. Moshhammer, J. Ullrich, M. Unverzagt, W. Schmidt, P. Jardin, R. Olson, R. Mann, R. Dörner, V. Mergel, U. Buck et al. *Low-energy electrons and their dynamical correlation with recoil ions for single ionization of helium by fast, heavy-ion impact*. Physical Review Letters **73**, 3371 (1994).
 99. J. Ullrich, R. Moshhammer, R. Dörner, O. Jagutzki, V. Mergel, H. Schmidt-Böcking and L. Spielberger. *Recoil-ion momentum spectroscopy*. Journal of Physics B: Atomic, Molecular and Optical Physics **30**, 2917 (1997).
 100. R. Dörner, V. Mergel, O. Jagutzki, L. Spielberger, J. Ullrich, R. Moshhammer and H. Schmidt-Böcking. *Cold target recoil ion momentum spectroscopy: a ‘momentum microscope’ to view atomic collision dynamics*. Physics Reports **330**, 95–192 (2000).
 101. J. Ullrich, R. Moshhammer, A. Dorn, R. Dörner, L. P. H. Schmidt and H. Schmidt-Böcking. *Recoil-ion and electron momentum spectroscopy: reaction-microscopes*. Reports on Progress in Physics **66**, 1463 (2003).
 102. L. Strüder, S. Epp, D. Rolles, R. Hartmann, P. Holl, G. Lutz, H. Soltau, R. Eckart, C. Reich, K. Heinzinger et al. *Large-format, high-speed, X-ray pnCCDs combined with electron and ion imaging spectrometers in a multi-purpose chamber for experiments at 4th generation light sources*. Nuclear Instruments and Methods in Physics Research Section A: Accelerators, Spectrometers, Detectors and Associated Equipment **614**, 483–496 (2010).
 103. B. Erk, J. P. Müller, C. Bomme, R. Boll, G. Brenner, H. N. Chapman, J. Correa, S. Düsterer, S. Dziarzhytski, S. Eisebitt et al. *CAMP@ FLASH: an end-station for imaging, electron-and ion-spectroscopy, and pump-probe experiments at the FLASH free-electron laser*. Journal of Synchrotron Radiation **25** (2018).
 104. M. Lavollée. *A new detector for measuring three-dimensional momenta of charged particles in coincidence*. Review of Scientific Instruments **70**, 2968–2974 (1999).
 105. A. Huetz and J. Mazeau. *Double photoionization of helium down to 100 meV above threshold*. Physical Review Letters **85**, 530 (2000).

106. M. Gisselbrecht, A. Huetz, M. Lavollée, T. Reddish and D. Seccombe. *Optimization of momentum imaging systems using electric and magnetic fields*. Review of Scientific Instruments **76**, 013105 (2005).
107. Cubic Formula. <http://mathworld.wolfram.com/CubicFormula.html> (Accessed: 27-10-2018).
108. W. Wiley and I. H. McLaren. *Time-of-flight mass spectrometer with improved resolution*. Review of Scientific Instruments **26**, 1150–1157 (1955).
109. J. L. Kirschvink. *Uniform magnetic fields and double-wrapped coil systems: improved techniques for the design of bioelectromagnetic experiments*. Bioelectromagnetics **13**, 401–411 (1992).
110. R. S. Caprari. *Optimal current loop systems for producing uniform magnetic fields*. Measurement Science and Technology **6**, 593 (1995).
111. R. Merritt, C. Purcell and G. Stroink. *Uniform magnetic field produced by three, four, and five square coils*. Review of Scientific Instruments **54**, 879–882 (1983).
112. L. Lugansky. *Optimal coils for producing uniform magnetic fields*. Journal of Physics E: Scientific Instruments **20**, 277 (1987).
113. S. O. Kasap. *Principles of Electronic Materials and Devices* volume 2. McGraw-Hill New York (2006).
114. The RoentDek delay line detector with hexanode. http://www.roentdek.de/info/Delay_Line/ (Accessed: 22-08-2018).
115. T. McIlrath, P. Bucksbaum, R. Freeman and M. Bashkansky. *Above-threshold ionization processes in xenon and krypton*. Physical Review A **35**, 4611 (1987).
116. W. Becker, S. Goreslavski, D. Milošević and G. Paulus. *The plateau in above-threshold ionization: the keystone of rescattering physics*. Journal of Physics B: Atomic, Molecular and Optical Physics **51**, 162002 (2018).
117. A. Rudenko, K. Zrost, C. Schröter, V. De Jesus, B. Feuerstein, R. Moshhammer and J. Ullrich. *Resonant structures in the low-energy electron continuum for single ionization of atoms in the tunnelling regime*. Journal of Physics B: Atomic, Molecular and Optical Physics **37**, L407 (2004).
118. Z. Chen, T. Morishita, A.-T. Le, M. Wickenhauser, X. Tong and C. Lin. *Analysis of two-dimensional photoelectron momentum spectra and the effect of the long-range Coulomb potential in single ionization of atoms by intense lasers*. Physical Review A **74**, 053405 (2006).
119. T. Morishita, Z. Chen, S. Watanabe and C. Lin. *Two-dimensional electron momentum spectra of argon ionized by short intense lasers: Comparison of theory with experiment*. Physical Review A **75**, 023407 (2007).
120. D. G. Arbó, K. L. Ishikawa, K. Schiessl, E. Persson and J. Burgdörfer. *Intracycle and intercycle interferences in above-threshold ionization: The time*

- grating*. Physical Review A **81**, 021403 (2010).
121. National Centers for environmental information geomagnetic calculator. <https://www.ngdc.noaa.gov/geomag-web/> (Accessed: 29-08-2018).
 122. D. Manura and D. A. Dahl. *SIMION 8.0 User Manual*. Scientific Instrument Services (2007).
 123. B. P. Abbott, R. Abbott, T. Abbott, M. Abernathy, F. Acernese, K. Ackley, C. Adams, T. Adams, P. Addesso, R. Adhikari et al. *Observation of gravitational waves from a binary black hole merger*. Physical Review Letters **116**, 061102 (2016).
 124. C. Davisson and L. H. Germer. *Diffraction of electrons by a crystal of nickel*. Physical Review **30**, 705 (1927).
 125. F. Quéré, J. Itatani, G. Yudin and P. Corkum. *Attosecond spectral shearing interferometry*. Physical Review Letters **90**, 073902 (2003).
 126. N. Dudovich, O. Smirnova, J. Levesque, Y. Mairesse, M. Y. Ivanov, D. Villeneuve and P. B. Corkum. *Measuring and controlling the birth of attosecond XUV pulses*. Nature Physics **2**, 781 (2006).
 127. T. Remetter, P. Johnsson, J. Mauritsson, K. Varjú, Y. Ni, F. Lépine, E. Gustafsson, M. Kling, J. Khan, R. López-Martens et al. *Attosecond electron wave packet interferometry*. Nature Physics **2**, 323 (2006).
 128. P. Johnsson, J. Mauritsson, T. Remetter, A. L’Huillier and K. J. Schafer. *Attosecond control of ionization by wave-packet interference*. Physical Review Letters **99**, 233001 (2007).
 129. M. Dahlström. *Light matter interaction on the attosecond timescale*. PhD thesis Lund University (2011).
 130. L. H. Haber, B. Doughty and S. R. Leone. *Continuum phase shifts and partial cross sections for photoionization from excited states of atomic helium measured by high-order harmonic optical pump-probe velocity map imaging*. Physical Review A **79**, 031401 (2009).
 131. Y. Mairesse, A. De Bohan, L. Frasinski, H. Merdji, L. Dinu, P. Monchicourt, P. Breger, M. Kovačev, R. Taïeb, B. Carré et al. *Attosecond synchronization of high-harmonic soft x-rays*. Science **302**, 1540–1543 (2003).
 132. G. Laurent, W. Cao, H. Li, Z. Wang, I. Ben-Itzhak and C. L. Cocke. *Attosecond control of orbital parity mix interferences and the relative phase of even and odd harmonics in an attosecond pulse train*. Physical Review Letters **109**, 083001 (2012).
 133. B. Erk, R. Boll, S. Trippel, D. Anielski, L. Foucar, B. Rudek, S. W. Epp, R. Coffee, S. Carron, S. Schorb et al. *Imaging charge transfer in iodomethane upon x-ray photoabsorption*. Science **345**, 288–291 (2014).
 134. R. A. Marcus. *Electron transfer reactions in chemistry. Theory and experi-*

- ment. *Reviews of Modern Physics* **65**, 599 (1993).
135. E. Sjulstok, J. M. H. Olsen and I. A. Solov'yov. *Quantifying electron transfer reactions in biological systems: what interactions play the major role?* *Scientific Reports* **5**, 18446 (2015).
136. E. R. Williams. *Proton transfer reactivity of large multiply charged ions.* *Journal of Mass Spectrometry* **31**, 831–842 (1996).
137. T. Cravens. *Comet Hyakutake X-ray source: Charge transfer of solar wind heavy ions.* *Geophysical Research Letters* **24**, 105–108 (1997).
138. K. Schnorr, A. Senftleben, M. Kurka, A. Rudenko, G. Schmid, T. Pfeifer, K. Meyer, M. Kübel, M. F. Kling, Y. H. Jiang, R. Treusch, S. Düsterer, B. Siemer, M. Wöstmann, H. Zacharias, R. Mitzner, T. J. M. Zouros, J. Ullrich, C. D. Schröter and R. Moshhammer. *Electron Rearrangement Dynamics in Dissociating I_2^+ Molecules Accessed by Extreme Ultraviolet Pump-Probe Experiments.* *Physical Review Letters* **113**, 073001 (2014).
139. R. Boll, B. Erk, R. Coffee, S. Trippel, T. Kierspel, C. Bomme, J. D. Bozek, M. Burkett, S. Carron, K. R. Ferguson et al. *Charge transfer in dissociating iodomethane and fluoromethane molecules ionized by intense femtosecond X-ray pulses.* *Structural Dynamics* **3**, 043207 (2016).
140. K. Motomura, E. Kukk, H. Fukuzawa, S.-i. Wada, K. Nagaya, S. Ohmura, S. Mondal, T. Tachibana, Y. Ito, R. Koga et al. *Charge and nuclear dynamics induced by deep inner-shell multiphoton ionization of CH₃I molecules by intense x-ray free-electron laser pulses.* *The Journal of Physical Chemistry Letters* **6**, 2944–2949 (2015).
141. A. Rudenko, L. Inhester, K. Hanasaki, X. Li, S. Robotjazi, B. Erk, R. Boll, K. Toyota, Y. Hao, O. Vendrell et al. *Femtosecond response of polyatomic molecules to ultra-intense hard X-rays.* *Nature* **546**, 129 (2017).
142. M. Makris, P. Lambropoulos and A. Mihelič. *Theory of multiphoton multi-electron ionization of xenon under strong 93-eV radiation.* *Physical Review Letters* **102**, 033002 (2009).
143. B. Rudek, S.-K. Son, L. Foucar, S. W. Epp, B. Erk, R. Hartmann, M. Adolph, R. Andritschke, A. Aquila, N. Berrah et al. *Ultra-efficient ionization of heavy atoms by intense X-ray free-electron laser pulses.* *Nature Photonics* **6**, 858 (2012).
144. N. Gerken, S. Klumpp, A. Sorokin, K. Tiedtke, M. Richter, V. Bürk, K. Mertens, P. Juranić and M. Martins. *Time-dependent multiphoton ionization of xenon in the soft-X-ray regime.* *Physical Review Letters* **112**, 213002 (2014).
145. K. Mertens, N. Gerken, S. Klumpp, M. Braune and M. Martins. *Soft x-ray multiphoton excitation of small iodine methane derivatives.* *Journal of Modern Optics* **63**, 383–389 (2016).

146. B. Henke, P. Lee, T. Tanaka, R. L. Shimabukuro and B. Fujikawa. *Low-energy X-ray interaction coefficients: Photoabsorption, scattering, and reflection: $E=100\text{--}2000\text{ eV}$ $Z=1\text{--}94$* . Atomic Data and Nuclear Data Tables **27**, 1–144 (1982).
147. J. Yeh and I. Lindau. *Atomic subshell photoionization cross sections and asymmetry parameters: $1 \leq Z \leq 103$* . Atomic Data and Nuclear Data Tables **32**, 1–155 (1985).
148. L. Nahon, A. Svensson and P. Morin. *Experimental study of the $4d$ ionization continuum in atomic iodine by photoelectron and photoion spectroscopy*. Physical Review A **43**, 2328 (1991).
149. J. Cutler, G. Bancroft and K. Tan. *Ligand-field splittings and core-level linewidths in $I\ 4d$ photoelectron spectra of iodine molecules*. The Journal of Chemical Physics **97**, 7932–7943 (1992).
150. M. Krikunova, T. Maltezopoulos, P. Wessels, M. Schlie, A. Azima, M. Wieland and M. Drescher. *Ultrafast photofragmentation dynamics of molecular iodine driven with timed XUV and near-infrared light pulses*. The Journal of Chemical Physics **134**, 024313 (2011).
151. M. Uiberacker, T. Uphues, M. Schultze, A. J. Verhoef, V. Yakovlev, M. F. Kling, J. Rauschenberger, N. M. Kabachnik, H. Schröder, M. Lezius et al. *Attosecond real-time observation of electron tunnelling in atoms*. Nature **446**, 627 (2007).
152. G. Dujardin, L. Hellner, D. Winkoun and M. Besnard. *Valence and inner shell electronic processes in dissociative double photoionization of CH_3I* . Chemical Physics **105**, 291–299 (1986).
153. G. G. O’Sullivan, C. McGuinness, J. T. Costello, E. T. Kennedy and B. Weinmann. *Trends in $4d$ -subshell photoabsorption along the iodine isonuclear sequence: I , I^+ , and $I\ 2^+$* . Physical Review A **53**, 3211 (1996).
154. H. Kjeldsen, P. Andersen, F. Folkmann, H. Knudsen, B. Kristensen, J. West and T. Andersen. *Absolute photoionization cross sections of I^+ and $I\ 2^+$ in the $4d$ ionization region*. Physical Review A **62**, 020702 (2000).
155. A. Domondon and X. Tong. *Photoabsorption spectra of I and its ions in the $4d$ region*. Physical Review A **65**, 032718 (2002).
156. J. Bizau, C. Blancard, D. Cubaynes, F. Folkmann, J. Champeaux, J. Lemaire and F. Wuilleumier. *Absolute photoionization cross sections along the Xe isonuclear sequence: $Xe\ 3^+$ to $Xe\ 6^+$* . Physical Review A **73**, 022718 (2006).
157. A. Aguilar, J. D. Gillaspay, G. Gribakin, R. Phaneuf, M. Gharaibeh, M. Kozlov, J. Bozek and A. Kilcoyne. *Absolute photoionization cross sections for $Xe\ 4^+$, $Xe\ 5^+$, and $Xe\ 6^+$ near 13.5 nm : Experiment and theory*. Physical Review A **73**, 032717 (2006).
158. A. Müller, S. Schippers, D. Esteves-Macaluso, M. Habibi, A. Aguilar, A. Kil-

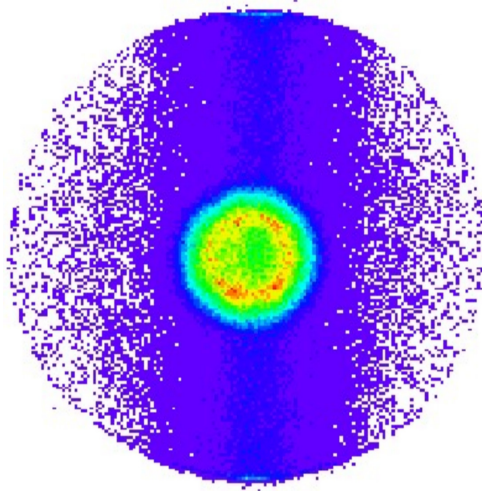
- coyne, R. Phaneuf, C. Ballance and B. McLaughlin. *Valence-shell photoionization of Ag-like Xe7+ ions: experiment and theory*. Journal of Physics B: Atomic, Molecular and Optical Physics **47**, 215202 (2014).
159. P. Andersen, T. Andersen, F. Folkmann, V. Ivanov, H. Kjeldsen and J. West. *Absolute cross sections for the photoionization of 4d electrons in Xe+ and Xe2+ ions*. Journal of Physics B: Atomic, Molecular and Optical Physics **34**, 2009 (2001).
160. NIST Atomic Spectra Database (ver. 5.5.6). <https://physics.nist.gov/asd> (Accessed: 15-09-2018).
161. H. Kjeldsen, J. Hansen, F. Folkmann, H. Knudsen, J. West and T. Andersen. *The absolute cross section for L-shell photoionization of C+ ions from threshold to 105 eV*. The Astrophysical Journal Supplement Series **135**, 285 (2001).
162. D.-S. Kim and S. T. Manson. *Photoionization of the ground state of the Be-like C2+ ion leading to C3+ 2l and 3l states*. Journal of Physics B: Atomic, Molecular and Optical Physics **37**, 4707 (2004).
163. D.-S. Kim and Y. S. Kim. *Characteristics of photoionization in the XUV domain for the excited 1s22s2p1, 3Po states of the Be-like C2+ ion*. Journal of Physics B: Atomic, Molecular and Optical Physics **40**, 3807 (2007).
164. H. Liu, Z. Yang, Z. Gao and Z. Tang. *Ionization and dissociation of CH 3 I in intense laser field*. The Journal of Chemical Physics **126**, 044316 (2007).
165. Y. Wang, S. Zhang, Z. Wei and B. Zhang. *Velocity map imaging of dissociative ionization and coulomb explosion of CH3I induced by a femtosecond laser*. The Journal of Physical Chemistry A **112**, 3846–3851 (2008).
166. M. E. Corrales, G. Gitzinger, J. González-Vázquez, V. Loriot, R. de Nalda and L. Banares. *Velocity map imaging and theoretical study of the Coulomb explosion of CH3I under intense femtosecond IR pulses*. The Journal of Physical Chemistry A **116**, 2669–2677 (2011).
167. H. Ryufuku, K. Sasaki and T. Watanabe. *Oscillatory behavior of charge transfer cross sections as a function of the charge of projectiles in low-energy collisions*. Physical Review A **21**, 745 (1980).
168. K. Schnorr. *XUV Pump-Probe Experiments on Diatomic Molecules: Tracing the Dynamics of Electron Rearrangement and Interatomic Coulombic Decay*. Springer (2014).
169. F. Brauße, G. Goldsztejn, K. Amini, R. Boll, S. Bari, C. Bomme, M. Brouard, M. Burt, B. C. De Miranda, S. Düsterer et al. *Time-resolved inner-shell photoelectron spectroscopy: From a bound molecule to an isolated atom*. Physical Review A **97**, 043429 (2018).
170. G. Sanna and G. Tomassetti. *Introduction to Molecular Beams Gas Dynamics*. World Scientific (2005).

171. T. Wall. *Preparation of cold molecules for high-precision measurements*. Journal of Physics B: Atomic, Molecular and Optical Physics **49**, 243001 (2016).
172. D. Low and E. Moelwyn-Hughes. *The heat capacities of acetone, methyl iodide and mixtures thereof in the liquid state*. Proceedings of the Royal Society of London. Series A. Mathematical and Physical Sciences **267**, 384–394 (1962).
173. N. Rohringer and R. Santra. *X-ray nonlinear optical processes using a self-amplified spontaneous emission free-electron laser*. Physical Review A **76**, 033416 (2007).
174. B. Erk, D. Rolles, L. Foucar, B. Rudek, S. W. Epp, M. Cryle, C. Bostedt, S. Schorb, J. Bozek, A. Rouzee et al. *Ultrafast charge rearrangement and nuclear dynamics upon inner-shell multiple ionization of small polyatomic molecules*. Physical Review Letters **110**, 053003 (2013).
175. J. Rothhardt, S. Hädrich, Y. Shamir, M. Tschernajew, R. Klas, A. Hoffmann, G. K. Tadesse, A. Klenke, T. Gottschall, T. Eidam et al. *High-repetition-rate and high-photon-flux 70 eV high-harmonic source for coincidence ion imaging of gas-phase molecules*. Optics Express **24**, 18133–18147 (2016).
176. G. Andriukaitis, T. Balčiūnas, S. Ališauskas, A. Pugžlys, A. Baltuška, T. Popmintchev, M.-C. Chen, M. M. Murnane and H. C. Kapteyn. *90 GW peak power few-cycle mid-infrared pulses from an optical parametric amplifier*. Optics Letters **36**, 2755–2757 (2011).
177. T. Popmintchev, M.-C. Chen, D. Popmintchev, P. Arpin, S. Brown, S. Ališauskas, G. Andriukaitis, T. Balčiūnas, O. D. Mücke, A. Pugžlys et al. *Bright coherent ultrahigh harmonics in the keV x-ray regime from mid-infrared femtosecond lasers*. Science **336**, 1287–1291 (2012).
178. K. Klünder, J. Dahlström, M. Gisselbrecht, T. Fordell, M. Swoboda, D. Guenot, P. Johnsson, J. Caillat, J. Mauritsson, A. Maquet et al. *Probing single-photon ionization on the attosecond time scale*. Physical Review Letters **106**, 143002 (2011).
179. M. Isinger, D. Busto, S. Mikaelsson, S. Zhong, C. Guo, P. Salières, C. Arnold, A. L’Huillier and M. Gisselbrecht. *Temporal Resolution of the RABBIT technique*. arXiv preprint arXiv:1812.06756 (2018).
180. S. Haessler, B. Fabre, J. Higuët, J. Caillat, T. Ruchon, P. Breger, B. Carré, E. Constant, A. Maquet, E. Mével et al. *Phase-resolved attosecond near-threshold photoionization of molecular nitrogen*. Physical Review A **80**, 011404 (2009).
181. D. Busto, L. Barreau, M. Isinger, M. Turconi, C. Alexandridi, A. Harth, S. Zhong, R. Squibb, D. Kroon, S. Plogmaker et al. *Time–frequency representation of autoionization dynamics in helium*. Journal of Physics B: Atomic, Molecular and Optical Physics **51**, 044002 (2018).

182. M. R. Bionta, H. Lemke, J. Cryan, J. Glowonia, C. Bostedt, M. Cammarata, J.-C. Castagna, Y. Ding, D. Fritz, A. Fry et al. *Spectral encoding of x-ray/optical relative delay*. Optics Express **19**, 21855–21865 (2011).
183. M. Danailov. *MB Danailov, F. Bencivenga, F. Capotondi, F. Casolari, P. Cinquegrana, A. Demidovich, E. Giangrisostomi, MP Kiskinova, G. Kurdi, M. Manfreda, C. Masciovecchio, R. Mincigrucci, IP Nikolov, E. Pedersoli, E. Principi, and P. Sigalotti, Opt. Express 22, 12869 (2014)*. Optics Express **22**, 12869 (2014).
184. S. Schulz, I. Grguraš, C. Behrens, H. Bromberger, J. Costello, M. Czwalińska, M. Felber, M. Hoffmann, M. Ilchen, H. Liu et al. *Femtosecond all-optical synchronization of an X-ray free-electron laser*. Nature Communications **6**, 5938 (2015).
185. E. Savelyev, R. Boll, C. Bomme, N. Schirmel, H. Redlin, B. Erk, S. Düsterer, E. Müller, H. Höppner, S. Toileikis et al. *Jitter-correction for IR/UV-XUV pump-probe experiments at the FLASH free-electron laser*. New Journal of Physics **19**, 043009 (2017).
186. C. Behrens, F.-J. Decker, Y. Ding, V. Dolgashev, J. Frisch, Z. Huang, P. Krejcik, H. Loos, A. Lutman, T. Maxwell et al. *Few-femtosecond time-resolved measurements of X-ray free-electron lasers*. Nature Communications **5**, 3762 (2014).
187. M. Kozák, J. McNeur, K. J. Leedle, H. Deng, N. Schönenberger, A. Ruehl, I. Hartl, J. Harris, R. Byer and P. Hommelhoff. *Optical gating and streaking of free electrons with sub-optical cycle precision*. Nature Communications **8**, 14342 (2017).
188. N. Hartmann, G. Hartmann, R. Heider, M. Wagner, M. Ilchen, J. Buck, A. Lindahl, C. Benko, J. Grünert, J. Krzywinski et al. *Attosecond time-energy structure of X-ray free-electron laser pulses*. Nature Photonics **12**, 215 (2018).



LUND
UNIVERSITY



Faculty of Engineering, LTH

Lund University

ISBN 978-91-7895-026-3

ISSN 0281-2762

Lund Reports on Atomic Physics, LARP 555 (2019)

